

Structural Modulation and Phase Transitions in Melilites



Dissertation

zur
Erlangung des Doktorgrades
der Naturwissenschaften
(Dr. rer. nat.)

dem
Fachbereich Geowissenschaften
der
Philipps-Universität Marburg

vorgelegt von
Zhihong Jia
aus der V. R. China

Marburg/Lahn, Germany 2005

Vom Fachbereich Geowissenschaften
der Philipps-Universität Marburg
als Dissertation am 17. 01. 2005 angenommen.
Erstgutachter: Dr. Helmut Rager
Zweitgutachter: Prof. Dr. Werner Massa
Tag der mündlichen Prüfung am 02. 02. 2005

Contents

1	Introduction.....	1
2	Structure modulation of melilites.....	3
2.1	General aspects of incommensurability.....	3
2.2	The melilite system.....	4
2.2.1	Temperature dependence of the structure modulation.....	5
2.2.2	The compositional dependence of the structure modulation.....	8
2.3	Mechanisms of the structure modulation in melilites.....	9
3	Experimental methods.....	13
3.1	Single-crystal growth method and apparatus.....	13
3.1.1	Double ellipsoid mirror furnace.....	13
3.1.2	Factors affecting single crystal quality.....	16
3.2	Electron microscopy.....	18
3.2.1	Transmission electron microscopy.....	18
3.2.2	Scanning electron microscopy, energy-dispersive X-ray spectrometry and wavelength-dispersive X-ray spectrometry.....	29
3.3	Electron spin resonance.....	32
3.4	X-ray diffraction.....	34
3.5	Magnetic measurements.....	36
3.6	Other methods.....	39
3.6.1	Differential scanning calorimeter.....	39
3.6.2	Photoluminescence measurements.....	39
4	Results and discussions.....	40
4.1	Synthesis of $\text{Ca}_2\text{MgSi}_2\text{O}_7$, $\text{Ca}_2\text{CoSi}_2\text{O}_7$ and $\text{Ca}_2\text{ZnSi}_2\text{O}_7$ melilites.....	40
4.2	Single crystal growth.....	44
4.2.1	The preparation of a feed rod and a seed crystal.....	44
4.2.2	Growth of $\text{Ca}_2\text{Mg}_{1-x}\text{Zn}_x\text{Si}_2\text{O}_7$, $\text{Ca}_2\text{Co}_{1-x}\text{Zn}_x\text{Si}_2\text{O}_7$, $(\text{Ca}_{1-x}\text{Sr}_x)_2\text{CoSi}_2\text{O}_7$ crystals	46
4.3	Investigations of $\text{Ca}_2\text{Mg}_{1-x}(\text{Zn}, \text{Co})_x\text{Si}_2\text{O}_7$ with modulated structure.....	55
4.3.1	The $\text{Ca}_2\text{Mg}_{1-x}\text{Zn}_x\text{Si}_2\text{O}_7$ system.....	55

Contents

4.3.2	The $\text{Ca}_2\text{Mg}_{1-x}\text{Co}_x\text{Si}_2\text{O}_7$ system	60
4.3.3	Conclusions.....	65
4.4	Modulation and phase transitions of $\text{Ca}_2\text{Co}_{1-x}\text{Zn}_x\text{Si}_2\text{O}_7$ in dependence on temperature and composition	66
4.4.1	Crystal growth and characterization	66
4.4.2	The average structure observed by high-resolution transmission electron microscopy and corresponding image simulation.....	71
4.4.3	Electron microscope studies of the modulated structure	74
4.4.4	The transition from the incommensurate phase to the commensurate lock-in phase and to the normal phase	78
4.4.5	Refinement of the commensurate lock-in structure of $\text{Ca}_2\text{Co}_{0.9}\text{Zn}_{0.1}\text{Si}_2\text{O}_7$	88
4.4.6	Conclusions.....	92
4.5	Investigations of the structural modulation of $(\text{Ca}_{1-x}\text{Sr}_x)_2\text{CoSi}_2\text{O}_7$	94
4.5.1	Crystal characterization	94
4.5.2	The modulated structure and the transition from the incommensurate to the normal phase with varying Sr-content	99
4.5.3	Conclusions.....	106
4.6	Investigations of $\text{Ca}_2(\text{Mg},\text{Co})\text{Si}_2\text{O}_7$ doped with Cr and Eu	107
4.6.1	Synthesis and characterization of $\text{Ca}_2\text{MgSi}_2\text{O}_7:\text{Cr}$ solid solutions	107
4.6.2	Synthesis, characterization and optical properties of $\text{Ca}_2\text{Mg}(\text{Co})\text{Si}_2\text{O}_7:\text{Eu}$ solid solutions	110
4.6.3	Conclusions.....	116
5	Summary and outlook	117
6	Zusammenfassung und Ausblick.....	120
7	References.....	123

Appendix A. Lock-in phase of $\text{Ca}_2(\text{Co}_{0.9}\text{Zn}_{0.1})\text{Si}_2\text{O}_7$ refined in s. g. $P2_12_12$

Appendix B. Lock-in phase of $\text{Ca}_2(\text{Co}_{0.9}\text{Zn}_{0.1})\text{Si}_2\text{O}_7$ refined in s. g. $P\bar{4}$.

Appendix C. Abbreviations

Acknowledgements

1 Introduction

A crystal consisting of atoms repeated regularly in three dimensions has a so-called translational symmetry, which can be described by one of the 230 crystallographic space groups. The lattice periodicity is apparent in X-ray, electron or neutron diffraction patterns which consist of sharp spots located on points of the reciprocal lattice. Often, additional spots besides the main reflections are observed, they can be attributed to the existence of various kinds superlattice structures, lattice defects or structure modulations. Incommensurately modulated crystals are known from, e.g., quasi one-dimensional conductors ^[1], ferroelectrics ^[2], alloys ^[3], minerals ^[4, 5], composite crystals ^[6].

Extensive studies have been done on melilite-type compounds with the general formula $X_2T^1T^2O_7$ to elucidate the nature of the observed incommensurate ordering. The melilite structure consists of layers formed by T^1 and T^2 tetrahedra and the larger X cations located halfway between adjacent layers. The incommensurate modulation was first described independently by Hemingway et al. ^[4] and Seifert et al. ^[5] in synthetic $Ca_2MgSi_2O_7$ åkermanite. It was supposed that the misfit between the large X cations and the sheet-like tetrahedral framework might be responsible for the modulation. Changing the structural misfit by substitution of other cations or by temperature varied the amplitude of the modulation and the length of the modulation vector ^[7-11]. X-ray refinement suggested that the modulated structure is $P_{p4mg}^{P\bar{4}_2, m}$ according to the (3+2)-dimensional superspace formalism, and that the modulation is caused by a displacive shift of the constituent atoms resulting in a rotation and deformation of the T^1 and T^2 tetrahedra ^[12, 13]. These changes appear to be accompanied by changes of the interlayer X -cation environment in a way that reduces the coordination number of X from eight to seven or even six ^[14-17]. It was further concluded that the flattened T^1 -tetrahedra surrounded by low-coordinated X cations show the tendency to form octagonal clusters, and that the arrangement of these clusters determines the strength of the overall modulation ^[16, 18, 19].

In spite of the number of studies, the detailed structure of modulated melilite crystals has not yet been clarified till now. This holds for the atomic configurations and the correct symmetry relations of the five-dimensional structure as well as the different aspects of superstructure ordering. The transition from the incommensurate

to the commensurate lock-in phase and the formation of domains during this process in melilites are also not yet clear. Another open question remains the possible contribution of occupational modulation in addition to the displacive modulation^[9, 15]. Finally, studies of the structural modulation of Co/Zn-melilites are still lacking.

End-members of melilites like $\text{Ca}_2\text{Al}_2\text{SiO}_7$ and $\text{Ca}_2\text{MgSi}_2\text{O}_7$ have potential applications as laser active materials^[20, 21] and long-lasting phosphorescent materials^[22-24]. Detailed knowledge of the structure is a prerequisite for the exploitation of the appropriate material. On the other hand, because the melilite family occurs in igneous rocks which come from continuous crystallization of magma compositions with falling temperature, investigations of crystals of the melilite system are also important to understand the formation of rocks.

This work will contribute to a better understanding of the fundamentals of the structural modulation and its formation mechanisms in melilites as well as of the correlation between the domain structure formed during phase transition and the modulation. To begin it was necessary to find out the optimum conditions for growing high-quality single crystals of the series $\text{Ca}_2\text{Mg}_{1-x}\text{Zn}_x\text{Si}_2\text{O}_7$, $\text{Ca}_2\text{Co}_{1-x}\text{Zn}_x\text{Si}_2\text{O}_7$ and $(\text{Ca}_{1-x}\text{Sr}_x)_2\text{CoSi}_2\text{O}_7$ by the floating zone melting technique. Then the aim was to investigate the variations of the modulation with composition and temperature, and to find out the features occurring during transitions from the incommensurate phase to the normal phase and to the low-temperature commensurate phase as well as the details of the domain formations. Electron microscopy, electron and X-ray diffraction techniques, X-ray analytic methods as well as differential scanning calorimetry were applied as the main methods for the present studies. Preliminary investigations were done to find out the effects of Cr and Eu doping on the structure and the optical behavior of $\text{Ca}_2\text{MgSi}_2\text{O}_7$ and $\text{Ca}_2\text{CoSi}_2\text{O}_7$ melilites.

2 Structure modulation of melilites

2.1 General aspects of incommensurability

As pointed out in the introduction, in crystal diffraction patterns additional reflections can be observed besides the main lattice reflections, indicating the existence of additional ordering schemes. Such crystals may have an incommensurate crystal structure and can not be described by three-dimensional crystallographic space groups.

An incommensurate crystal can be described in terms of a basic structure with three-dimensional space group symmetry and a periodic deviation (the modulation) which in the incommensurate phase has a period that does not fit to the lattice of the basic space group. According to the different origin causing the modulation, one can class them as the following:

(1) If the modulation consists of displacements one has a displacively modulated structure (Fig.2.1.1a);

(2) If the modulation involves a variation of the occupation probability of given atoms at crystallographic sites of the basic structure one has an occupation-modulated structure (Fig.2.1.1b);

(3) A system consisting of at least two subsystems whose basis structures are mutually incommensurate is called an incommensurate composite structure (Fig.2.1.1c).

Fourier wave-vectors of a modulated crystal phase can be expressed as:

$$\mathbf{h} = h\mathbf{a}^* + k\mathbf{b}^* + l\mathbf{c}^* + m\mathbf{q} \quad (2.1.1)$$

where \mathbf{a}^* , \mathbf{b}^* , \mathbf{c}^* are the basic vectors of the reciprocal lattice of the basic structure, \mathbf{q} is the modulation vector of the reciprocal lattice, and m is integer. In this case the rank of the quasi-lattice is four and its dimension three. In general, the modulation is multiperiodic and involves several wave vectors \mathbf{q}_j . Then, the quasi-lattice to which the diffraction spots belong is

$$M^* = \left\{ \sum_{i=1}^3 h_i \mathbf{a}_i^* + \sum_{j=1}^d m_j \mathbf{q}_j \right\} \quad h_i, m_j \text{ integers} \quad (2.1.2)$$

The rank of the quasi-lattice is $3 + d$, where d is called the dimension of the modulation.

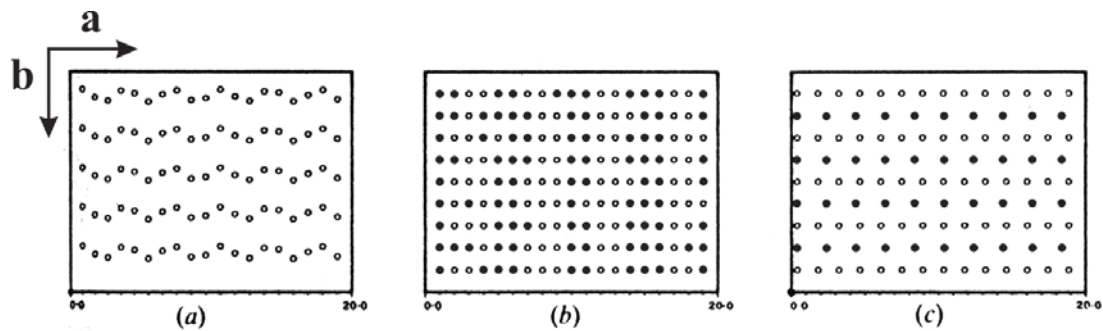


Fig.2.1.1 Three types of incommensurate crystal phases. (a) Transversal displacive modulation with wave-vector $0.2881\mathbf{a}^*$; each atom is displaced in the b direction. (b) Occupation modulation: the probability for finding an atom **A** (full circles) at a lattice position \mathbf{n} is given by $\cos(\mathbf{q} \cdot \mathbf{n})$, with $\mathbf{q} = 0.2881\mathbf{a}^*$. In the planes perpendicular to the a axis the atoms **A** are distributed statistically with this probability. At the remaining positions atoms **B** (open circles) are found. (c) Composite structure: two lattices are simultaneously present, one with lattice constants a , b and c , the other with a' , b and c , respectively, with irrational $a'/a = 1.4085$. (Reproduced from Janssen and Janner ^[25])

Satellite peaks may be temperature dependent. Thus, the incommensurate crystal phase varies as a function of temperature. Many compounds including melilites exhibit an incommensurate crystal phase in a certain temperature interval, which may vary from one to several hundred degrees. Above this interval a normal crystal phase exists, i.e. the basic crystal structure. At low temperatures the incommensurate crystal phase may convert into a so called lock-in phase if the wave-vectors of the incommensurate crystal phase are in mutually fixed rational relations. However, many compounds behave differently without showing any transition into the lock-in phase.

2.2 The melilite system

The melilite group mainly consists of a solid solution of gehlenite, $\text{Ca}_2\text{Al}_2\text{SiO}_7$, and åkermanite, $\text{Ca}_2\text{MgSi}_2\text{O}_7$, with variable amounts of $\text{CaNaAlSi}_2\text{O}_7$ and $\text{Ca}_2\text{FeSi}_2\text{O}_7$. Melilites occur in natural rock assemblages and have the general formula $\text{X}_2\text{T}^1\text{T}^2_2\text{O}_7$. They have also been synthesized for a wide range of chemical composition, i.e. with $\text{X} = \text{Ca}, \text{Sr}, \text{Ba}, \text{Na}, \text{La}$, $\text{T}^1 = \text{Co}, \text{Mg}, \text{Fe}, \text{Cr}, \text{Zn}, \text{Al}, \dots$, and $\text{T}^2 = \text{Si}, \text{Al}, \text{Ge}, \text{Ga}, \text{Be}, \dots$ ^[7]. The average structure of melilite, firstly determined by Warren ^[26] and revised by Smith ^[27], consists of layers of corner sharing $[\text{T}^2\text{O}_4]$ and $[\text{T}^1\text{O}_4]$ tetrahedra, as shown in Fig.2.2.1a. The eight-fold coordinated X cations provide the connection between adjacent layers (Fig.2.2.1b) The symmetry of the average structure is tetragonal with space group $P\bar{4}2_1m$.

The $[T^2O_4]$ tetrahedra occur as $[T^2_2O_7]$ dimers linked by O_1 atom. The four O_3 atoms in the layer plane are linked to $[T^1O_4]$ tetrahedra. The vertices of the dimer tetrahedra are either both pointing up or both pointing down with respect to the layer plane. The $[T^1O_4]$ tetrahedra have one of their binary axes perpendicular to the layer plane. The two upper corners are linked to the $[T^2_2O_7]$ dimer with tops pointing down, whereas the two lower corners of the $[T^1O_4]$ tetrahedra are linked to the $[T^2_2O_7]$ dimers with tops pointing up. The resulting sheets are rather thin, and their thickness is roughly the height of one $[T^2O_4]$ tetrahedron. This corner share results in an irregular pentagonal arrangement of tetrahedra. This arrangement forms channels which are filled with large X-ions located about halfway between the sheets. A side view of the structure is shown in Fig.2.2.1b.

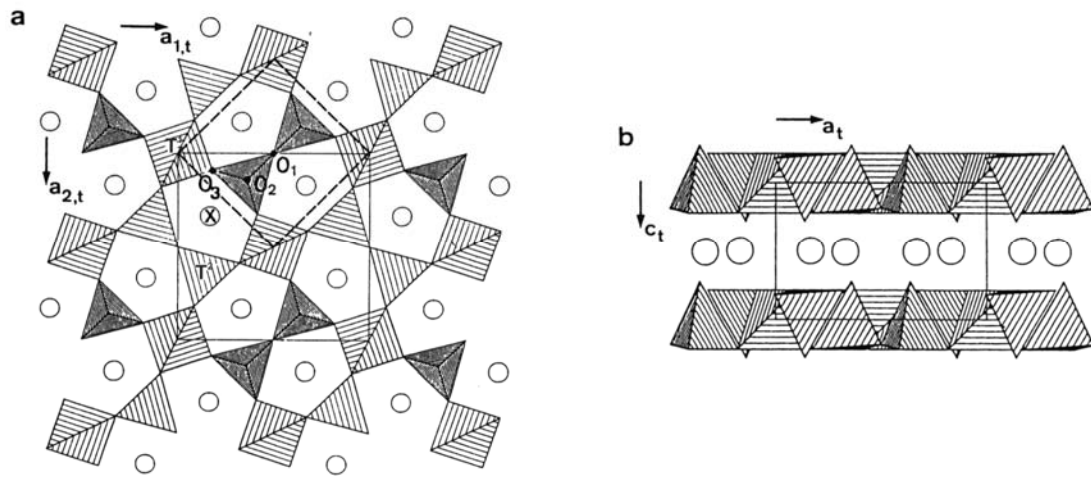


Fig.2.2.1 Structure of melilite ($X_2T^1T^2O_7$). (a) The $[T^1O_4]$ and $[T^2O_4]$ tetrahedra are projected on the c-plane as squares and triangles, respectively. A subunit containing a $[T^2_2O_7]$ dimer is outlined with dashed lines. The open circles represent the X-ions positioned halfway between the sheets as can be seen in (b). (Reproduced from von Heurck et al., 1992 ^[28])

2.2.1 Temperature dependence of the structure modulation

In synthetic $Ca_2MgSi_2O_7$, Hemingway et al. ^[4] observed that the set of strong main reflections is accompanied by weak satellite reflections, indicating an incommensurate modulation. With *in situ* heating in the transmission electron microscope, the intensity of the satellite reflections decreased significantly at temperatures above 358K and disappeared completely at about 580K. Hemingway et

al. concluded that this behavior is associated with local displacements of calcium ions from the mirror plane and accompanying distortion of the tetrahedral sheets.

The synthetic series $\text{Ca}_2\text{Mg}_{1-x}\text{Fe}_x\text{Si}_2\text{O}_7$ ($0 \leq x \leq 0.7$) exhibit at room temperature an incommensurate phase^[5]. Satellite reflections along [100] and [110] in the reciprocal lattice are observed and the distance of the satellites decreases with temperature, thus the corresponding wavelength of the modulation, which is incommensurate with respect to the average melilite structure, increases with temperature. Increasing temperature leads to increasing diffuseness of all satellites, but the effect is stronger for satellites on [100] than on [110]. The satellite peaks disappear at 130°C. When lowering the temperature the satellites reappear at the same transition temperature and attain the same intensity and position as before heating. This indicates that the phase transition is completely reversible.

Schosnig et al.^[11] investigated the temperature dependence of the phase transition from the normal to the incommensurately modulated structure of $(\text{Ca}_{1-x}\text{Sr}_x)_2\text{MgSi}_2\text{O}_7$ ($x = 0.04, 0.08, 0.16, \text{ and } 0.22$) åkermanites by electron diffraction. The value of the modulation wavelength λ calculated from the corresponding patterns at different temperatures reveals that the change of the modulation wavelength also strongly depends on temperature.

The variation and disappearance of the satellites with increasing temperature up to 355K corresponds to the transition from the incommensurate to the normal phase. The temperature dependent shift of the satellite reflections and the fact that incommensurate phases are often intermediate between a high temperature parent structure and a low temperature superstructure led to the prediction of a commensurate low temperature phase. This has been proved by Riester and Böhm^[29] on the basis of the investigation of $\text{Ca}_2\text{CoSi}_2\text{O}_7$ between 30K and 600K using X-ray single crystal diffraction.

In Fig.2.2.2 the temperature dependence of the q -value is shown. The phase transition between the incommensurate and the commensurate lock-in structure is characterized by a prominent hysteresis, which spans over 110K. The low temperature phase transition is observed at a higher temperature than predicted by Seifert and Röthlisberger. The cause for this may be the lack of thermodynamical equilibration in their experiments or just a difference in the thermal history during the synthesis of the

sample. In addition, the second order phase transition occurs at 498(1) K which is 5K higher than the value given by R othlisberger et al. [7] and Hagiya et al. [12].

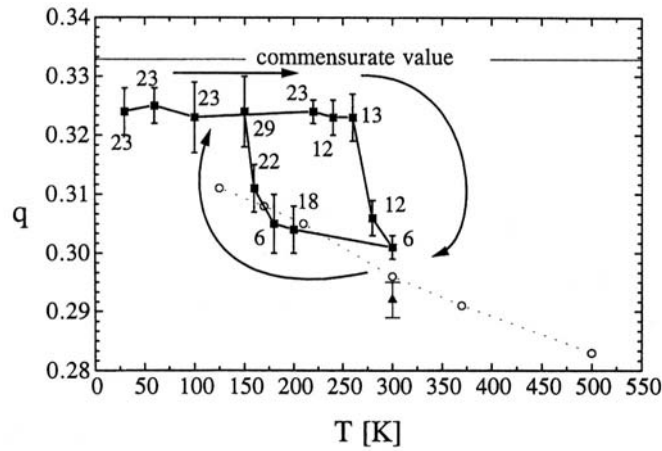


Fig.2.2.2 The q -value as a function of temperature for the compound $\text{Ca}_2\text{CoSi}_2\text{O}_7$, revealing the first order phase transition into the low temperature phase. The sequence of the measurement is indicated by arrows, the numbers indicate the equilibrium time in hours. The q -value at 300K of the juvenile sample is given as a solid triangle. The values of Seifert et al. are given as open symbols (dashed line) (Reproduced from R othlisberger et al., 1990 [7])

The transition from the incommensurate to the commensurate lock-in phase in $\text{Ca}_2\text{CoSi}_2\text{O}_7$ is also investigated by means of electron diffraction and transmission electron microscope [30]. The modulation q -vector calculated from the electron diffraction patterns change from 0.295 at 300K to 0.320 at 100K. Though such value is a bit different comparing to that measured by single crystal X-ray diffraction [29], the q -vector always increases during the phase transition from the incommensurate to the commensurate lock-in structure.

In a word, the dependence of the modulation in melilites on temperature can be generalized as follows: the incommensurate phase is an intermediate phase, which transforms into the unmodulated normal phase at high temperature or into the commensurate lock-in phase at low temperature. There is no hysteresis between the incommensurate and the normal phase transition, but a prominent hysteresis is found between the incommensurate and the commensurate lock-in phase transition, which may be due to the formation of domains as observed by Schaper et al. [30]. In addition, Schosnig et al. [11] divides the incommensurate phase into the high temperature, low ordered phase and into the low temperature, high ordered phase according to the satellites intensity observed from the electron diffraction patterns.

2.2.2 The compositional dependence of the structure modulation

Besides the dependence of the modulation in melilites on temperature, the composition of melilites likewise influences the modulation. This has been investigated in detail by synthetic melilites on the join $\text{Ca}_2\text{MgSi}_2\text{O}_7$ (åkermanite) – $\text{Ca}_2\text{FeSi}_2\text{O}_7$ (iron åkermanite) [5]. The modulation wavelength decreases with increasing Fe content in tetrahedral Mg sites. In pure $\text{Ca}_2\text{MgSi}_2\text{O}_7$ all satellite peaks are sharp. With increasing Fe content the intensity between the satellites on [100] and [110] becomes diffuse forming a ring around the main peaks.

A compilation of different synthetic melilite-type compounds including phase-transition temperatures, synthesis temperature and investigation techniques is given by Röhlichberger et al. [7]. The incommensurate phase and its transition to the unmodulated normal melilite structure can be followed by a variety of techniques, such as calorimetry and single-crystal X-ray diffraction [4], ^{57}Fe Mössbauer spectroscopy [5], ^{29}Si MAS NMR [31]. However, transmission electron microscopy and electron diffraction provide the most direct and sensitive information [4]. Most of the observed phase transition data are therefore based on electron diffraction measurements.

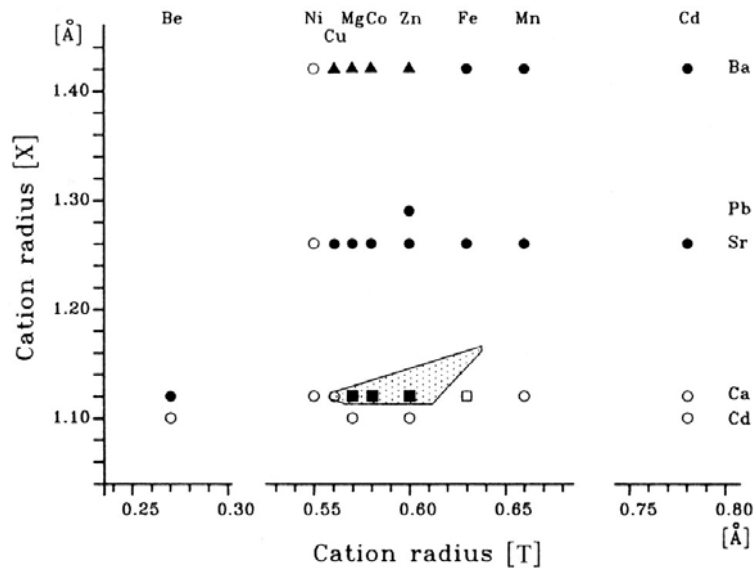


Fig.2.2.3 Structural stability field of $\text{X}_2\text{TSi}_2\text{O}_7$ end-member melilites as a function of the cation radii [X] and [T]. Filled circles: melilite structure; filled triangles: $\text{Ba}_2\text{CuSi}_2\text{O}_7$ structure type; filled squares: melilite structure, modulated at room temperature; unfilled square: metastable melilite [32]; unfilled circles: no compound of this stoichiometry. The stippled area defines the range of compositions, including solid solution series, in which the melilites are modulated at room temperature (Reproduced from Röhlichberger et al., 1990 [7]).

For $X_2TSi_2O_7$ melilites the structural stability diagram in terms of ionic radii of X and T cations is taken from R othlisberger et al. [7] and shown in Fig.2.2.3. The field of modulated melilites at room temperature is indicated. As hypothesized by Seifert et al. [5], the modulated phases are restricted to an area close to the border of the melilite structural field towards larger T and smaller X cations. The end-member melilites $Ca_2TSi_2O_7$ with $T = Fe^{2+}$, Mn and Cd are not stable. With increasing r_T an increasing amount of Sr substituting for Ca is required to stabilize the particular melilite structure. The incommensurately modulated phases extend in general to higher Sr contents with larger r_T , but for $r_T > r_{Fe^{2+}}$ the field of the modulated structures is truncated by the overall instability of such melilites of high Ca contents.

The effects of more complex substitutions on the stability of the modulated phase can be rationalized as follows. Starting from $Ca_2MgSi_2O_7$, the ‘‘gehlenite’’ substitution 2Al for Mg + Si will decrease the average tetrahedral radius from 0.363 to 0.347 . Similarly, starting from $Ca_2ZnGe_2O_7$, the 2Ga for Zn + Ge substitution decrease the average tetrahedral radius from 0.460 to 0.443 . The observed decrease in stability of the modulated phase upon these substitutions is consistent with the above deductions of Seifert et al. On the other hand, the substitution of $Fe^{3+} + Al$ for Mg + Si increases the average tetrahedral radius from 0.363 to 0.383 , but instead of the expected stabilization of the incommensurate structure, the modulation disappears at room temperature.

In general, the transition temperature, T_{N-IC} , from the unmodulated high-temperature structure to the incommensurately modulated structure strongly depends on the composition of the phase. T_{N-IC} increases with increasing ionic radii of the two types of tetrahedrally-coordinated cations by increasing the dimensions of the tetrahedral sheet. The concept of a misfit between the size of the interlayer cation and the size of the tetrahedral sheet is used to explain the absence of an incommensurate phase in Ba- and Sr-melilites [33].

2.3 Mechanisms of the structure modulation in melilites

Since the phenomenon of the structural modulation was found in melilites [4], scientists have been devoting themselves to pursue the nature causing modulation. By substituting different ions for X or T in $X_2T^1T^2O_7$ melilites Seifert et al. [5] proposed

that the incommensurate phase is based on the misfit between the tetrahedral ($T^1Si_2O_7$)⁴⁻ sheets and the Ca^{2+} ions.

A first structural model for the incommensurately modulated melilites has been presented by van Heurck et al. [28] on the basis of their transmission electron microscopy investigations of $Ca_2ZnGe_2O_7$. Their model consists of commensurately modulated micro-domains that are separated by antiphase boundaries. Statistical fluctuations of the size of such domains yield an incommensurate average of the modulation period. The domains are characterized by octagonal arrangements of Zn-tetrahedra which form various ordering schemes and vary with temperature.

A structure determination for the incommensurate structure of $Ca_2CoSi_2O_7$ from X-ray data in the (3+2)-dimensional space has been reported by Hagiya and Ohmasa [12]. The satellites indicate that the modulation is two-dimensional with wavevectors $\mathbf{q}_1 = \alpha (\mathbf{a}^* + \mathbf{b}^*)$, $\mathbf{q}_2 = \alpha (-\mathbf{a}^* + \mathbf{b}^*)$. All reflections could thus be written in terms of five integers $hklmn$ and five vectors in the five-dimensional expression [34] $\mathbf{h} = h\mathbf{a}^* + k\mathbf{b}^* + l\mathbf{c}^* + m\mathbf{q}_1 + n\mathbf{q}_2$. Using the least-squares program *REMOS* developed by Yamamoto [35] the modulated structure of $Ca_2CoSi_2O_7$ has been refined according to the multidimensional treatment.

The Ca-O bond lengths depend on the Ca coordination. The SiO_4 tetrahedron does not behave as a rigid body, i.e. the distortion of the Si-O bonds is variable throughout the crystal in agreement with the interpretation of the ²⁹Si NMR spectra observed by Merwin et al. [31] and of the Mössbauer spectra measured in synthetic iron-bearing $Ca_2MgSi_2O_7$ [5]. Variations of the Co-O bond lengths in the T^1O_4 tetrahedra show a feature different from those of the Si-tetrahedra. All four Co-O bond lengths change simultaneously. A histogram of the mean Co-O bond lengths shows two peaks which probable correspond to a compressed and a normal Co-tetrahedra.

Kusaka et al. [18] have studied the details of the incommensurate structure of $Ca_2(Mg_{0.55}Fe_{0.45})Si_2O_7$ and $Ca_2CoSi_2O_7$, and proposed that these structures are characterized by an octagonal arrangement of bundles along the c -axis that are composed of four arrays of six-coordinated Ca polyhedra and a central array of T^1O_4 tetrahedra. The ratio of the six-coordinated Ca sites to all Ca sites in Co-åkermanite (28.5%) is larger than that in $Ca_2(Mg_{0.55}Fe_{0.45})Si_2O_7$ (17.8%). The distribution and the number of the octagons in these bundles vary with the modulation wavelength [36].

The structure determination of the lock-in phase of synthetic $\text{Ca}_2\text{CoSi}_2\text{O}_7$ elucidates the driving forces of the modulation in melilites ^[16]. Two approaches have been applied: a conventional refinement using a (3×3)-fold superstructure and a refinement in the (3+2)-dimensional superspace. The representation of the lock-in structure shows the distortion of the tetrahedral layer and the correlated displacements of calcium atoms. The calculations of the bond lengths revealed six-, seven-, and eight-fold oxygen coordinations for calcium. The atoms (Ca, Si, O(2)) are significantly displaced from their former special positions in the non-modulated phase. The displacement patterns of Ca and Co become apparent in the partial Fourier synthesis of the satellite reflections. Within the tetrahedral layer the largest displacements are observed for the bridging oxygen atoms O(1) and O(3). The distortion of the tetrahedral layer is based mainly on rotations of the SiO_4 - and CoO_4 -tetrahedra. The rotational distortions in the tetrahedral layer are accompanied by displacements of the central atoms. The bond valence calculations revealed the expected valences for Co^{2+} and Si^{4+} . The calculated valence sums for all nine symmetrically independent Ca atoms, however, are too small. This can be explained by the high degree of distortion of the Ca coordination.

In the non-modulated phase calcium is coordinated by eight oxygen atoms in a distorted quadratic antiprism with four shorter and four longer bond distances. In the incommensurate phase the increase of the distortion of the calcium coordination polyhedra results in six-fold Ca coordination ^[12]. For the lock-in structure the coordination of 2/3 of Ca sites is lower than eight-fold. The six- and seven-fold coordinated calcium atoms show the largest distortion of the structure. The strong distortion of the tetrahedral layer is obvious because the tilt angle can be up to 28° ^[16]. The number of lower coordinated calcium increases with decreasing temperature. This process starts in the non-modulated phase when the thermal vibrations become too small for a proper fit of calcium in the quadratic antiprism. At temperatures above the normal to incommensurate phase transition the distortions are distributed statistically and can be observed spectroscopically ^[5].

As suggested by Kusuka et al. ^[37] the six-fold coordinated Ca form an ordered distribution of clusters around the CoO_4 tetrahedra, forming centered octagons in the (3×3×1) super cell. The clusters with six-fold coordinated calcium sites are ordered in

domains with an average size of about $(7 \times 7 \times 1)$ unit cells of the basic structure. The average domain size is temperature dependent.

Such a centered octagonal arrangement agrees with TEM observations of incommensurately modulated $\text{Ca}_2\text{ZnGe}_2\text{O}_7$ at room temperature ^[28]. The centered octagonal arrangements vary with temperature. The change from an octagonal arrangement with diameter $\phi = 4$ subunits and a tentative overlap of these units in the incommensurate phase to a centered octagonal arrangement with diameter $\phi = 3$ subunits in the lock-in phase is confirmed by high-resolution transmission electron microscope (HREM) images ^[30]. In the lock-in phase the octagonal arrangements are regarded as completely overlapping. This leads to a more general approach of understanding of the structural modulation in melilites. The driving force for the modulation in order to release internal stress leads to the formation of domains with clusters arranged in octagons which represents an energetically favorable pattern.

On the basis of the results derived from an electron microscope imaging and electron diffraction study, Jiang et al. ^[9] showed that an occupational modulation also contributes to the overall modulation characteristics, as a consequence of the ordered distribution of Sr. Accordingly, Bagautdinov et al. ^[15] found a sinusoidal form of the occupancy modulation of Sr and Ca in the incommensurately modulated structure of $(\text{Sr}_{0.13}\text{Ca}_{0.87})_2\text{CoSi}_2\text{O}_7$.

3 Experimental methods

3.1 Single-crystal growth method and apparatus

3.1.1 Double ellipsoid mirror furnace

The floating zone (FZ) melting method is developed from the zone melting technique, which is used to refine solid materials. In this method a molten zone is held between two vertical collinear solid rods by its surface tension. Normally, temperatures $> 1000^{\circ}\text{C}$ should be attainable for melting a raw material, thus the heat source and the design to focus energy are very important. The ellipsoid mirror furnace using focused light provides an efficient and compact way for a local heating, especially for high temperature applications. The two main components of the ellipsoid mirror furnace are the ellipsoidal reflectors and the lamps. The simplest geometry for a mirror furnace is a closed ellipsoid of rotation with one lamp, so-called mono-ellipsoid mirror furnace. If such a furnace is equipped with a device providing translation and rotation movements of the raw material rod it is also suitable for crystal growth experiments.

The application of such a mono-ellipsoid furnace is limited. The available radiation energy is determined by the power rating of the lamp. A larger filament of the lamp could deliver more power but decreases the furnace performance because of worse focusing properties. Therefore, a two-ellipsoid arrangement consisting of two ellipsoids has been developed.

A double-ellipsoid is to be preferred because it provides a much better peripheral thermal distribution of energy than a mono-ellipsoid, although the latter has maximum thermal efficiency. The double-ellipsoid is especially suitable for high-temperature crystal growth because the power needed to melt a sample is divided up between two halogen lamps. The small loss in efficiency is far outweighed by the fact that two lamp filaments of favorable size can be operated at an electrical power rating far below breakdown, resulting in a longer lamp life and a safer operation of the furnace. Considering the demands for high efficiency, thermal symmetry, good focusing properties and technical feasibility, a double-ellipsoid arrangement with axes $a = 90$ mm and $b = 80$ mm ($b/a = 0.88$) has usually been used.

3.1 Single-crystal growth method and apparatus

For all experiments of single crystal growth we used a double-ellipsoid mirror furnace shown in Fig.3.1.1. It consists of (1) growth furnace; (2) pulling-rotation system; (3) cooling unit; (4) visualizing system and (5) power supply system. If the furnace is equipped by a sealed system, crystals can also be grown in protecting atmospheres.

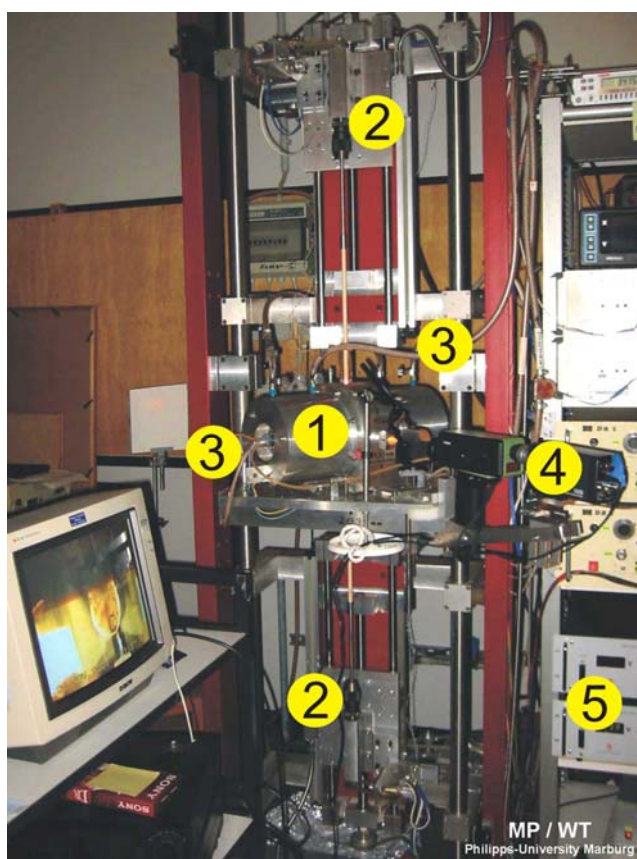


Fig.3.1.1 A double-ellipsoid mirror furnace. Numbers 1-5 see text.

The growth furnace (see (1) in Fig.3.1.1) is the most important part in the whole set ups. The enlarged cross-section scheme is shown in Fig.3.1.2. It includes two ellipsoidal mirrors. There is one halogen lamp (120 V, 1 kW) on each side. The radiation heat from two halogen lamps is reflected by the ellipsoidal mirrors and focused on an area of *ca.* 8mm length, which is the high temperature zone. Based on the output of the halogen lamp a maximum temperature of about 2000°C can be reached. This temperature is higher than the melting point of many inorganic compounds and, therefore, this furnace can be used for synthesis of many kinds of

compounds. The growth chamber is a long quartz tube with 2.8 cm diameter and 50 cm length.

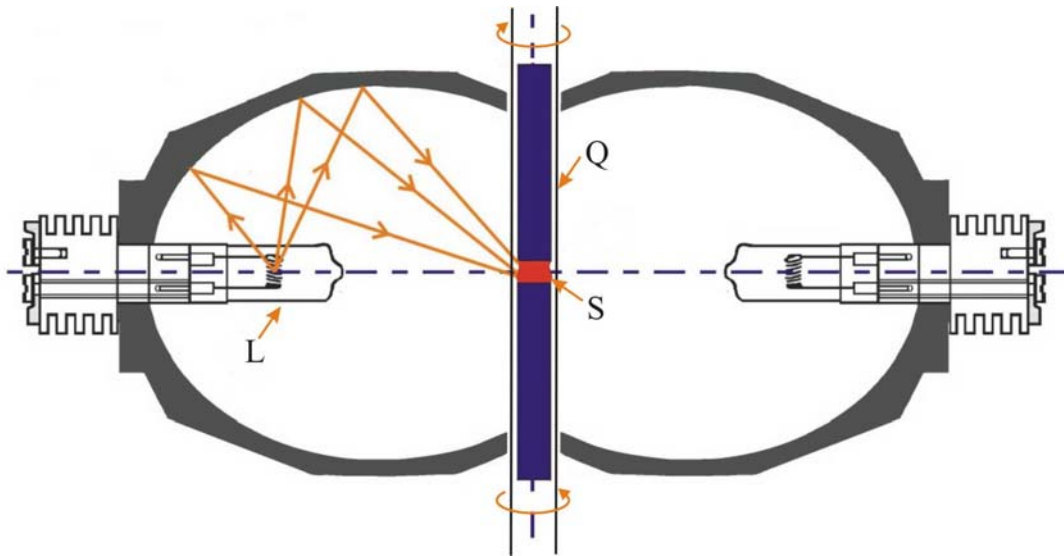


Fig.3.1.2 A scheme of mirror furnace. L – Halogen lamps; S – Melting zone; Q – Quartz tube. ($a = 90\text{mm}$, $b = c = 80\text{mm}$, $b/a = 0.88$)

The rotation and translation (see (2) in Fig.3.1.1) of the rod as well as of the seed crystal are controlled independently through four micro-stepping motors. Normally, the rod is mounted on the upper shaft and the seed crystal is fixed on the lower one. By controlling the traveling speed of these two parts, crystals with different diameter can be grown. The initial touch between the seed crystal and the molten raw material is very critical for the formation of a stable interface.

The rotation equipment with different adjustment steps enables to choose a suitable rotation speed. In course of growing a crystal, a concave or convex interface will be formed due to the properties of the polycrystalline raw material. But these interfaces do not benefit to grow a single crystal. Therefore, the relative rotating speed is adjusted to get a relative flat interface.

A good cooling unit (see (3) in Fig.3.1.1) is necessary for running the mirror furnace at high temperatures. Because the lamps give off plenty of heat energy during growing process, the lamp holder can reach very high temperatures, which is disadvantageous for long-time crystal growth. Also, the mirror furnace absorbs less amount of infrared radiation and is getting hot. The cooling water cycle around two

halogen lamps and the mirror furnace is used to keep an acceptable temperature during the crystal growth.

A CCD-camera equipped with a monitor (see (4) in Fig.3.1.1) is used for watching the whole growing process. Visualization enables to modify growth parameters during growing and, hence, to gain high quality single crystals. It is especially helpful for the adjustment of the stable interface. The FZ melting method combined with a visualizing system is the most prominent feature comparing to the Czochralski and the Bridgman-Stockbarger method.

The required temperature of the zone can be obtained by regulating the input voltage (see (5) in Fig3.1.1) of the two halogen lamps. It should be noted that the position and the shape of the lamp can affect, for example, the zone area, the maximum temperature, the temperature gradient etc. As we know, the temperature gradient is absolutely critical for the quality of single crystals; therefore, the position of the lamp is adjusted and fixed before starting the growth procedure.

3.1.2 Factors affecting single crystal quality

As outlined above, a double-ellipsoid mirror furnace is a good choice to grow single crystals using the FZ melting method. However, there are several factors which affect the growth of high quality crystals and, therefore, have to be considered during growing process.

The zone length is one of the most important operational parameters. From the condition of the stability the inward pressure on the planar surface of the liquid due to surface tension should be equal at all points and opposite to the pressure exerted by the liquid head. It is shown that the maximum height of the liquid, l_m , which can be supported in a floating zone technique, is given by the expression ^[38]

$$l_m \approx 2.8 \sqrt{\frac{\gamma}{\rho g}} \quad (3.1.1)$$

where γ is the surface tension of the liquid; ρ is the density of the liquid and g is the gravitational acceleration. The maximum height of the liquid is related to the radius of the rod, which is shown in Fig.3.1.3.

In general, l_m increases with increasing radius of the rod. It should be noted that this curve does not indicate any upper limit on the diameter of the rod. It must be emphasized that equation (3.1.1) provides only a guide line for the selection of the

zone length. The actual shape and the stability of the zone is greatly modified by the degree of stirring and the thermal conductivity of the solid rod because these parameters affect the curvature of the solid/liquid interface.

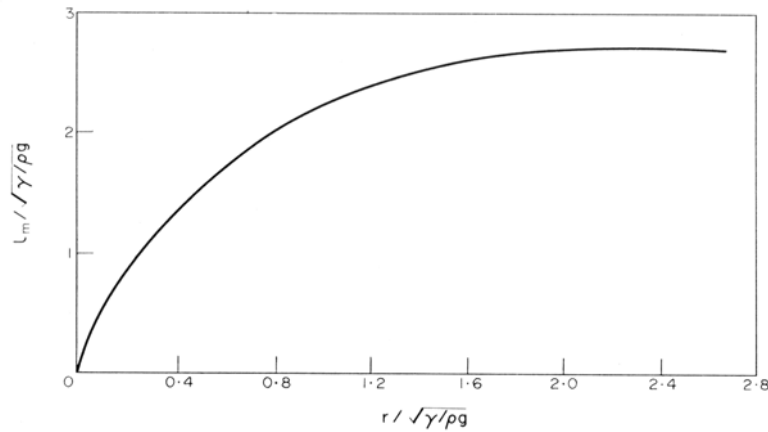


Fig.3.1.3 Variation of a maximum stable height, l_m , of a floating zone versus radius, r , for cylindrical rods. (Reproduced from Heywang, 1956^[38])

The thickness of the diffusion layer at the solid/liquid interface is a function of growth velocity. Therefore, the vertical zone velocity is one of the determining factors for the shape of the solid/liquid interface. The onset of interface stability such as constitutional supercooling is inherently dependent on the zone vertical-moving velocity, the concentration of the solute and the temperature gradient at the solid/liquid interface. It is therefore necessary for a homogeneous single phase single crystal production to select the vertical-moving velocity with due care. Generally speaking, slower growth rates are advantageous for producing perfect crystals. On the other hand fast growth speeds may enable one to avoid interface instabilities simply because a fast growth does not permit the diffusion processes to build an enhanced impurity layer at the interface.

The temperature gradient at the solid/liquid interface is an important parameter governing the onset of interface instability. A correct combination of the imposed temperature gradient and traverse speed is essential for avoiding micro-segregation. The imposed temperature gradient depends on the nature of the heat source, thermal conductivity of the ingot material and other modes of heat losses. It should be noted that the magnitude of the temperature gradient would affect the zone length and the degree of mixing in the zone.

3.2 Electron microscopy

3.2.1 Transmission electron microscopy

3.2.1.1 Image formation in the TEM

The image formation in the electron microscope consists of three consecutive processes: electron scattering in the specimen and formation of the exit wave, formation of diffracted beams at the back focal plane of the objective lens, and formation of an image in the image plane. Accordingly, the electron optical system of a TEM can be approximated by the schematic principle shown in Fig.3.2.1.

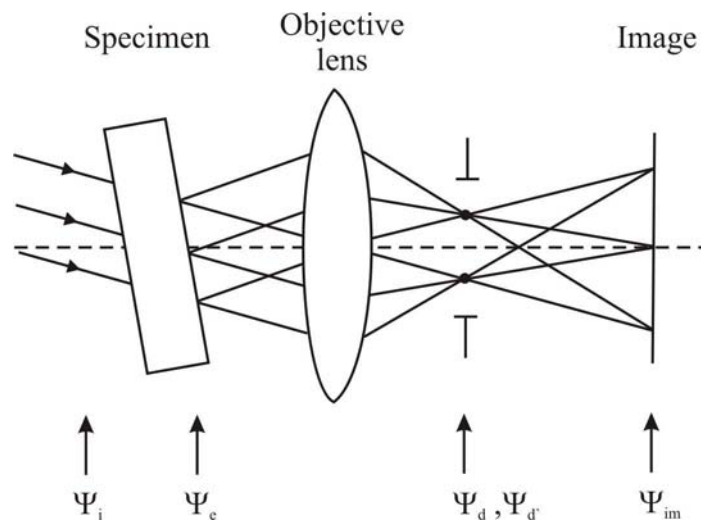


Fig.3.2.1 Electron optical system of image formation in TEM. Ψ_i – the incident electron wave function; Ψ_e – the exit-surface wave function; Ψ_d – the diffraction pattern; $\Psi_{d'}$ – the corrected diffraction pattern; Ψ_{im} – the wave function in the image plane (according to ^[39]).

The electron wave ψ_i striking on the specimen depends on the characteristics of the electron source (gun) and the condenser lens and can be described as a plane wave of the form

$$\Psi_i = \Psi_0 \exp(-ikr) \quad (3.2.1)$$

where \mathbf{k} is the wave vector and $|\mathbf{k}| = 2\pi/\lambda$ the wave number, \mathbf{r} is the position vector. The wavelength λ of the incident wave is determined by the principle of conservation of energy of an electron in a potential field U :

$$\lambda = \frac{h}{mv} = \frac{h}{\sqrt{2meU}} \quad (3.2.2)$$

where h is Planck's constant, v is the velocity of the electron, m and e are the electron mass and charge, respectively. Taking into account the relativistic variation of the mass of the electron at high energies the relativistic mass of an electron can be expressed as

$$m = \frac{m_0}{\sqrt{\left(1 - \frac{v^2}{c^2}\right)}} \quad (3.2.3)$$

where m_0 = electron rest mass, c = velocity of light. Thus, the equation (3.2.2) has to be rewritten as

$$\lambda = \frac{h}{\sqrt{2meU_r}} \quad (3.2.4)$$

where

$$U_r = U_0 + \left(\frac{e}{2m_0c^2}\right)U_0^2 \quad (3.2.5)$$

where U_r is the relativistic accelerating voltage. The equation (3.2.4) shows that the electron wavelength λ relates to the accelerating voltage. Table 3.2.1 lists values of the electron wavelength and the interaction constant σ (see equation 3.2.7) for a number of selected accelerating voltages.

Table 3.2.1

Electron wavelength λ and interaction constant σ at different accelerating voltage V.

Accelerating Voltage, V (kV)	Wavelength, λ (nm)	Interaction constant, σ (V ⁻¹ nm ⁻¹)
100	0.00417572	0.0100871
200	0.00250793	0.0072884
300	0.00196875	0.0065262
400	0.00164394	0.0061214
600	0.00125680	0.0057072
800	0.00102695	0.0055030
1000	0.00087192	0.0053850
1250	0.00073571	0.0052956
1500	0.00063745	0.0052397
2000	0.00050432	0.0051760
2500	0.00041783	0.0051423
3000	0.00035693	0.0051223

Within a crystal, the wavelength of the incident electron wave will be changed by the crystal potential $\phi(r)$ from λ to λ' :

$$\lambda' = \frac{h}{\sqrt{2me(U_r + \phi(r))}} \quad (3.2.6)$$

When the electron wave passes through a thin crystal it undergoes a phase shift which depends on the projected potential in the z -direction. This is illustrated in Fig.3.2.2. The mean inner potential of a sample usually increases with increasing atomic numbers present, and takes values in the range of a few volts to about 30V.

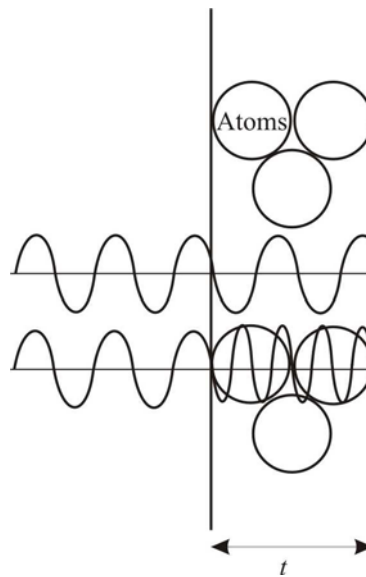


Fig.3.2.2 The electron wave illustrated in two cases passing through a specimen. The wave passing through the centre of an atom (where the potential is high) has its wavelength reduced and so suffers a phase advance relative to the wave passing the specimen between the atoms which experiences little change in its wavelength. (reproduced and processed according to [40]).

The complex exit wave function can be written as

$$\Psi_e = \exp[-i\sigma\phi(r) - \mu(r)] \quad (3.2.7)$$

with $\mu(r)$ representing an absorption function and σ the so-called interaction constant,

$$\sigma = \frac{2\pi me\lambda}{h^2}$$

with relativistically corrected values for λ . σ generally decreases with

increasing acceleration voltage, see Table 3.2.1.

Equation (3.2.7) describes the specimen as a strong phase object. Further simplification for very thin specimens and neglecting considerable absorption is known as the weak phase object approximation (WPOA):

$$\Psi_e(x, y) \approx 1 - i\sigma\varphi(r) \quad (3.2.8)$$

which assumes only kinematical scattering and ignores dynamical scattering in the specimen. The essential meaning of equation (3.2.8) is that the amplitude of a transmitted wave is a linear function of the projected potential of the specimen.

The complex wave amplitude ψ_d in the back focal plane of the objective lens is obtained by Fourier transformation of the transmission function:

$$\Psi_d(u, v) = \delta - i\sigma F[\varphi(r)] \quad (3.2.9)$$

where F represents the Fourier transformation. δ is a delta function which represents the unscattered wave (i.e. the direct beam). However, equation (3.2.9) does not take into account the additional phase shift due to the various aberrations (spherical, chromatic, astigmatism) of the electron beam in the electron microscope. Spherical aberration is introduced by the contrast transfer function (CTF)

$$T(u, v) = A(u, v) \exp[i\chi(u, v)] \quad (3.2.10)$$

where $A(u, v)$ is the aperture function and $\chi(u, v)$ the phase shift due to lens aberrations. Considering only the spherical aberration (C_s), and combining it with a term for the focus error Δf we obtain for the phase shift $\chi(u, v)$

$$\chi = \frac{2\pi}{\lambda} \left(C_s \frac{\lambda^4 u^4}{4} + \Delta f \frac{\lambda^2 u^2}{2} \right) \quad (3.2.11)$$

Relation (3.2.11) emphasizes the following particular aspects:

- 1) It is possible widely to compensate for the spherical lens error by choosing an appropriate defocus value;
- 2) Defocusing allows phase contrast imaging of the object by making visible the phase shift induced by the object potential.

Including the aberration effects, the wave amplitude in the back focal plane can be written

$$\Psi_{d'}(u, v) = \delta - i\sigma F[\varphi(r)] A(u, v) \exp[i\chi(u, v)] \quad (3.2.12)$$

Inverse Fourier transformation of equation (3.2.12) leads to the complex image amplitude Ψ_{im}

$$\Psi_{im} = 1 - i\sigma F[\varphi(r)] \otimes F[A \exp(i\chi)] \quad (3.2.13)$$

where \otimes is the symbol of convolution, and finally, the image intensity is obtained as

$$I = \Psi \Psi^* = |\Psi_{im}|^2 \quad (3.2.14)$$

Carrying out the multiplication in equation (3.2.14) it becomes evident that only the imaginary part of (3.2.10) contributes to the image intensity, i.e. only $\sin\chi$ is responsible for the final image contrast. $\sin\chi$ is a complicated curve that depends on the lens quality of the microscope (C_s) and the so-called ‘‘Scherzer defocus’’ Δf , a measure of the resolution power of the microscope. Fig.3.2.3 shows the contrast transfer function of a JEM 3010 high-resolution TEM with LaB₆ cathode mainly used in this work. The microscope provides a point resolution of 0.167nm.

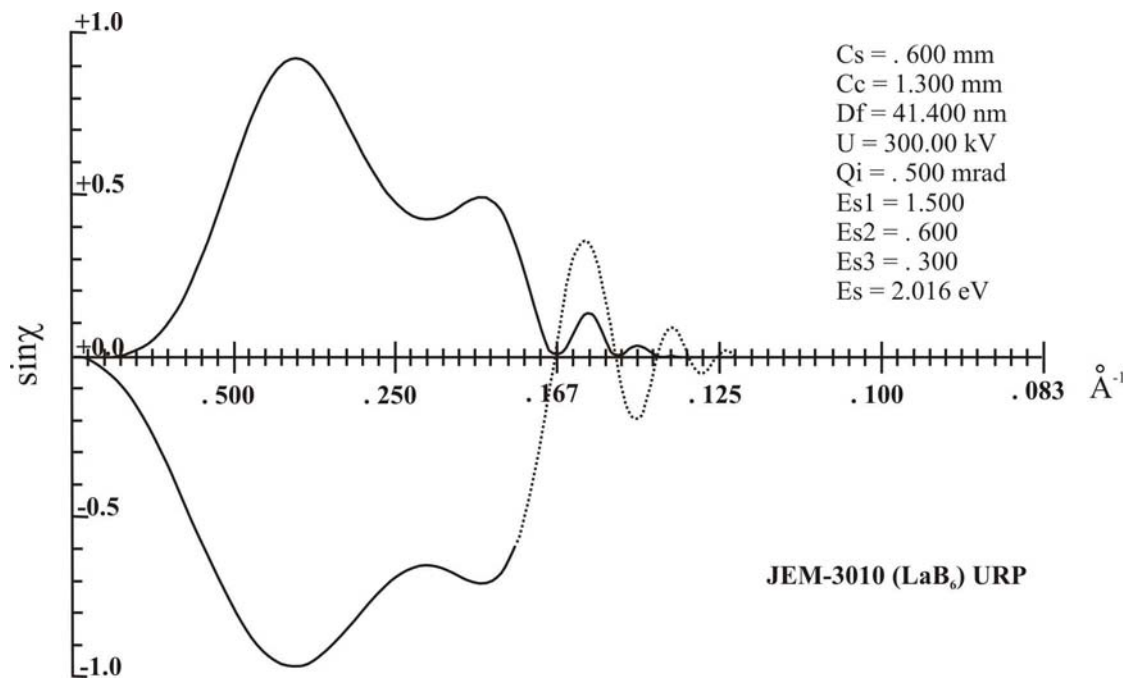


Fig.3.2.3 Phase contrast transfer function of a JEM 3010 microscope operated at 300kV.

3.2.1.2 Practical aspects of diffraction contrast

Besides the phase contrast outlined above, diffraction contrast which is one form of the amplitude contrast is often used in imaging defect structures. When electrons with wavelength λ pass through a crystal of lattice spacing d diffracted waves will be produced at angles 2θ according to the Bragg condition, $2d \sin \theta = \lambda$ (See also 3.4). The diffraction waves form diffraction spots in the back focal plane (Fig.3.2.4). By choosing different diffraction spots using the objective aperture diffraction contrast images are obtained.

Bright-field (BF) and dark-field (DF) images will be formed when an objective aperture selects only the spot formed by the direct electron beam (Fig.3.2.4a) or any diffracted spots (Fig.3.2.4b). The high-resolution image is obtained by choosing both kinds of diffracted spots (Fig.3.2.4c). It emphasizes the information corresponding to the selected diffracted spots. To get strong diffraction contrast the specimen is tilted to two-beam conditions.

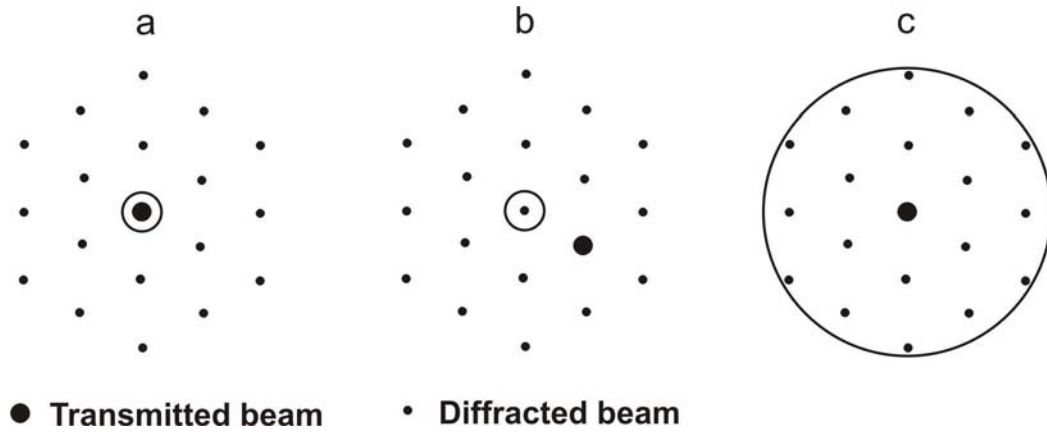


Fig.3.2.4. Three observed modes in electron microscopy using an objective aperture. The center of the objective aperture is assumed to be set to the optical axis. (a) bright-field method; (b) dark-field method; (c) high-resolution electron microscopy (reproduced from ^[41]).

3.2.1.3 Structure factor and crystal potential

The introduction of the structure factor concept is most important in solving crystal structures from high-resolution images and diffraction patterns. The structure factor is defined as

$$F(u) = \sum_{j=1}^N f_j(u) \exp 2\pi i(u \cdot r_j) \quad (3.2.15)$$

where $f_j(u)$ is the atomic scattering factor for atom j and u are coordinates of atom j in three dimensional direction. N is the number of atoms in the unit cell. r_j is the position vector.

The equation (3.2.15) means that the amplitude of the scattering is influenced by the type of the atom, its position in the unit cell and the specific atomic phases contributing to the discrete reciprocal lattice. $F(u)$ is complex and consists of the amplitude $|F(u)|$ and the phase $\phi(u)$

$$F(u) = |F(u)| \exp[i\phi(u)] \quad (3.2.16)$$

The phase depends on the origin chosen of the unit cell (in centro-symmetric structures it is always in the center of symmetry).

The crystal potential $\varphi(r)$ introduced in equation (3.2.6) is closely related to the structure factor $F(u)$:

$$\varphi(r) = \frac{\lambda}{\sigma\Omega} \sum F(u) \exp[-2\pi i(u \cdot r)] \quad (3.2.17)$$

where σ = interaction constant, Ω = unit cell volume. Therefore, if both the amplitudes $|F(u)|$ and the phase $\phi(u)$ of the structure factor are known for all reflections u , the potential $\varphi(r)$ can be determined. This is the key principle in the analysis of unknown crystals within the bounds of Electron Crystallography^[42].

3.2.1.4 Image simulation

Image simulation was originally developed for interpreting experimental high-resolution TEM images because high-resolution images are affected not only by various aberrations but also by dynamical diffraction effects. Interpretation of atomic resolution images taken by HRTEM makes image simulation necessary for confirming the precise atomic positions. Two methods are available^[40], namely, the Bloch wave and the multislice method. The Bloch wave method solves directly the time independent Schrödinger equation and the exit wave function of the crystal is obtained. The multislice method is based on the physical optics approach^[43]. The crystal of the thickness t is sliced into many thin slices of small thickness Δt . For each slice the potential is projected onto a plane and the corresponding projected potential is calculated. The propagation of the electron wave from the exit surface of one slice to the incident surface of the next slice is considered as a Fresnel propagation in vacuum. These two methods may be applied in complementary cases. However, the multislice approach is more frequently used, e.g. in the JEMS software package developed by Stadelmann (http://cimesg1.epfl.ch/CIOL/asu94/ICT_1.html).

3.2.1.5 Instrumentation

In this work mainly a JEOL 3010 TEM with LaB₆ as electron source operated at 300 keV was used. The attainable point and lattice resolutions of the microscope are

0.167nm and 0.14nm, respectively. The microscope is equipped with a 2048 ×2048 CCD camera for image acquisition. The sample can be tilted in two directions along x and y axis up to 20° using the double tilt specimen holder. Phase transitions can be investigated by a double tilt cooling specimen holder (636-DH) in which the sample can be cooled down, using liquid nitrogen, to a temperature of about -170°C. The temperature stability is better than $\pm 1^\circ\text{C}$ in the range from -170°C to -130°C.

The JEOL-ARM1250 „Atomic-Resolution Microscope” at MPI in Stuttgart operating at an accelerating voltage of 1250 keV was used for detecting atomic positions in the studied systems. A point resolution of 0.12 nm can be reached with the “side-entry” goniometer in this microscope.

A cryo-high-resolution microscope JEM-4000SFX operating at 400 keV was also used for additional very low-temperature measurements at liquid He temperature.

3.2.1.6 Specimen preparation for TEM

Because of the strong interaction of electrons with matter, very thin specimen ($< 100\text{\AA}$) should be used for high resolution imaging. Preparation of thin specimens with extremely smooth surfaces is highly important for any TEM investigation, especially for high-resolution TEM structural studies. Such a specimen can be prepared by ion beam milling at low incident angles.

For our TEM investigations, high-resolution structural image of (001) plane is helpful for studying the modulated structure, so the c-axis of the sample should be parallel to the direction of the electron beam, so several steps were taken before final ion milling as shown in scheme 3.2.1.



Scheme 3.2.1 The pre-preparation process before ion milling.

The precession method ^[44] had been used to orient the specimen. According to the reflection dots on the film, we adjusted the goniometer in three directions to make the c-axis of the crystal parallel to the direction of the X-ray beam.

3.2 Electron microscopy

After orientation the crystal of $1\text{mm} \times 1.8\text{mm}$ size was cut from the bulk material. A Well Precision Diamond Wire Saw (Model 3242) was used for this cutting. The diameter of the wire is 0.3mm . The cutting speed and strength depend on the nature of the material. For brittle materials a small cutting speed and strength were applied; otherwise, the material got easily broken.

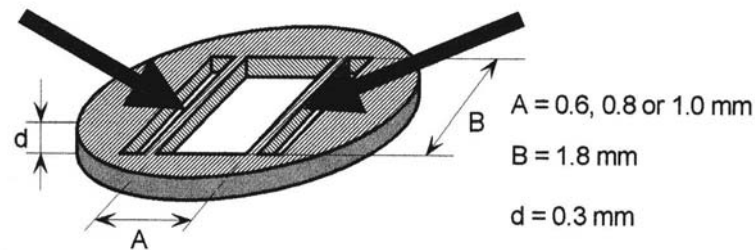


Fig.3.2.5 The Ti-disk for fixing a specimen. (Reproduced from the manual of the Ion Beam Thinning Unit, Technoorg Linda)

The following step was to fix the cut specimen into a Ti disk of 3mm in diameter (Fig.3.2.5) using the glue, G-1, composed of a mixing ratio of 10 (epoxy) : 1 (hardener). A temperature of 120°C was used and the curing time was about 3 minutes. The crystal was aligned with its c-axis normal to the disk plane.

Mechanical grinding was applied to remove damaged surface layers due to cutting. The specimen was put onto a cloth paper with $40\mu\text{m}$ diameter particles and thinned by a Disk Grinder (Model 623, Gatan) till $200\text{-}250\mu\text{m}$ thickness. Then the specimen was thinned and polished in turn using abrasive diamond paper (the diamond sizes: 15, 5, 3, 1, $1/4\mu\text{m}$) by a Micropol Polisher (Linda). Both sides of the specimen were prepared in this way. A specimen of $30\text{-}70\mu\text{m}$ thickness was finally obtained after finest polishing.

For ion milling, high purity Ar was used as the ion source in the Ion Beam Thinning Unit (Model IV3/H/L) from Technoorg Linda and partly in a Precision Ion Polishing System (Model 691) (PIPSTM) from Gatan. The arrangement of the ion milling units of TELETWIN guns from Technoorg-Linda are shown in Fig.3.2.6. The specimen holder together with the sample can be moved along the x and z axis. Two ion guns are in mirror-image position. The angle of incidence of the ion beam can be adjusted either by tilting the sample holder or by tilting the common holder of the guns.

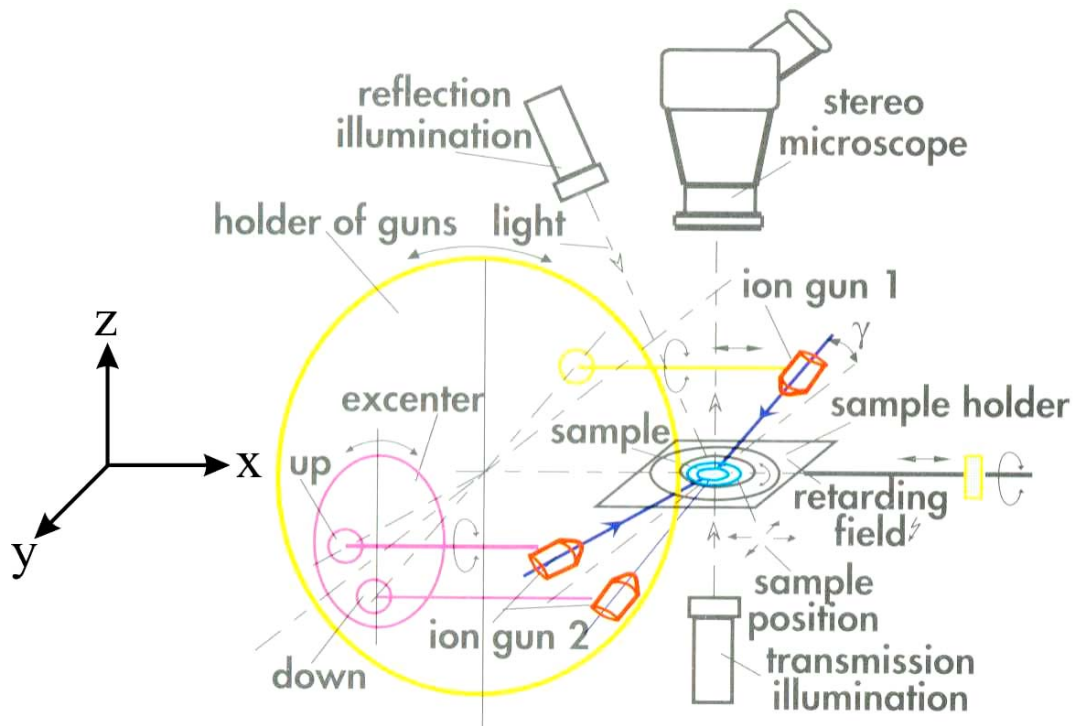


Fig.3.2.6 The TELETWIN ion gun and sample holders. The sample holder located in center can be moved in rotation or oscillation mode. Two ion guns in mirror-image position can be rotated along a axis to adjust a incident angle. The use of a stereo microscope located in the top and the transmission illumination unit is helpful for following the milling process (Reproduced from the introduction of products of Technoorg Linda, Model IV3/H/L)

The stability of the beam needs some time, normally about 10-20 min. After that, adjusting the gun and focusing voltage make the beam spots onto the desired area of the sample. Again both sides of the sample have to be polished. The smooth polishing of both sides was carried out using a low energy gun with the voltage of 1 kV and 400 V, respectively. The detailed working parameters are listed in the following:

High energy ion gun	Low energy ion gun
Chamber vacuum: $< 6.0 \times 10^{-5}$ mbar	Chamber vacuum: $< 5.0 \times 10^{-6}$ mbar
Focused voltage: 3.4-3.9 kV	Cathode bias voltage: 1-1.5 V
Source voltage: 7.0- 8.0 kV	Cathode current: 15-17 mA
Ion current: $\sim 20 \mu\text{A}$	Gun 1 voltage: 250 V
Motor movement: rotation	Gun 2 voltage: 50-90 V
Thinning way: double sided thinning	Anode voltage: 1 kV and 400 V
Thinning time: depends on the thickness of the samples, normally 2-5h each side	Focused voltage: 600 V and 230 V
The incident angle: 4-5 degree	

3.2 Electron microscopy

The Precision Ion Polishing System (PIPS) was also used for the preparation of a few specimens. The corresponding conditions are listed as follows:

α_{up}	7°	5°	4°	4°	4°	2°
α_{down}	7°	5°	4°	4°	4°	2°
Voltage (kV)	5	5	5	4	3	1.7
Time (min)	35	35	115	20	15	15

α_{up} and α_{down} - the incident angle of the ion gun above and below the sample with respect to the surface of the sample.

The PIPS with a small volume of the chamber easily reaches the final vacuum after putting in or taking out the sample. During the whole process of preparation, the incident angles of the two guns and the gun voltage were decreased step by step at a rather good focus. The sample was thinned and polished on both sides at the same time. The lowest voltage of the gun available is about 1.5 kV.

Comparing the two ion beam thinning units, the PIPS allows better to adjust the incident angle and to control the beam focus, while the Technoorg-Linda apparatus provides a higher quality surface of the sample because of the use of low energy gun. Fig.3.2.7 shows a final sample prepared by the two techniques. The former has a very good surface and the center hole indicates a good focus and alignment of two guns (Fig.3.2.7a). The latter shows a irregular hole and relative rough surface (Fig.3.2.7b).

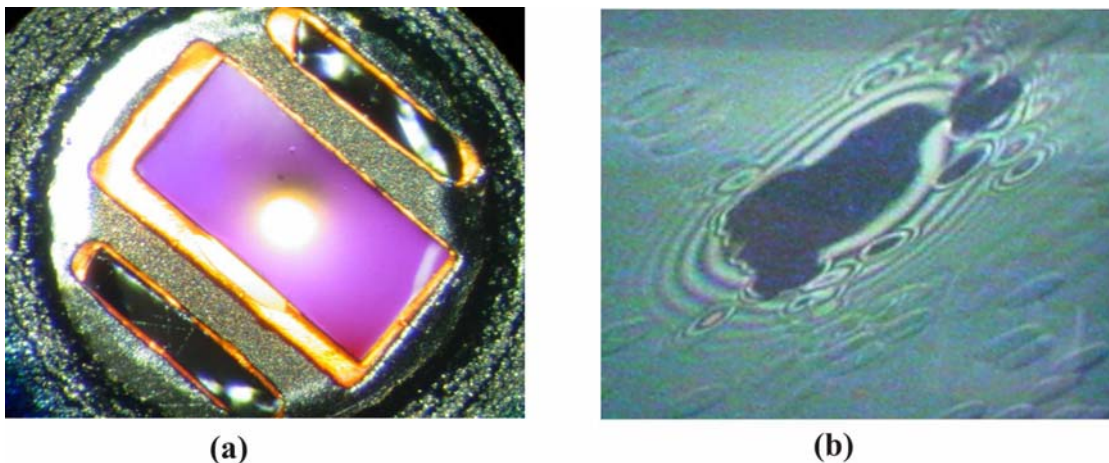


Fig.3.2.7 (a) a sample prepared by Technoorg-Linda apparatus showing the smooth surface; (b) a sample prepared by PIPS showing damaged surface.

3.2.2 Scanning electron microscopy, energy-dispersive X-ray spectrometry and wavelength-dispersive X-ray spectrometry

3.2.2.1 SEM

The principle function of SEM is to produce surface images of three-dimensional objects. The most commonly used types of images are *secondary electron* (SE) images, which show topographic features, and *backscattered electron* (BSE) images, which are used to reveal compositional variations.

Secondary electrons with energies less than 50eV are emitted from the specimen after collision with high energy incident electron beams. The emission of secondary electrons is very sensitive to the angle at which the electron beam strikes the surface. To a large extent, contrast in SE images arises from the variation of the angle between the running direction of secondary electrons emitted from the specimen surface and the detector.

Backscattered electrons are electrons from the incident beam which have interacted with atoms in the specimen and reflected out again. Owing to their relatively high energy comparable to the energy of the primary electrons, backscattered electrons travel in almost straight lines. The amount of the BSE shows a dependence on the angle between primary beam and specimen surface similar to that of the SE, so the apparent brightness of those regions which can be 'seen' by the detector varies with the angle between the surface and detector. The resulting effect gives a good impression of the topography of the specimen. With the usual types of BSE detector which are insensitive to low-energy electrons it is desirable to use an accelerating voltage of 15kV or higher for BSE imaging.

3.2.2.2 EDS and WDS

The energy-dispersive (ED) type consists of a solid-state detector which produces pulses proportional to X-ray photon energy, which are sorted electronically by their amplitude in order to produce a spectrum. The pulses are processed in quick succession and the whole spectrum is effectively recorded in 'parallel'.

In ED spectrometers the X-ray detection medium is a semiconductor crystal (usually silicon doped with Lithium which provides the formation of electron-hole pairs) with an electronic band structure in which the valence band is normally fully

occupied by electrons. When an X-ray photon is absorbed it generates Auger and photo-electrons, which dissipate their energy partly by raising valence electrons to the conduction band. The arrival of each photon thus creates a brief pulse of current caused by electrons and holes moving in opposite directions under the influence of the bias voltage of the detector. The X-ray collection efficiency of an ED spectrometer can be maximized by placing the detector as close as possible to the source. The efficiency of detection of the X-rays reaching the detector is close to 100% over the energy range of 2 ~ 20keV.

The wavelength-dispersive (WD) type makes use of Bragg reflection by a crystal. X-rays are scattered by the atoms in the crystal similar to that of the electron. The result causes the strong reflections where the Bragg equation is satisfied. The most intense reflections (the first order $n = 1$) is normally used in WD analysis. The wavelength range (for $n = 1$) is limited for a given value of d . Several detecting crystals of different spacing are therefore needed to cover an appropriate range of wavelengths. The crystals normally used are LiF ($d = 2.013\text{\AA}$), PET (4.371\AA) and TAP (12.95\AA). WD spectrometers operate in 'serial' mode and are turned to only one wavelength at a time.

The comparison of ED and WD spectrometry is summarized in Table 3.2.1.

Table 3.2.1 Comparison of ED and WD spectrometry.

	ED	WD
Spectrum resolution	Low (110-140eV)	High (ca. 10eV)
Signal-to-noise ratio	Low (ca. 100)	High (ca. 1000)
Count rate/specimen current	High/ca. 10^{-10} A	Low/ca. 10^{-7} A
Detection method	All elements at the same time	One by one
Spectrum record	simultaneous	Sequential
Analysis time	Short	Long
Element range	${}^5\text{B}$ - ${}_{92}\text{U}$	${}^4\text{Be}$ - ${}_{92}\text{U}$
Accuracy	2-10%	1-2%

3.2.2.3 Instrumentation further used

A CamScan 4 SEM equipped with a Thermo Noran detector was used for EDS mapping and compositional analysis. Thin sections of as-grown crystals were cut and polished for SEM measurements. The images using backscattered electrons or secondary electrons were taken at 15kV accelerating voltage, respectively.

3 Experimental methods

A SX100 electron probe micro analyzer produced by CAMECA was used for high precision quantitative analysis for some as-grown crystals. The back scatter images and composition of the sample were measured using at 20kV accelerating voltage and 40.2nA beam current. The size of each measured spot was about 10 μm in diameter.

3.3 Electron spin resonance

Electron Spin Resonance (ESR), also referred to as Electron Paramagnetic Resonance (EPR), is concerned with the energy differences between allowed spin states of an electron spin. An electron has a spin $S = \frac{1}{2}$ and an associated magnetic moment. In a magnetic field \mathbf{B} two spin states $S = +\frac{1}{2}$ and $S = -\frac{1}{2}$ occur with different energies (Fig.3.3.1).

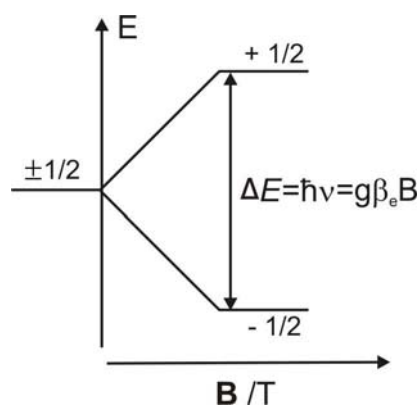


Fig.3.3.1 Energy levels of a spin $S = \frac{1}{2}$ in a magnetic field \mathbf{B} . g is g -factor. β_e is the Bohr magneton.

The energy difference for an electron spin, S , is in the microwave region and, hence, transitions between the two spin states can be induced by applying a microwave radiation to the sample within a magnetic field.

Normally, ESR spectra are obtained by keeping the microwave frequency fixed and varying the magnetic field until the resonance is reached. At resonance, the energy difference between the two states is given by

$$\Delta E = \hbar\nu = g\beta_e B_0 \quad (3.36)$$

where β_e is the Bohr magneton (magnetic moment of a free electron), \mathbf{B} is the applied magnetic field, ν is the frequency and g is the so-called g -factor^[45].

For an isolated free electron $g = 2.0023$. The g -factor is strictly a tensor and its effective value may vary depending on the symmetry of the paramagnetic centre. In single crystal studies the symmetry may be determined by observing the variation of ESR transitions with changing orientation of the crystal relative to the magnetic field \mathbf{B} .

ESR is very sensitive in detecting low spin concentrations, and the detection limit can be as low as 10^{11} spins. Sensitivity is improved by keeping the sample at low temperature (e. g. liquid helium temperature, 4.2K), which increases the population difference between two energy states.

The description above refers to a single electron with two spin states $+1/2$ and $-1/2$. However, transition metal ions and rare earth ions have more than one unpaired electron i.e. $S = n/2$ where n is the number of unpaired electrons and $2S + 1$ spin energy levels occur in a magnetic field. Transitions within these $2S + 1$ levels are governed by the selection rule $\Delta S = \pm 1$, which results in a spectrum with $2S$ lines, referred to as the fine structure in ESR.

In a spherically symmetric electric field, all of these $2S + 1$ energy levels are degenerate and the application of an external magnetic field \mathbf{B} , splits the levels equally, so only one line will be seen in the ESR spectrum. However, in a crystal the electric field is generally distorted depending on the coordination of the paramagnetic ion and, therefore, the effect of the unpaired electrons on each other depends on the symmetry of the ligand field which produces a so called zero field splitting of the energy levels. Hence, resonance does not occur at the same value of the applied field \mathbf{B} but at different values of \mathbf{B} . Therefore, more than one line will be seen in the ESR spectrum.

ESR spectroscopy is a very sensitive tool for detecting paramagnetic centres in small concentration. The spectrum can provide information about the local structural and electronic environment of the paramagnetic centre e.g. Cr^{3+} , Co^{2+} etc. This can be applied to a wide variety of problems either in directly studying the local structure or in using the paramagnetic centre as a probe to monitor processes and reaction in minerals. In addition, ESR technique may be used to determine the site occupied by elements with unpaired electrons, the oxidation state of an element, change in local structure etc.

3.4 X-ray diffraction

X-rays are high frequency ($\sim 10^{18}$ Hz) electromagnetic waves. The oscillating electric field of X-rays interacts with the electrons of an atom, causing them to oscillate with the same frequency. In general, heavy atoms scatter more strongly electrons than light atoms. This proportionality would only be a simple one if the size of atoms is small relative to the X-ray wavelength. However, heavy atoms have dimensions of the same order as the X-ray wavelength. The effect of this is that X-rays scattered from different points in the electron cloud of the same atom interfere with one another resulting in a fall-off in the scattered intensity with the angle through which the incident beam has been scattered. At small scattering angles the scattering is proportional to the atomic number.

When X-rays pass through a crystal the diffraction wave conform to the Bragg equation, that is, the diffractions from a row of lattice points occur at distinct angles and interfere each other when their path differences are integral number of wavelengths. Figure 3.4.1 shows the diffraction geometry. An incident beam is diffracted from two successive (hkl) planes with interplanar spacing d_{hkl} . The path difference for beams from successive planes is given by $AB + BC = 2d_{hkl} \sin\theta$ and, hence, the condition for diffraction maxima is

$$2d_{hkl} \sin\theta = n\lambda \quad (3.4.1).$$

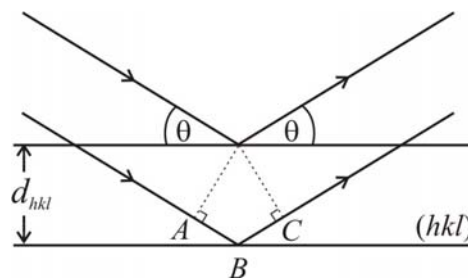


Fig.3.4.1 The condition for Bragg reflection from planes (hkl) with spacing d_{hkl} . The path difference between X-rays reflected from successive planes is $AB + BC$.

The most common application of the Bragg equation is in the interpretation of X-ray diffraction pattern from powders. X-ray powder diffraction is a standard method for identifying crystalline materials, determining their lattice parameters, and in some cases determining crystal structures from the diffracted intensities.

A Siemens DIFFRAC-500 diffractometer with a Cu-K α radiation ($\lambda = 0.15406\text{nm}$, Ni filter, sample pressed onto glass plates) and a Philips X'Pert MRD (θ - θ geometry, samples on Si single crystal sample holder, secondary monochromator, point detector) with CuK α radiation (Si as an external standard) was used for phase identification. The scanning range of $10^\circ \leq 2\theta \leq 80^\circ$ is used with the scanning steps of 0.03° . The measured results are compared with the corresponding data from inorganic crystal structure data (ICSD) using PowderCell program.

An imaging plate diffraction system (STOE IPDS-II) using graphite-monochromatized Mo K α radiation was used for collecting single crystal data. An Oxford cryosystem device which can be cooled down to 100K was used for investigations of the phase transition.

3.5 Magnetic measurements

Magnetic moments associated with atoms in magnetic materials have three origins: These are the electron spins, the electron orbital motion and the change in orbital motion of the electrons caused by an applied magnetic field \mathbf{H} .

The diamagnets are solids with no permanent net magnetic moment per atom. Diamagnetic susceptibility χ arises from the realignment of electron orbital under the action of a magnetic field. Therefore all materials exhibit a diamagnetic susceptibility, although not all are classified as diamagnets. Some materials have a net magnetic moment per atom, due to an unpaired electron spin in each atom which leads to paramagnetism or even to ordered magnetic states such as ferromagnetism and antiferromagnetism. In each case the paramagnetic or ferromagnetic susceptibility is much greater than the diamagnetic susceptibility and therefore is the dominant effect. Paramagnetism occurs at higher temperatures in all materials which have a net magnetic moment. The atomic magnetic moments are randomly oriented but can be aligned by a magnetic field.

Only the change in orbital motion gives rise to a diamagnetic susceptibility. Diamagnetism leads to a very weak magnetization which opposes the applied magnetic field. The diamagnetic susceptibility is therefore negative and has an order of magnitude of $-\chi \approx 10^{-5}$ or 10^{-6} . It is also found to be independent of temperature.

Both the electron spin and the orbital angular momentum contribute to the magnetization which leads to positive susceptibility. The susceptibilities of paramagnets are typically of the order of $\chi \approx 10^{-3}$ to 10^{-5} , and at low fields \mathbf{H} the magnetization \mathbf{M} is proportional to \mathbf{H} . The susceptibilities of a large number of paramagnetic solids were measured over a wide temperature range. It is found that the susceptibility varies inversely with temperature,

$$\chi = \frac{C}{T} \quad (3.5.1)$$

where C is the Curie constant. The materials obeying this law are materials in which the magnetic moments are localized at the atomic sites, i.e. the magnetic atoms are surrounded by a number of non-magnetic atoms. But it was also found that for the description of χ (T) a more generalized form is necessary known as the Curie-Weiss law:

$$\chi = \frac{C}{(T - \theta_p)} \quad (3.5.2)$$

where θ_p is the paramagnetic Curie temperature. θ_p can be either positive, negative or zero. For materials that undergo a paramagnetic to ferromagnetic transition $\theta_p > 0$ corresponds to the Curie temperature T_C . For materials that undergo a paramagnetic to antiferromagnetic transition the term θ_p is less than zero ($\theta_p < 0$), although in practice the transition temperature between the paramagnetic and antiferromagnetic phases occurs at a positive temperature T_N known as the Neel temperature. It should be remembered that the susceptibility only follows the Curie-Weiss law in the paramagnetic region. As soon as the material becomes ordered the susceptibility behaves in a very complicated way and no longer has a unique value for a given field strength.

There are a number of different types of magnetic order in solids including ferromagnetism, antiferromagnetism, weak ferromagnetism ferrimagnetism and helimagnetism. Rare earth compounds, for example, exhibit more than one ordered magnetic state. These ordered states undergo transitions at critical temperatures so that every solid that exhibits one of these types of magnetic order will become paramagnetic at higher temperatures. For example in a ferromagnet, e.g. Fe, Co, Ni with strong exchange interactions between the magnetic dipoles, the Curie point is the transition temperature above which the material becomes paramagnetic and below which an ordered ferromagnetic state exists. The Neel point is the temperature below which an ordered antiferromagnetic state exists. Some solids such as terbium, dysprosium and holmium have both Curie and Neel temperatures. Fig.3.5.1 shows some possible types of magnetic ordering of solids.

In oxides a different kind of exchange interaction occurs via the oxygen atoms, and the spins of neighbouring metal ions become aligned in an antiparallel way. This coupling mechanism, e.g. Fe (\uparrow) – O – Fe (\downarrow), is termed as superexchange interactions, and becomes most effective as the Fe – O – Fe bond angle approaches 180° . If the moments are exactly antiparallel, there is no net magnetic moment. In some cases the spin directions are not precisely antiparallel and a small net magnetic moment results from this spin canting.

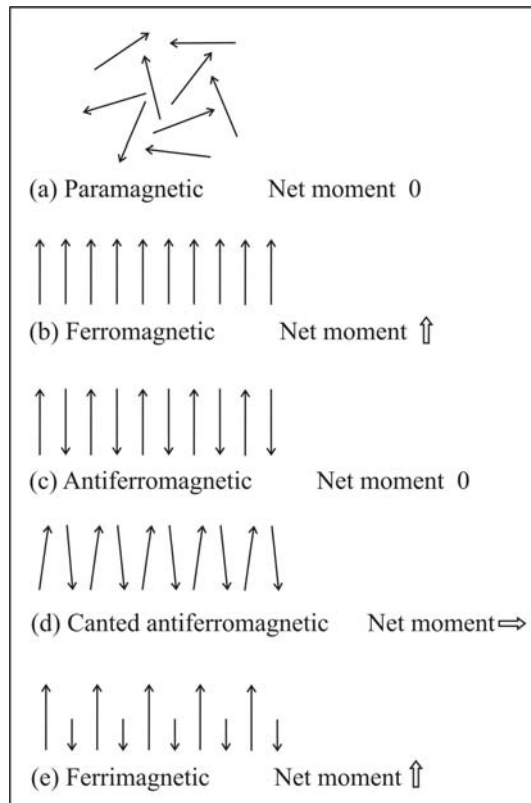


Fig.3.5.1 Different types of magnetic ordering

Hematite (Fe_2O_3) is a famous example for a canted antiferromagnet with a Curie temperature of 680°C . Silicate minerals containing paramagnetic ions only become magnetically ordered at low temperatures and therefore they do not play a role in the magnetism of rocks. But none the less a lot of silicates can stand for model substances.

The Quantum Design **M**agnetic **P**roperties **M**easurement **S**ystem (MPMS-2) is a SQUID-magnetometer allowing highly automated measurements of the magnetic moment of a wide variety of samples as a function of magnetic field, temperature or time. Magnetic moments down to 10^{-7}emu (10^{-7}Gcm^3) can be measured in a reproducible way. The MPMS has a temperature range between 1.8K and 400K, the superconducting magnet can reach magnetic fields between -5.5Tesla and +5.5Tesla.

Specimens must be fixed rigidly inside a tube which is magnetically homogeneous and of low magnetic susceptibility. For experiments in the temperature range 2K-330K, we use transparent drinking straws.

The background signal contributed by the mount can be recorded separately and subtracted from the data. Fields are applied parallel to the specimen tube, and the magnetisation of the specimen is measured along the same direction.

3.6 Other methods

Besides the techniques outlined in some detail above the following experimental techniques have also been used to characterize and investigate the samples.

3.6.1 Differential scanning calorimeter

A Mettler Toledo DSC 821^e was used for the investigation of the anomaly of heat capacity in the selected system under nitrogen atmosphere. The sample was placed in a standard aluminum pan. The sample amount was 7mg. The cycle of heating and cooling at a rate of 5K /min was carried out twice. The second heating curve was used to calculate the phase transition temperature. Temperature and enthalpy were calibrated with ultra-pure zinc- and indium-sample.

3.6.2 Photoluminescence measurements

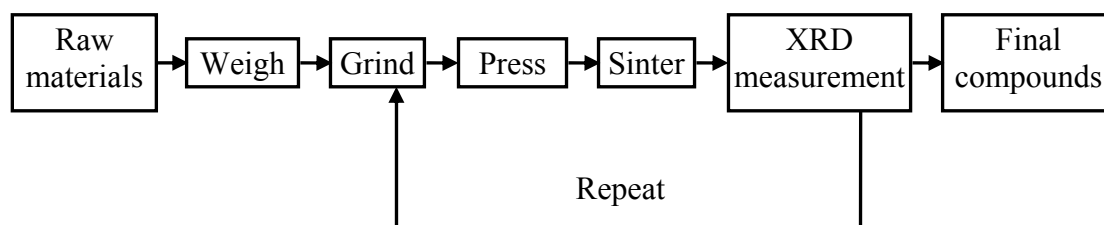
A Perkin-Elmer Lambda 9 with a spectral resolution of about 2nm was used for the measurements of the excitation and emission spectra. The setup was equipped with a Xe lamp of 1000W as heat source and two monochromators (spectropro 300I, Acton Research, Polytec) controlled by a NCL single-channel spectroscopy detection system.

A Shimadzu RF-1502 spectrofluorometer (light source = XBO lamp) with a resolution of about 15nm was also used. The light power at the excitation wavelength was in the range below 1mW.

4 Results and discussions

4.1 Synthesis of $\text{Ca}_2\text{MgSi}_2\text{O}_7$, $\text{Ca}_2\text{CoSi}_2\text{O}_7$ and $\text{Ca}_2\text{ZnSi}_2\text{O}_7$ melilites

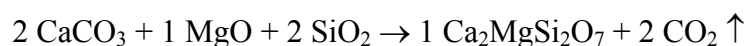
Powder of high purity of CaCO_3 (99.97%, Merck), of MgO (99.999%, Ventron GMBH), of Co_3O_4 (99.7%, Merck), of ZnO (99.999%, Merck) and of SiO_2 (99.995%, Merck) were weighed in stoichiometric proportions. MgO was first heated at 1000°C for 5h to remove absorbing water. The stoichiometric mixture was then ground in an agate mortar, pressed into pellets and calcined in a program-controlled oven. The calcined powder was mixed again and sintered until the pure intended compound was obtained. The whole preparation procedure is given in scheme 4.1.1.



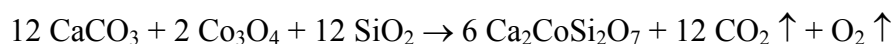
Scheme 4.1.1 The procedure of preparing powder material.

The reaction equations for the three compounds are given as follows:

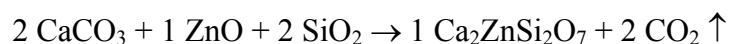
CaMg-åkermanite



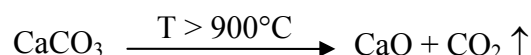
CaCo-åkermanite



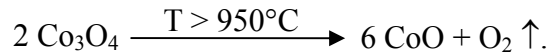
CaZn-åkermanite



The reaction process involves the decomposition of CaCO_3 when the temperature is higher than about 900°C ^[46] according to:



For the CaCo-åkermanite synthesis, it also involves the decomposition of Co_3O_4 into CoO and O_2 according to:



Taking into account the decomposition of CaCO_3 and Co_3O_4 , the sintering program of four steps was taken (Table 4.1.1). Step 1 was to preheat the oven and step 2 for decomposition. The raw materials reaction to form the expected product was performed in step 3, which should use a low heat rate. Step 4 was to drop temperature.

Table 4.1.1 Sintering program for three melilite systems.

Steps	Heat rate (°C/h)	Final Temp. (°C)	Dwell time (h)	Notes
1	800	200	0	System requirement
2	200	1000	2	In order to decompose CaCO_3 and Co_3O_4
3	75	1350/1200/1300	48	$\text{CaMg-} / \text{CaCo-} / \text{CaZn-}\text{\AA} \text{kermanite}$
4	-150	50	0	Temperature drop

After the first sintering, XRD results of the end-member of $\text{Ca}_2\text{MgSi}_2\text{O}_7$ show that the main phase is $\text{Ca}_2\text{MgSi}_2\text{O}_7$. Some additional peaks correspond to $\text{Ca}_3\text{MgSi}_2\text{O}_8$ and $\text{CaMgSi}_2\text{O}_6$. The pure phase of $\text{Ca}_2\text{MgSi}_2\text{O}_7$ could be achieved after a third sintering process (Fig.4.1.1).

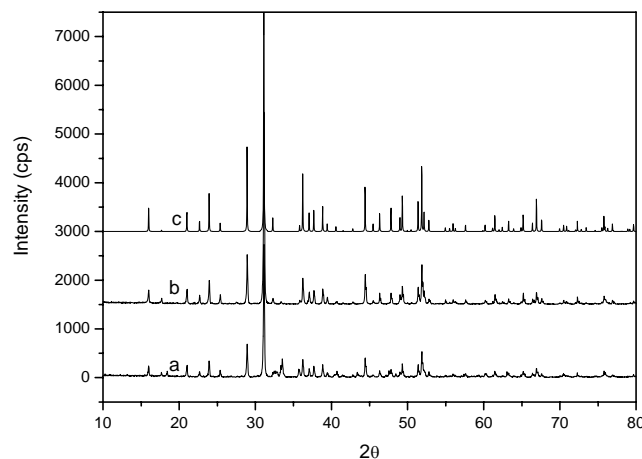


Fig.4.1.1 XRD diagrams of $\text{Ca}_2\text{MgSi}_2\text{O}_7$. a) after first sintering run; b) after third sintering run; c) data from ICSD-100736.

For the end-member $\text{Ca}_2\text{CoSi}_2\text{O}_7$ a longer reaction time was needed to obtain the pure phase. The possible reason is due to the use of Co_3O_4 . In the intended product Co

4.1 Synthesis of $\text{Ca}_2\text{MgSi}_2\text{O}_7$, $\text{Ca}_2\text{CoSi}_2\text{O}_7$ and $\text{Ca}_2\text{ZnSi}_2\text{O}_7$ melilites

exists in the valence state 2+. Although Co_3O_4 starts to decompose at about 950°C , the complete decomposition process is rather slow, which is confirmed by the color change of the sample from grey-black to deep blue. After repeating the sintering five times the pure phase was obtained as identified by XRD in Fig.4.1.2.

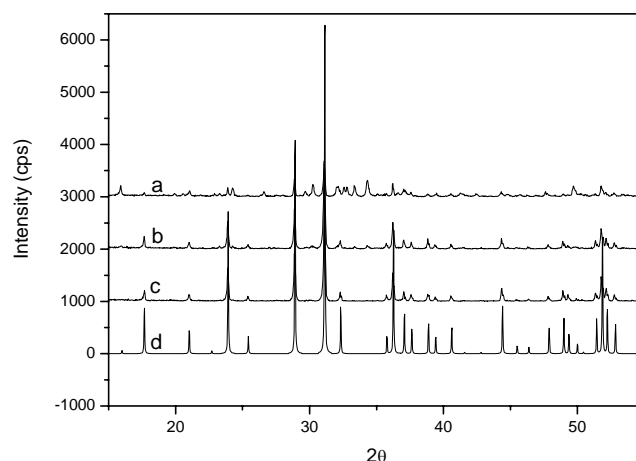


Fig.4.1.2 XRD diagram of $\text{Ca}_2\text{CoSi}_2\text{O}_7$. a), b) and c) corresponding to first, third and five sintering runs, respectively; d) data from ICSD-72543.

For the end-member $\text{Ca}_2\text{ZnSi}_2\text{O}_7$ the experiments showed that it is very difficult to get the pure phase comparing to the former two. The stoichiometric raw materials were calcined three times, however, four additional peaks were always observed in the XRD diagrams. Refinement of the measurements using PowderCell program^[47] showed that these additional peaks belong to $\text{Ca}_3\text{Si}_3\text{O}_9$ -26553 from inorganic crystal structure database (ICSD), which are obviously formed because of the evaporation of ZnO during the high-temperature reaction process. The refinement results showed that approximate 88% $\text{Ca}_2\text{ZnSi}_2\text{O}_7$ and 12% $\text{Ca}_3\text{Si}_3\text{O}_9$ were obtained. Therefore, 5/4 of stoichiometric ZnO was added to the mixture and sintered again. The XRD results then showed a good agreement with the single-crystal data of $\text{Ca}_2\text{ZnSi}_2\text{O}_7$ -18114 (Fig.4.1.3).

4 Results and discussions

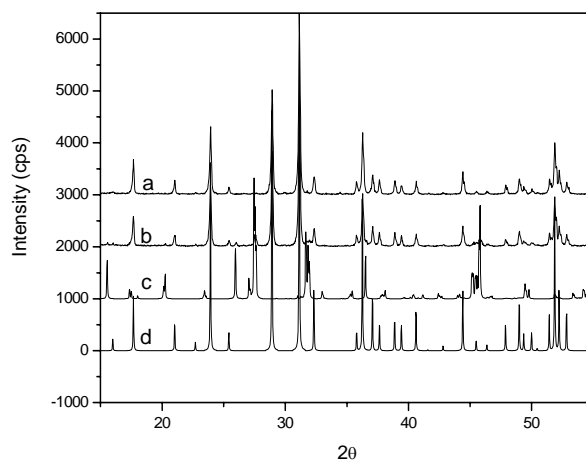


Fig.4.1.3 XRD diagram of $\text{Ca}_2\text{ZnSi}_2\text{O}_7$ powder. a) after fourth sintering (additional ZnO); b) after third sintering; c) and d) the data of $\text{Ca}_3\text{Si}_3\text{O}_9$ and $\text{Ca}_2\text{ZnSi}_2\text{O}_7$ from ICSD, respectively.

4.2 Single crystal growth

For the growth of melilite crystal two main methods, the Czochralski (CZ) ^[48] and the Floating Zone (FZ) melting ^[49] method, were reported. In the present work, all single crystals were grown by the FZ melting method.

In this section, the preparations for single crystal growth, the growth parameters, and the particular growth procedure for each system were described. The growing steps responsible for the final crystal quality were outlined.

4.2.1 The preparation of a feed rod and a seed crystal

The preparation of the feed rod is crucial for a successful growth process. After powder synthesis of the end-member compounds, melilites with different composition were obtained by proportionally mixing two end-members. The mixtures then were prepared into rods with certain diameter and length.

Normally, there are two ways to prepare a rod. One is that the powder is intimately mixed together with acetone in a polyethylene blender, placed into a sealed rubber tube to form a rod, and then hydrostatically pressed. Finally, the rod is calcined at a certain temperature.

Another way is to place the powder into an alumina tube where it is calcined, subsequently. We used the latter way to prepare rods of 4 mm diameter and 40-60 mm length. A small quantity of the powder was given into the alumina tube and immediately compressed by hand using a quartz stick. Then the next powder load was added and compressed and so on. If too much powder was added at once, the rod can break easily. The procedure is illustrated in Fig.4.2.1.

For the series $\text{Ca}_2\text{MgSi}_2\text{O}_7\text{-Ca}_2\text{ZnSi}_2\text{O}_7$, excess of 1% ZnO related to the amount of the $\text{Ca}_2\text{ZnSi}_2\text{O}_7$ as well as a small amount of $\text{Ca}_2\text{CoSi}_2\text{O}_7$ was added into the rod. The ZnO excess compensates the loss of evaporation during sintering and growing, while $\text{Ca}_2\text{CoSi}_2\text{O}_7$ increases the absorption of radiative energy by changing the rod color from white to light blue. The experiments proved that the $\text{Ca}_2\text{CoSi}_2\text{O}_7$ excess decreased the input energy efficiently. The temperature for sintering was the same as that of synthetic powder.

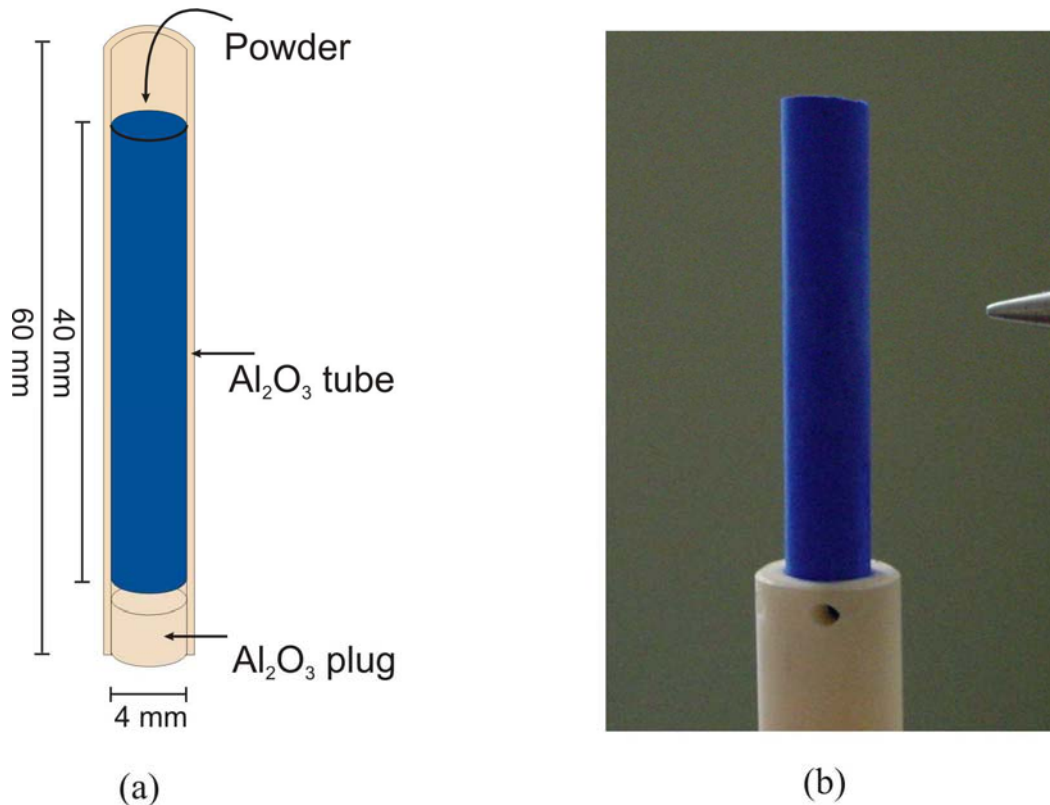


Fig.4.2.1 (a) The preparation of a rod in an Al_2O_3 tube; (b) the centered rod of $\text{Ca}_2\text{Co}_{0.7}\text{Zn}_{0.3}\text{Si}_2\text{O}_7$ used for crystal growth.

A seed crystal is necessary to grow single crystals. There are three advantages for using a seed crystal:

- Crystals with a certain orientation can be grown by a pre-oriented seed crystal;
- Nucleation happens only on boundaries of a seed crystal;
- A stable growth interface can be reached easily.

To grow a seed crystal the following steps were performed:

- 1) The sintered rod, fixed into a ceramic tube located in the upper shaft of the pulling unit, was used as nutrient. A Pt wire of 0.5mm diameter was mounted into a ceramic rod of the lower shaft.
- 2) The rod and the Pt tip were centered along the rotating axis and counter-rotated with a certain speed to ensure a flat interface and homogeneity.
- 3) The nutrient rod was moved into the focus area of the lamps and the input power was increased step by step until the rod starts to melt.
- 4) When the material in the zone was melted homogeneously, the Pt tip was moved upwards until the hanging melting drop was touched.

- 5) After the equilibrium was achieved, the Pt tip was pulled down carefully until the solid-liquid interface could be observed.
- 6) The growing speed and the traveling-down speed of the feed rod could be set at this time.
- 7) At the end of the growth procedure, the temperature was lowered slowly to reduce the volume of the melting zone. Finally the as-grown crystal was separated from the melt.

Because the as-grown crystal using a Pt tip is arbitrarily oriented a orientation of the crystal has to be carried out, before a parallelepiped of $2 \times 2 \times 5\text{mm}^3$ size for the use as seed crystal can be prepared.

4.2.2 Growth of $\text{Ca}_2\text{Mg}_{1-x}\text{Zn}_x\text{Si}_2\text{O}_7$, $\text{Ca}_2\text{Co}_{1-x}\text{Zn}_x\text{Si}_2\text{O}_7$, $(\text{Ca}_{1-x}\text{Sr}_x)_2\text{CoSi}_2\text{O}_7$ crystals

Generally, the growth of a high-quality crystal requires maintaining the growth conditions as stable as possible. Fig.4.2.2 shows the four stages of the growth process. The initial amount of the melt has a strong influence on the subsequent formation of the solid-liquid interface and its position. Too much melt moves the solid-liquid interface downwards even under the same input voltage. The increase of the melt volume is especially disadvantageous for crystal growth when evaporating material like ZnO is present. In addition, if the melting point of the seed crystal is a little bit higher than that of the rod (for example, the seed crystal of $\text{Ca}_2\text{Co}_{0.7}\text{Zn}_{0.3}\text{Si}_2\text{O}_7$ was used for growing the $\text{Ca}_2\text{Co}_{0.9}\text{Zn}_{0.1}\text{Si}_2\text{O}_7$ crystal), the seed crystal will be covered by the melt and finally melted completely due to the heat capacity and conductivity if there is an excess of the melt.

To obtain a suitable volume of the melt, one should first try to get a rough value of the input voltage under which the rod can be melted. Then the input voltage must be adjusted carefully. This step takes some time because the effect of the input voltage on the rod can be detected after a certain time. Three different situations of the melt are shown in Fig.4.2.3.

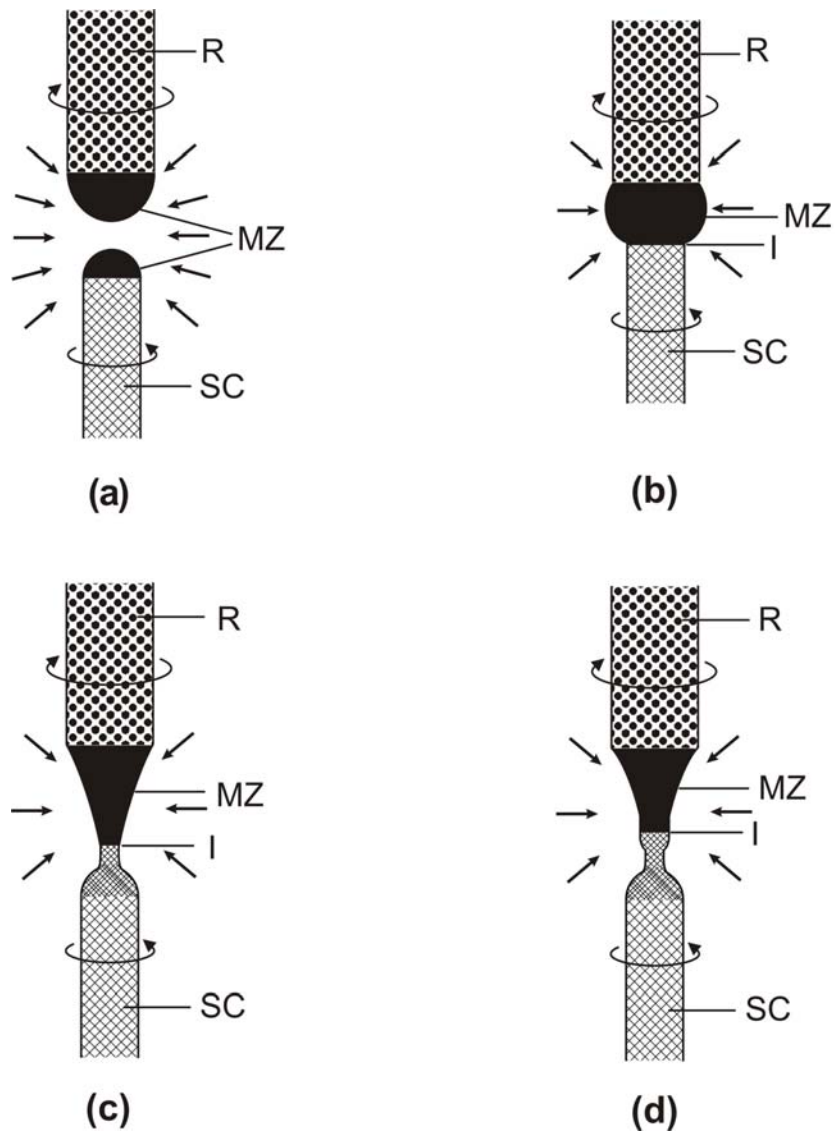


Fig.4.2.2 The four stages of the FZ growing process. R – Rod; MZ – Melting zone; I – Solid-liquid interface; SC – Seed crystal. a) the melting rod (R) and the seed crystal (SC); b) contact between rod and seed crystal; c) crystal growth at the beginning with smaller diameter; d) crystal growth under fixed conditions.

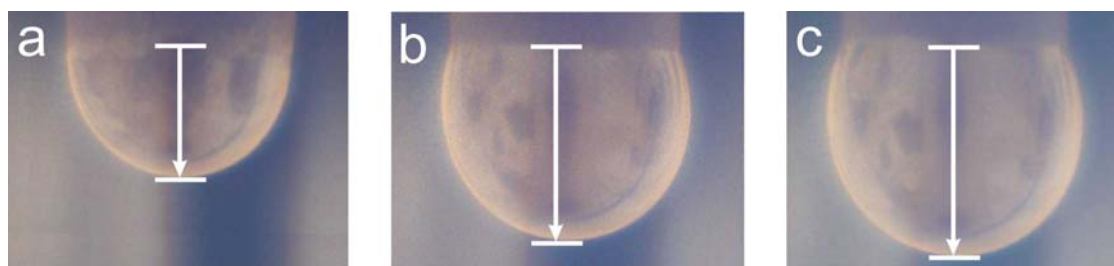


Fig.4.2.3 Three possible melting shapes of the melt drop. The volume of the melt is indicated roughly by the white arrow. a) too less; b) just right; c) too much.

4.2 Single crystal growth

The suitable volume of the melt should be just a little bit larger than a half sphere whose radius is the same as that of the rod. Because the major force holding a floating zone in place is the surface tension, it is possible to obtain the quantitative expression by neglecting the cohesion between the solid and liquid and buoyancy. The growth angle is often used for the description of the melt shape (or volume), which is defined as the angle α between the meniscus surface and the growth direction of the crystal at the solid-liquid-gas trijunction (Fig.4.2.4). More information can be referred to the corresponding literatures ^[50].

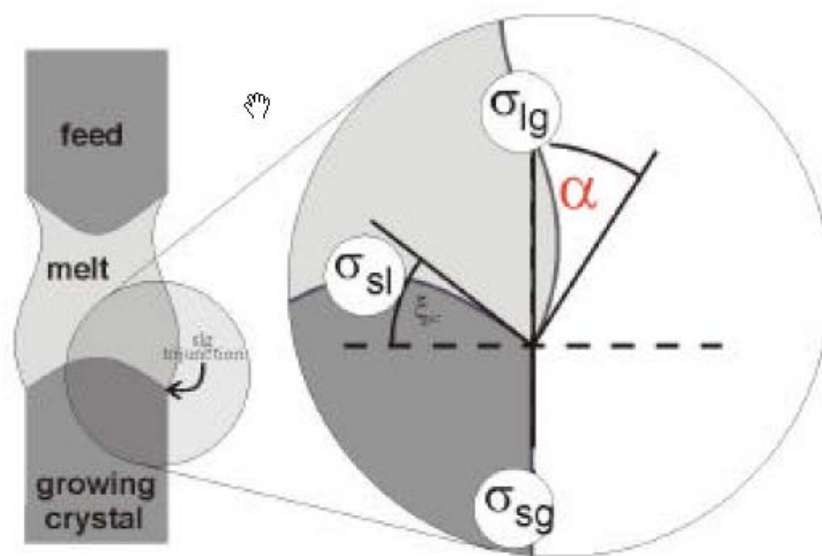


Fig.4.2.4 Growth angle α . Important parameters controlling the floating zone process: σ_{lg} , σ_{sb} , and σ_{sg} are the interface free energies liquid-gas, solid-liquid and solid-gas, respectively.

Once the melt was homogeneous, the seed crystal was moved upwards until it touched the melt. To get the solid-liquid interface, one may drag the seed crystal downwards, and meanwhile, sometimes adjust the input voltage. In fact, careful control of the melt volume as well as of the temperature gradient is important to attain a stable solid-liquid interface. Fortunately, the situation of the interface can be observed directly on the monitor by means of a CCD camera. In Fig.4.2.5 a good and stable solid-liquid interface is shown.

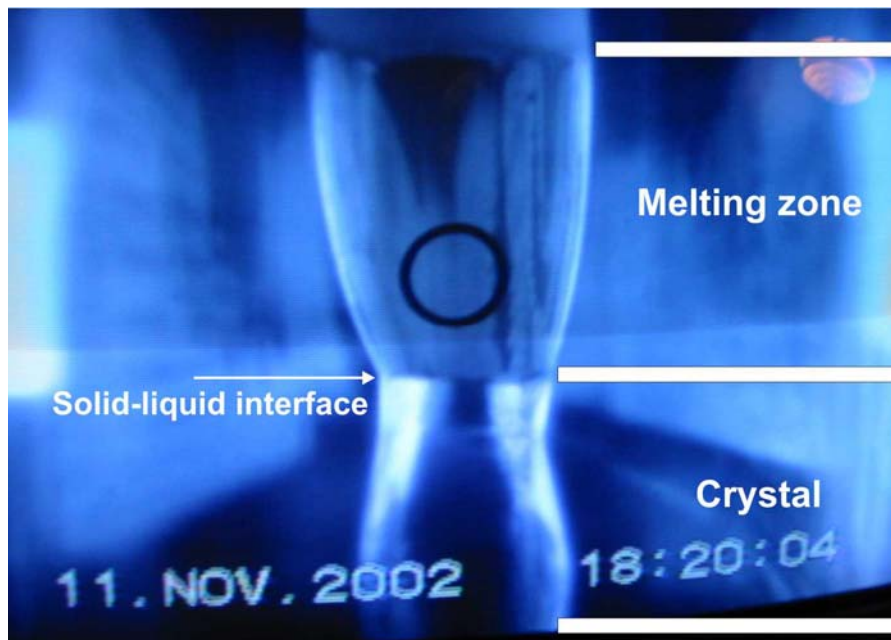


Fig.4.2.5 Picture taken at stable condition during growing crystal process. A stable and plane solid-liquid interface can be seen clearly.

The suitable traveling-down speed (growth speed) can be set up after obtaining the stable solid-liquid interface. For our experiments, a traveling-down speed of 1.0 mm/h of the seed crystal was normally used. However, at the beginning, often a speed of 0.5 mm/h of the rod was used, leading to a smaller diameter of the as-grown crystal which benefits to grow single crystal. Although the seed crystal with certain lattice facets was used, growth of the crystal may occur in different directions at the beginning. Therefore, the diameter of the crystal should be as small as possible to decrease the number of nucleation possibilities. Furthermore, different growth directions would compete with each other until the dominant direction was obtained as described in Fig.4.2.6. After that, the traveling-down speed of the rod can be increased to grow the crystal with a larger diameter. It should be noted that the separation of the crystal from the melt is also an important step. If the cooling procedure is too fast, it will cause the formation of cracks within the grown crystal (see 4.3) which will be discussed in more detail later. Normally we reduced the input voltage by 0.1 V/min.

For the melilite rod, a little gas could be absorbed into the melting zone, as seen from Fig.4.2.7, which would be influential for heat convection and further, for the crystal quality. This effect can be weakened by quenching the melt or by using growing condition with less oxygen pressure.

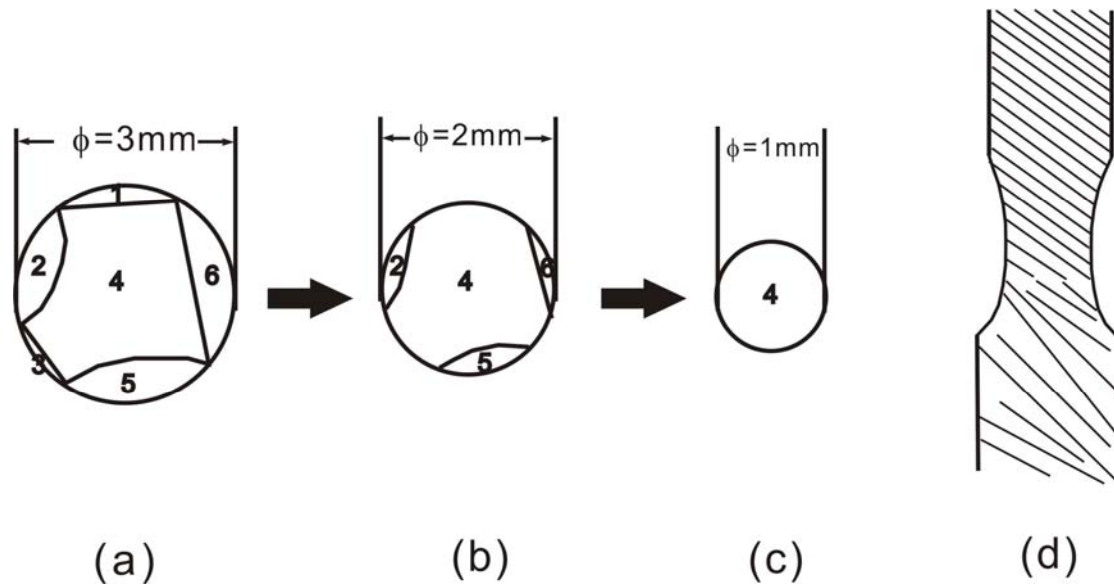


Fig.4.2.6 The crystal growth with different growing direction. (a-c) the evolution from multi- to single-growing direction. d) the crystal shape.

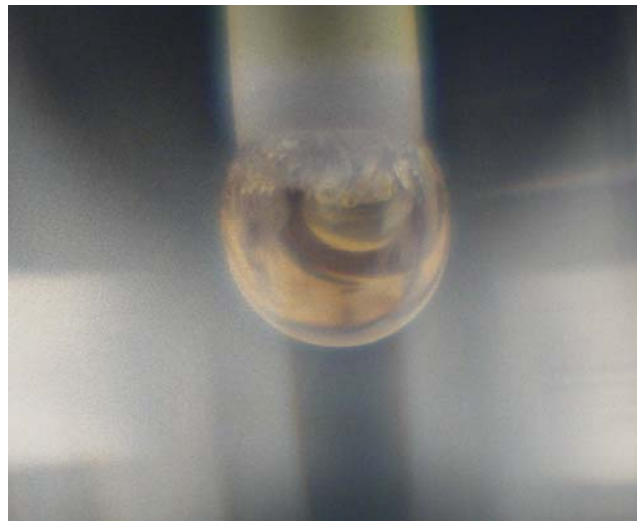


Fig.4.2.7 The melt hanging on the rod. A large bubble inside near the solid-liquid interface can be seen.

In the floating zone melting method, to grow a crystal one can also fix a seed crystal onto the upper shaft and move it upwards. However, such as-grown crystals normally include bubbles, therefore, we have chosen the moving-down technique. On the other hand, when the seed crystal is fixed in the lower shaft oxygen bubbles are introduced if the growing speed is too high, for example, bubbles were observed in a cross-section of a crystal grown at the speed of 1.5 mm/h (Fig.4.2.8).

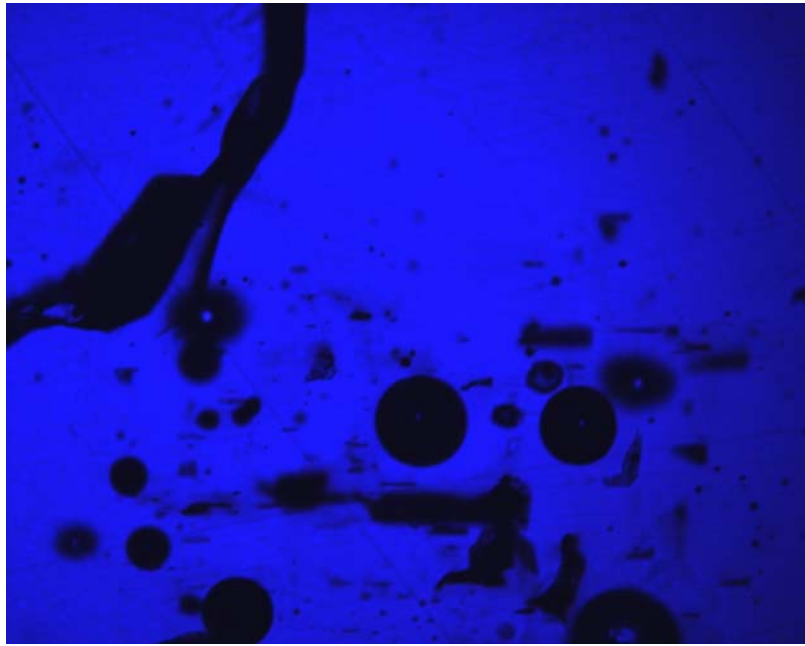


Fig.4.2.8 Cross section of as-grown crystal at the speed of 1.5 mm/h. Dark circle dot representing bubbles.

Generally, each system required special growth conditions as described in the following subparts.

$\text{Ca}_2\text{Mg}_{1-x}\text{Zn}_x\text{Si}_2\text{O}_7$

The feed rods of $\text{Ca}_2\text{Mg}_{1-x}\text{Zn}_x\text{Si}_2\text{O}_7$ have white color. A white rod reflects the radiative energy coming from halogen lamp more than a colored rod. Therefore, the input power had to be increased to melt the rod, which may result in an overheating of the rod. Further, ZnO easily evaporates at higher temperatures, therefore, overheating must be avoided as much as possible. To solve this problem, 0.1 wt % $\text{Ca}_2\text{CoSi}_2\text{O}_7$ of deep blue color was added to the series $\text{Ca}_2\text{Mg}_{1-x}\text{Zn}_x\text{Si}_2\text{O}_7$. The acquired rods are light blue and were sintered at 1350°C for 6h. The detailed conditions for growth are listed in Table 4.2.1.

There was another problem during the growing process. The contamination of the internal wall of the quartz tube by evaporating ZnO caused the loss of radiative energy, and furthermore, the instability of the solid-liquid interface. Under this growth condition some cracks in the final crystal were observed. To solve this problem, one

4.2 Single crystal growth

had to use a small melt volume, which will be described in 4.4. Prolonging the growing time, the loss of radiative energy was quite serious, so one had to keep the temperature of the melting zone stable by increasing the input voltage or moving the quartz tube. In the latter case, we could not grow long crystals because of the limitation of the length of the quartz tube.

Table 4.2.1 Data of rods and as-grown crystals for the $\text{Ca}_2\text{Mg}_{1-x}\text{Zn}_x\text{Si}_2\text{O}_7$ system.

x value	Rods			Crystals			
	Length	Diameter	Melting voltage	Growth voltage	Upper speed	Lower speed	Crystal length
	(mm)	(mm)	(V)	(V)	(mm/h)	(mm/h)	(mm)
0.0	37	4.7	87	73.3-73.5	0.5-1.0	1.0	23
0.1	36	4.8	87	73.6-73.9	0.5/1.2	1.0	9
0.3	34	4.6	88	73.4-74.2	0.5-1.2	1.0	10
0.5	32	4.6	77	73.8-74.9	0.5/1.0	1.0	11
0.7	31	4.6	77	69.0-70.4	0.7	1.0	10
0.9	30	4.6	75	72.2	0.5	1.0	7
1.0	32	4.6	62	66.7-67.0	0.7	1.0	14

$\text{Ca}_2\text{Co}_{1-x}\text{Zn}_x\text{Si}_2\text{O}_7$

All rods of $\text{Ca}_2\text{Co}_{1-x}\text{Zn}_x\text{Si}_2\text{O}_7$ solid solutions are blue, thus absorbing the radiative energy very well. Comparing to the rod of $\text{Ca}_2\text{Mg}_{1-x}\text{Zn}_x\text{Si}_2\text{O}_7$, the $\text{Ca}_2\text{Co}_{1-x}\text{Zn}_x\text{Si}_2\text{O}_7$ rod could be melted at a relatively low input voltage. The voltage to melt the rod was nearly the same as that to keep a stable growth. The preparing method for rods was the same as described above. For the solid solutions including Zn an excess of 1 wt % ZnO was added. Because the difference of the melting points between the end-members of $\text{Ca}_2\text{CoSi}_2\text{O}_7$ and $\text{Ca}_2\text{ZnSi}_2\text{O}_7$ is more than 100°C , the temperature for sintering the rod was divided into two levels according to the ratio of Zn in the solid solutions. Table 4.2.2 summarizes the details of the rod as well as the conditions for growing crystals. The as-grown crystals are dark blue except that of the end-member $\text{Ca}_2\text{ZnSi}_2\text{O}_7$ (light blue). The crystals are free of bubbles, however, some cracks could be observed at $x > 0.7$. The number of cracks increased with prolonging the growing time. Evaporation of ZnO still exists during the whole growing process, but is much smaller in comparison to the $\text{Ca}_2\text{Mg}_{1-x}\text{Zn}_x\text{Si}_2\text{O}_7$ system.

4 Results and discussions

Table 4.2.2 Data of rods and as-grown crystals for the $\text{Ca}_2\text{Co}_{1-x}\text{Zn}_x\text{Si}_2\text{O}_7$ system.

x value	Rods				Crystals			
	Length	Diameter	Sintering temp.	Melting voltage	Growth voltage	Upper speed	Lower speed	Crystal length
	(mm)	(mm)	(°C)	(V)	(V)	(mm/h)	(mm/h)	(mm)
0.0	23	4.7	1200	43	45.3	0.5-0.8	1.0	22
0.1	32	4.7	1200	44.5	44.5	0.7	1.0	21
0.3	32	4.7	1200	47	47.2-46.5	0.7	1.0	10
0.5	31	4.7	1250	48	48.5	0.7	1.0	10
0.7	31	4.5	1250	50	50	0.8	1.0	12
0.9	32	4.5	1250	51	50.9-51.2	0.7	1.0	6
1.0	32	4.6	1250	62	66.7-67.0	0.7	1.0	14

$(\text{Ca}_{1-x}\text{Sr}_x)_2\text{CoSi}_2\text{O}_7$

For this system, an unexpected problem was encountered when preparing the rod. Cracks were observed in all sintered rods during the growing process. Such cracks became enlarged with growing time and finally the nutrient material near the melt broke down, resulting in a stop of the experiment (Fig.4.2.9a). Several ways were tried to solve this problem. Increasing the sintering temperature did not show evident effects. Fixing the seed crystal onto the upper part and growing the crystal by moving the seed crystal upwards may avoid the separation the melt from the rod (Fig.4.2.9a), but bubbles occurred in the center of the crystal at the growing speed of 1.0 mm/h. Finally, it was found that prolonging the sintering time up to 10 h combined with a uniform pressing of the rod could avoid the occurrence of cracks during growth (Fig.4.2.9b).

The corresponding details for $(\text{Ca}_{1-x}\text{Sr}_x)_2\text{CoSi}_2\text{O}_7$ solid solutions are depicted in Table 4.2.3. Very stable growing conditions could be reached for this system and single crystals with high quality were grown for all compositions.

4.2 Single crystal growth

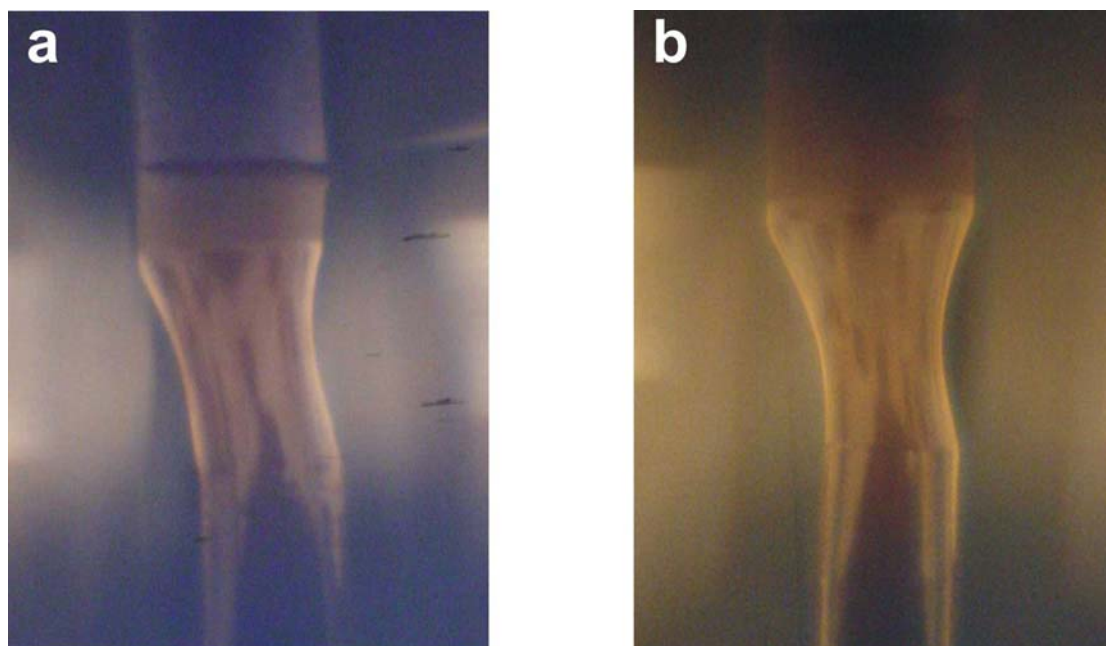


Fig.4.2.9 a) The rod sintering 6 h at 1250°C showing the crack during the growing process; b) there are no cracks in the rod sintering 10 h or more at the same temperature.

Table 4.2.3 Data of rods and as-grown crystals for the $(Ca_{1-x}Sr_x)_2CoSi_2O_7$ system.

x value	Rods			Crystals			
	Length	Diameter	Melting voltage	Growth voltage	Upper speed	Lower speed	Crystal length
	(mm)	(mm)	(V)	(V)	(mm/h)	(mm/h)	(mm)
0.0	23	4.7	43	45.3	0.5-0.8	1.0	22
0.07	18	4.6	40.5	40.6	0.5-0.7	1.0	25
0.1	21	4.7	42	41	0.5-0.65	1.0	21
0.12	30	4.6	45	45.1	0.7-1.0	1.0	10
0.25	20	4.7	42	42	0.6	1.0	24
0.30	25	4.5	42.2	42.2	0.5-0.7	1.0	22
0.35	38	4.7	41.5	42	0.2-0.7	1.0	23
0.50	17	4.8	46.4	48.2	0.5-0.8	0.7	12
0.75	32	4.6	54	54.6	0.8	1.0	7

4.3 Investigations of $\text{Ca}_2\text{Mg}_{1-x}(\text{Zn}, \text{Co})_x\text{Si}_2\text{O}_7$ with modulated structure

This section includes two series melilites. The crystal characterization and the incommensurate-to-normal phase transition were described in $\text{Ca}_2\text{Mg}_{1-x}\text{Zn}_x\text{Si}_2\text{O}_7$. Studies of the structural modulation of $\text{Ca}_2\text{Mg}_{1-x}\text{Co}_x\text{Si}_2\text{O}_7$ by means of TEM were reported. Detailed growth conditions and the corresponding characterization can be found in Pokoj's diploma work ^[51].

4.3.1 The $\text{Ca}_2\text{Mg}_{1-x}\text{Zn}_x\text{Si}_2\text{O}_7$ system

4.3.1.1 Crystal characterization

A series of $\text{Ca}_2\text{Mg}_{1-x}\text{Zn}_x\text{Si}_2\text{O}_7$ single crystals with the nominal values $x = 0, 0.1, 0.3, 0.5, 0.7, 0.9, 1.0$ were grown using the floating zone melting method. Fig.4.3.1 shows two as-grown crystals of different Zn concentration. Usually, at lower Zn concentration crystals of high-quality were obtained. With increasing Zn/(Mg + Zn) ratio, cracks were observed at the surface of the crystals. The number of cracks increased with increasing Zn content and growth time. The main reason for that is the evaporation of Zn at high melting temperatures. The evaporation of Zn causes an unbalance of the composition and instability of the solid-liquid interface, yielding atomic micro-arrangements of atoms inside the interface may occur with different crystallographic orientations. Hence, the amount of Zn was kept as constant as possible during the experiments (see 4.2).

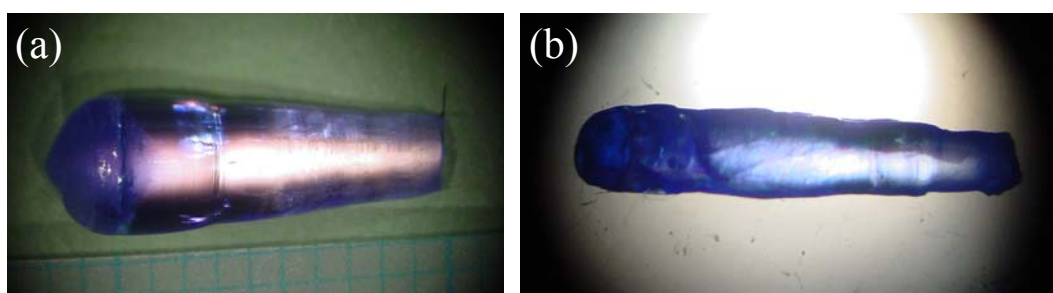


Fig.4.3.1 As-grown crystal of $\text{Ca}_2\text{Mg}_{0.9}\text{Zn}_{0.1}\text{Si}_2\text{O}_7$ (a) and $\text{Ca}_2\text{Mg}_{0.3}\text{Zn}_{0.7}\text{Si}_2\text{O}_7$ (b). The light blue color crystals correspond to a length of *ca.* 10 mm.

4.3 Investigations of $\text{Ca}_2\text{Mg}_{1-x}(\text{Zn}, \text{Co})_x\text{Si}_2\text{O}_7$ with modulated structure

Besides these factors, the quality of the seed crystal is also important. Two different seed crystals were used for growing the end member $\text{Ca}_2\text{MgSi}_2\text{O}_7$. One seed crystal, grown by pulling a Pt wire from the melt, had several cracks, the other was of good quality with the crystallographic c axis parallel to the growing direction.

The crystal grown by the “cracked” seed crystal has cracks inside (Fig.4.3.2a). However, the crystal grown by the second seed crystal has no cracks (Fig.4.3.2b). Both as-grown crystals were free of bubbles and inclusions. On top of the crystal in Fig.4.3.2a, the evident crack marked by arrow is due to the fast cooling speed after finishing the growth. Therefore, always the lowest cooling speed of $1^\circ/\text{min}$ attainable by the cooling system has been used. The crystal length is *ca.* 10 mm.

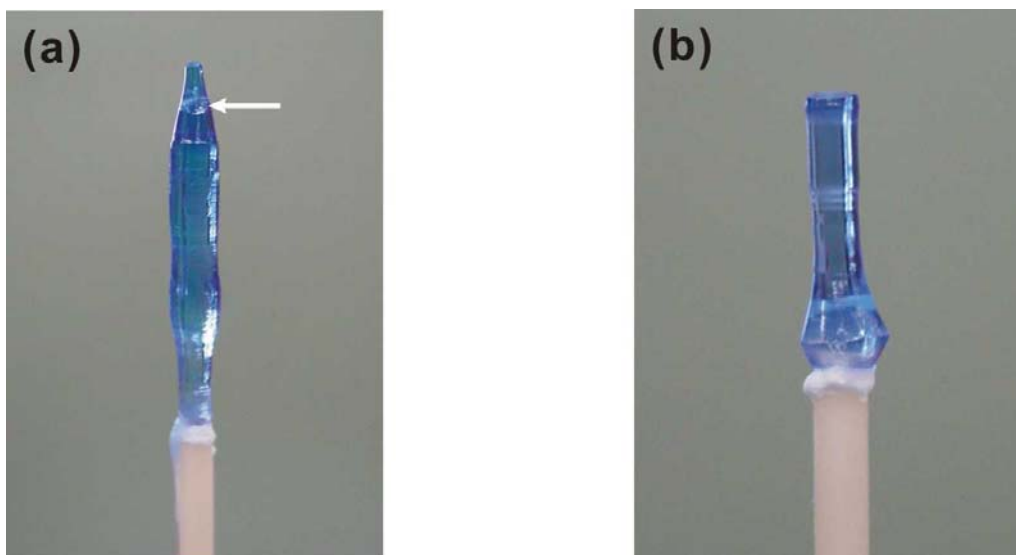


Fig.4.3.2 As-grown crystals of $\text{Ca}_2\text{MgSi}_2\text{O}_7$ using the seed crystals with different quality. (a) the seed crystal with some cracks grown by Pt wire as seed crystal; (b) the seed crystal of $\text{Ca}_2\text{MgSi}_2\text{O}_7$ with good quality and the crystallographic c axis paralleling to a growing direction

Thin polished sections cut from the bulk crystals were used for the SEM-EDS compositional analysis. The calculated results based on the EDS measurements are listed in Table 4.3.1. The measured concentrations of Zn are less than the corresponding nominal values. The difference between the nominal and the measured concentration of Zn increases with increasing Zn content of the raw material. This implies that there is still an evident evaporation of Zn despite the above-mentioned precautions.

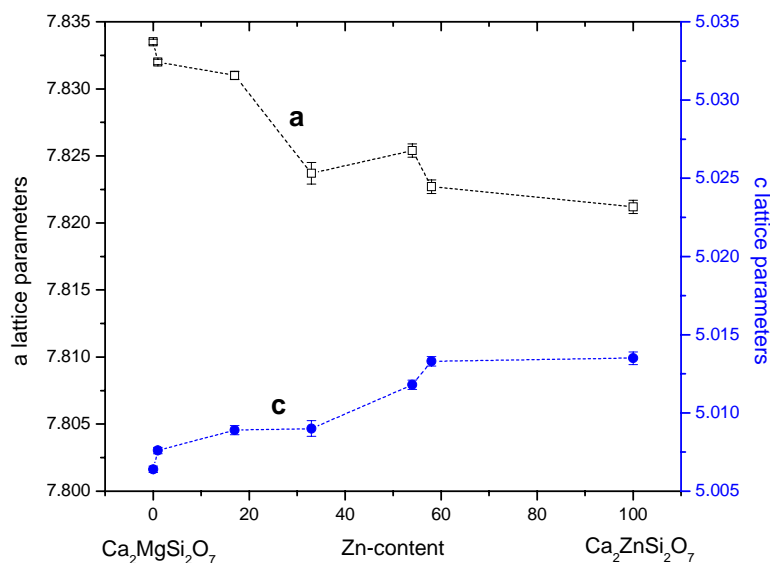
The XRD results show that all crystals are pure phases except the $\text{Ca}_2\text{Mg}_{0.5}\text{Zn}_{0.5}\text{Si}_2\text{O}_7$ crystal, which may be due to an unstable solid/liquid interface. The refined lattice constants for the Mg/Zn system are listed in Table 4.3.2 and plotted in Fig.4.3.3.

Table 4.3.1 Analyses of $\text{Ca}_2\text{Mg}_{1-x}\text{Zn}_x\text{Si}_2\text{O}_7$ crystals by SEM-EDS

Nominal x	Measured x	Analyzed formula
0.0	0.0	$\text{Ca}_{2.06}\text{Mg}_{0.97}\text{Si}_{1.97}\text{O}_7$
0.1	0.01	$\text{Ca}_{2.05}\text{Mg}_{0.99}\text{Zn}_{0.01}\text{Si}_{2.02}\text{O}_7$
0.3	0.17	$\text{Ca}_{2.06}\text{Mg}_{0.83}\text{Zn}_{0.17}\text{Si}_{2.03}\text{O}_7$
0.5	0.33	$\text{Ca}_{1.89}\text{Mg}_{0.67}\text{Zn}_{0.33}\text{Si}_{2.02}\text{O}_7$
0.7	0.54	$\text{Ca}_{1.88}\text{Mg}_{0.46}\text{Zn}_{0.54}\text{Si}_{2.03}\text{O}_7$
0.9	0.58	$\text{Ca}_{1.88}\text{Mg}_{0.42}\text{Zn}_{0.58}\text{Si}_{2.07}\text{O}_7$
1.0	1.0	$\text{Ca}_{1.94}\text{Zn}_{1.00}\text{Si}_{2.06}\text{O}_7$

Table 4.3.2 Lattice constants in the system $\text{Ca}_2\text{MgSi}_2\text{O}_7 - \text{Ca}_2\text{ZnSi}_2\text{O}_7$

Zn/(Mg + Zn)	a (Å)	c (Å)	V (Å ³)
0.0	7.8335(2)	5.0061(2)	307.193
0.01	7.8320(2)	5.0076(2)	307.163
0.17	7.8310(3)	5.0089(3)	307.173
0.33	7.8237(8)	5.0090(5)	306.607
0.54	7.8254(5)	5.0118(3)	306.910
0.58	7.8227(5)	5.0133(3)	306.787
1.0	7.8212(5)	5.0135(4)	306.684

Fig.4.3.3 Lattice parameters a and c of the system $\text{Ca}_2\text{MgSi}_2\text{O}_7 - \text{Ca}_2\text{ZnSi}_2\text{O}_7$.

With increasing Zn concentration, a decreases and c increases. This variation is unusual as compared to the systems $\text{Ca}_2\text{MgSi}_2\text{O}_7$ - $\text{Ca}_2\text{FeSi}_2\text{O}_7$ [5] and $\text{Ca}_2\text{MgSi}_2\text{O}_7$ - $\text{Ca}_2\text{CoSi}_2\text{O}_7$ [49]. In general, the substitution of large tetrahedral cations in T^1 -sites results in an increase in the dimensions of the tetrahedral sheet. As the tetrahedral sheets expand, the lattice constant a increases [19]. The reverse result obtained here for the substitution of Zn with $r_{\text{ion}} = 0.60\text{\AA}$ for Mg with $r_{\text{ion}} = 0.58\text{\AA}$ suggests that the Zn ion pushes up the Ca ion located between two sheets of tetrahedral five-member rings to vertical direction rather than expands the five-member rings laterally.

4.3.1.2 Incommensurate-to-normal phase transition

It is well known that the end-members of $\text{Ca}_2\text{MgSi}_2\text{O}_7$ and $\text{Ca}_2\text{ZnSi}_2\text{O}_7$ exhibit an incommensurate structure at room temperature. The incommensurate phase (I) is an intermediate state and can transform into the high-temperature phase (normal phase, N) or into the low-temperature commensurate phase (C). There are several ways to study the phase transition, such as XRD, TEM and DSC. Fig.4.3.4 shows the temperature dependence of the heat capacity measured by DSC around the I-N phase transition point of the solid solution series. Comparing Fig.4.3.4a with Fig.4.3.4b, there is no hysteresis during the phase transition.

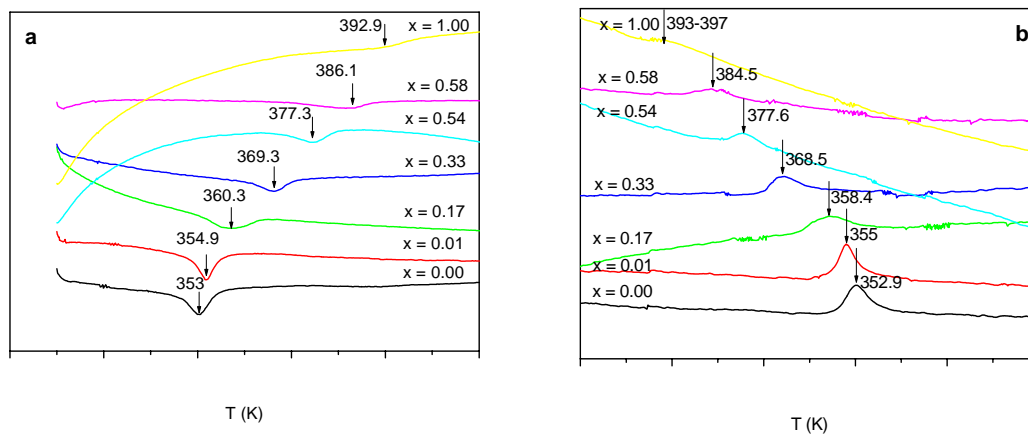


Fig.4.3.4 Temperature dependence of the heat capacity around the I-N transition point of $\text{Ca}_2\text{Mg}_{1-x}\text{Zn}_x\text{Si}_2\text{O}_7$ solid solutions. T_{I-N} is marked in the corresponding curves by an arrow. (a) heat capacity with increasing temperature from 323K to 413K; (b) heat capacity with decreasing temperature from 413K to 323K.

The endothermic and exothermic peaks are quite sharp for the end member $\text{Ca}_2\text{MgSi}_2\text{O}_7$. A broadening of the peak is observed with increasing Zn content. In spite of this, a weak λ shape of the peak can still be observed. It indicates the presence of dynamical fluctuations^[52]. The transition temperature T_{I-N} of the end member $\text{Ca}_2\text{MgSi}_2\text{O}_7$ is 353K. This temperature is consistent with the data measured by TEM^[5], but different from other DSC (348-358K) and NMR (385K) data in the literature^[4, 31]. T_{I-N} increases with increasing Zn concentration and reaches 393K for Zn-åkermanite, which is lower than 402.6K measured by Iishi et al.^[53]. Heat capacity anomaly is sensitive to the crystal quality^[4], synthesizing temperature^[5] and the preparation method as well as the sample form^[53]. The difference of T_{I-N} measured from us and Iishi et al. can be due to the synthesizing method.

Merwin et al.^[31] observed the strongest changes in the NMR spectra of the pure Mg-åkermanite at 385K, which has a large difference from our and other DSC results. This difference might indicate that NMR data show only short-range order and do not seem responsive to long-range ordering effects.

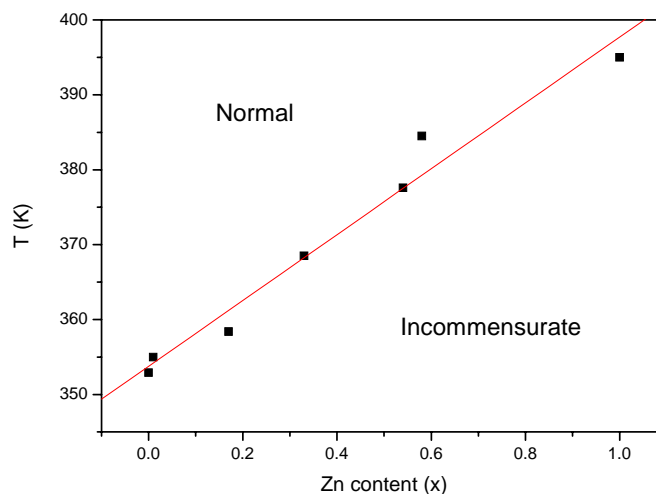


Fig.4.3.5 Dependence of transition temperature on Zn content in $\text{Ca}_2\text{Mg}_{1-x}\text{Zn}_x\text{Si}_2\text{O}_7$ system.

The broadening of the peaks with increasing Zn concentration can also be explained by the existence of dislocations in the sample. The density of dislocations in crystals increases with increasing Zn concentration due to the evaporation of Zn. Despite the effect of the sample quality on the heat capacity anomaly, one can generalize the trend of the transition from incommensurate to normal phase. Fig.4.3.5

exhibits the phase diagram of $\text{Ca}_2\text{Mg}_{1-x}\text{Zn}_x\text{Si}_2\text{O}_7$ solid solution, which indicates an almost linear increase of T_{I-N} with the $\text{Zn}/(\text{Mg} + \text{Zn})$ ratio.

4.3.2 The $\text{Ca}_2\text{Mg}_{1-x}\text{Co}_x\text{Si}_2\text{O}_7$ system

4.3.2.1 Average structure

As revealed by X-ray diffraction, the average structure of the melilite group shows tetrahedral symmetry with the space group $P\bar{4}2_1m$. The projection of this basic structure along the $[001]$ direction is shown in Fig.4.3.6. A dashed square represents the unit cell while a dotted square represents the subunit including one $(\text{Mg},\text{Co})\text{O}_4$ tetrahedron and one Si_2O_7 dimer. Fig.4.3.7 shows an electron diffraction pattern of the average structure of $\text{Ca}_2\text{Mg}_{0.75}\text{Co}_{0.25}\text{Si}_2\text{O}_7$ crystal taken along the $[001]$. Only the Bragg reflections of the unmodulated basic structure are observed.

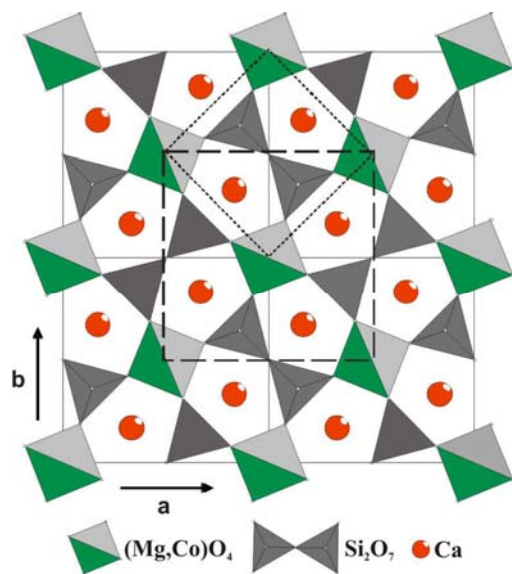


Fig.4.3.6 Projection of the melilite structure along the c -direction.

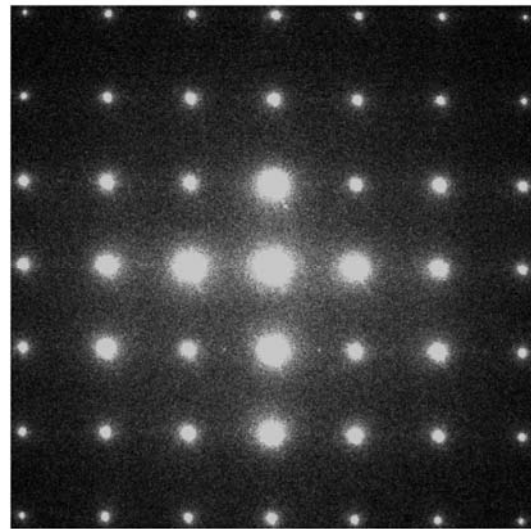


Fig.4.3.7 Electron diffraction pattern of the average structure of $\text{Ca}_2\text{Mg}_{0.75}\text{Co}_{0.25}\text{Si}_2\text{O}_7$.

The corresponding high-resolution image in Fig.4.3.8 exhibits the tetrahedral average structure. By choosing some strong diffraction dots from the Fourier transformation, a more clear structural image (Fig.4.3.8b) was obtained after Fourier-filtering, which is completely consistent with the simulation image (inserted).

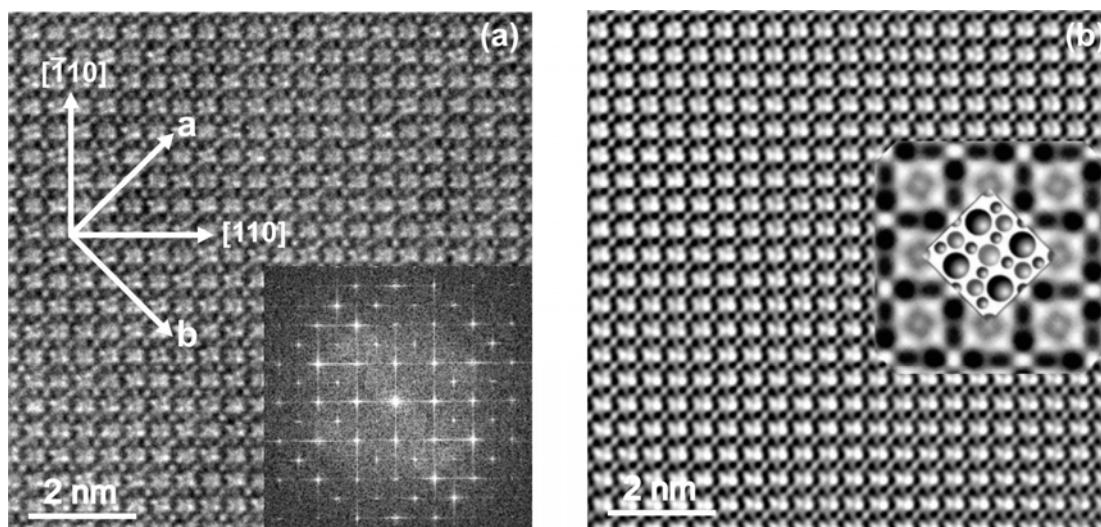


Fig.4.3.8 (a) High-resolution image and corresponding Fourier transformation showing the average structure of $\text{Ca}_2\text{Mg}_{0.75}\text{Co}_{0.25}\text{Si}_2\text{O}_7$; (b) inverse filtered Fourier transformation of (a) with the inserted multi-slice image simulation of the structure along with a model of the atomic positions within the unit cell.

4.3.2.2 Modulated structure

For the whole $\text{Ca}_2\text{MgSi}_2\text{O}_7$ - $\text{Ca}_2\text{CoSi}_2\text{O}_7$ åkermanite series, the incommensurate structure was detected by EDPs and HRTEM images in thicker sample regions. Fig.4.3.9 shows the complex [001] zone diffraction pattern of $\text{Ca}_2\text{Mg}_{0.9}\text{Co}_{0.1}\text{Si}_2\text{O}_7$ as well as a schematic representation of the same diffraction pattern.

The most intense spots form a square grid corresponding to the basic reflections due to the average structure. The first-, second- and even third-order of the modulation can be observed as marked by the numbers 1, 2 and 3, respectively, in Fig.4.3.9b. Normally, the intensity of these satellite spots weakens from the first to the second and to the third order as observed from the experimental EDP. Relatively intense satellites, which are due to combinations of the two modulation vectors, e.g. $\mathbf{q}_1 + \mathbf{q}_2$ and $\mathbf{q}_1 - \mathbf{q}_2$, are also formed symmetrically on both [100] and [010] directions between two basic reflections, which confirm that the modulation is two-dimensional rather than the superposition of two one-dimensional modulations.

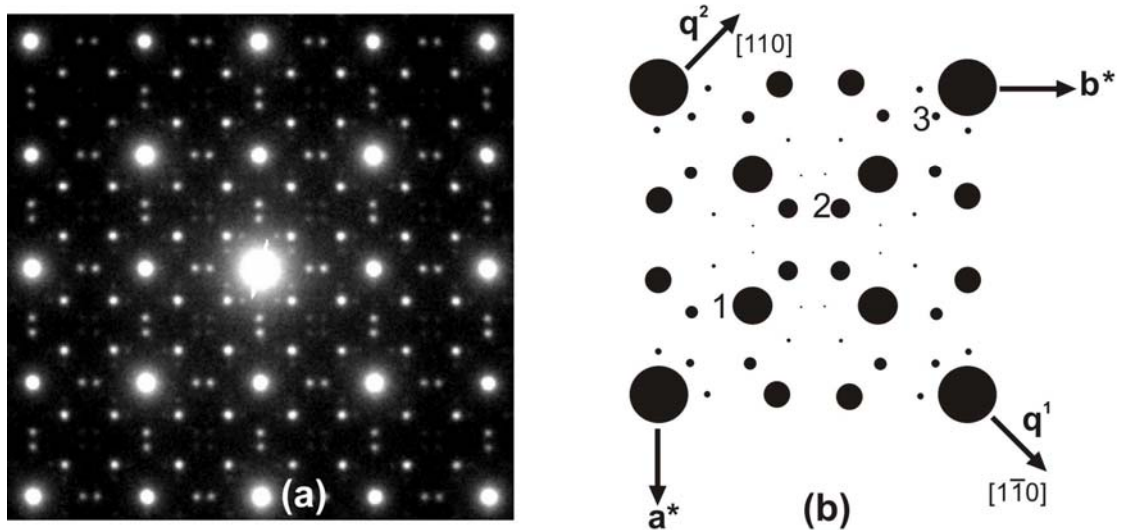


Fig.4.3.9 (a) Electron diffraction pattern of $\text{Ca}_2\text{Mg}_{0.9}\text{Co}_{0.1}\text{Si}_2\text{O}_7$ along $[001]$ direction; (b) a schematic drawing of one enlarged reciprocal unit cell. The first-, second- and third-order satellites are indicated by numbers.

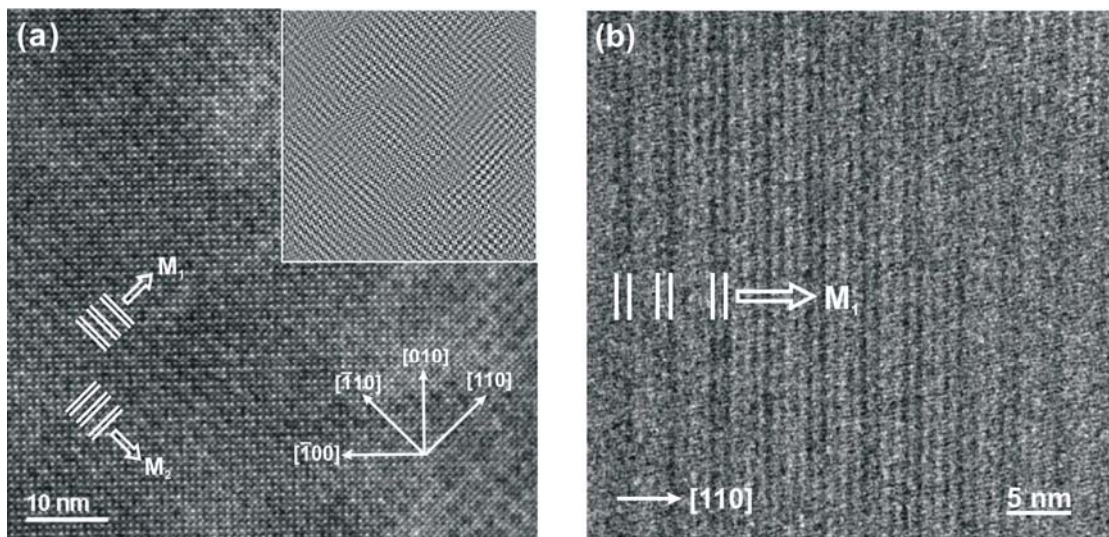


Fig.4.3.10 (a) A medium resolution image of $\text{Ca}_2\text{Mg}_{0.9}\text{Co}_{0.1}\text{Si}_2\text{O}_7$ taken along the $[001]$ direction. The two-dimensional modulation is indicated by M_1 and M_2 . A “tartan-like” pattern is formed by intertwining of the modulation waves, which can be observed clearly from the inverse filtered Fourier transformation (inserted); (b) a high-resolution image of $\text{Ca}_2\text{Mg}_{0.5}\text{Co}_{0.5}\text{Si}_2\text{O}_7$ taken along $[113]$ direction. One-dimensional modulation is revealed from the image.

The two-dimensional modulation along $[110]$ and $[\bar{1}10]$ is directly observed in Fig.4.3.10a, which shows a “tartan-like” pattern. This is revealed more clearly in the inverse filtered Fourier transformation (inserted in Fig.4.3.10a). Such “tartan-like”

pattern indicates the existence of nanometer-sized domains as observed in $\text{Ca}_2\text{ZnGe}_2\text{O}_7$ [28]. The modulation wavelength measured directly from the image is about 21.8 Å. This value corresponds very closely to four times the dimension of a subunit (5.53 Å). Along the modulation direction atomic arrays are detected which alternatively show variations in density and brightness of the dots as indicated by two parallel lines. This should be due to the overlapping of octagonal cell arrangements as drawn in Fig.4 of literature [30]. A similar feature is observed in Fig.4.3.10b, but only one-dimensional along [110].

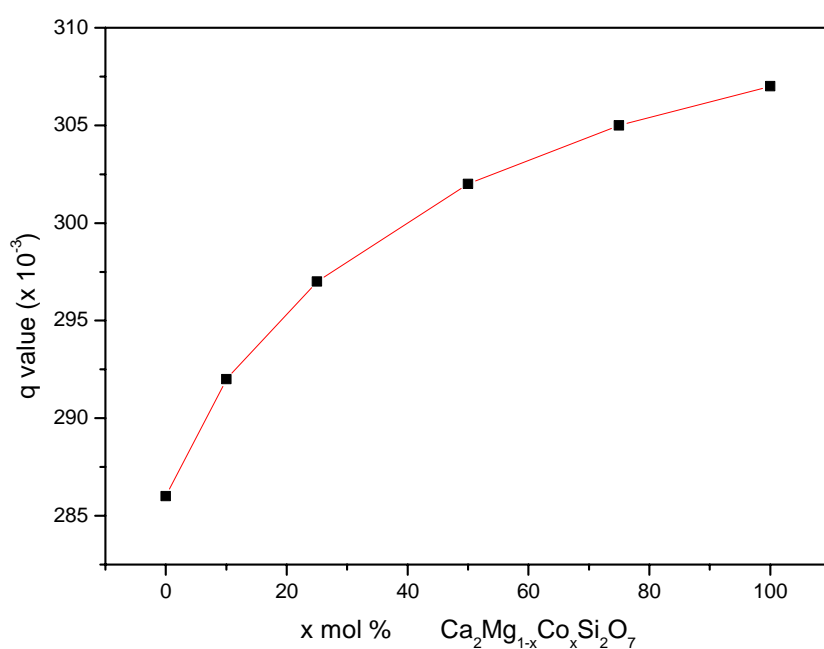


Fig.4.3.11 The q -value as a function of Co-content in $\text{Ca}_2\text{Mg}_{1-x}\text{Co}_x\text{Si}_2\text{O}_7$ crystals. The value of every dot was the average of seven measured data from the corresponding EDPs.

The incommensurate structural modulation of the $\text{Ca}_2\text{Mg}_{1-x}\text{Co}_x\text{Si}_2\text{O}_7$ system was observed in the whole range of x at room temperature. The modulation vector q calculated from the corresponding EDPs is plotted in Fig.4.3.11. With increasing amount of Co, the modulation vector increases from 0.280 for $\text{Ca}_2\text{MgSi}_2\text{O}_7$ to 0.307 for $\text{Ca}_2\text{CoSi}_2\text{O}_7$. This tendency is the same as that observed by Seifert et al. [5] in synthetic $\text{Ca}_2\text{MgSi}_2\text{O}_7$ - $\text{Ca}_2\text{FeSi}_2\text{O}_7$ system.

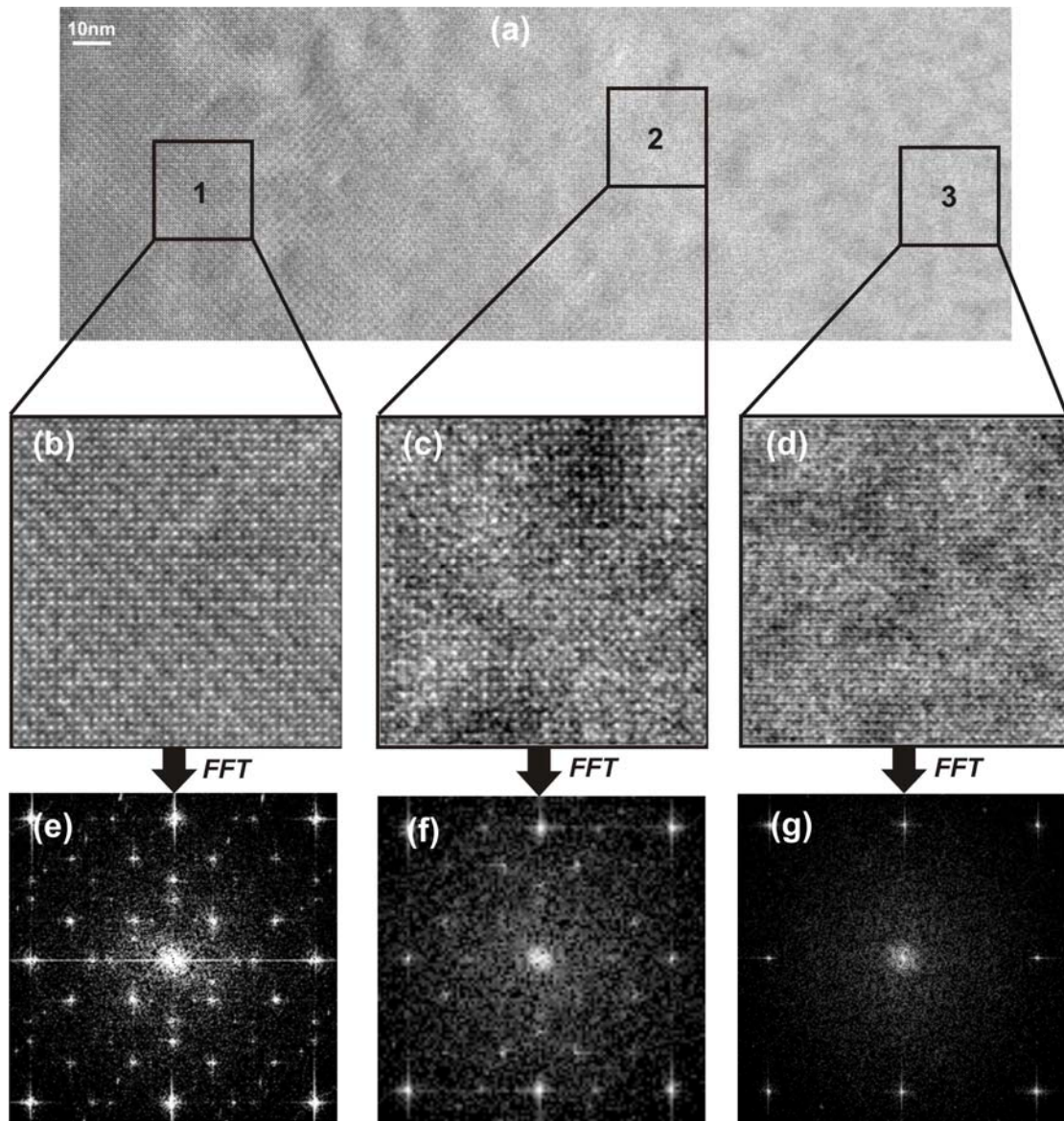


Fig.4.3.12 A medium image of $\text{Ca}_2\text{Mg}_{0.9}\text{Co}_{0.1}\text{Si}_2\text{O}_7$ crystal revealing different structural information (a). Two-dimensional modulation observed by enlarged image (b) and the corresponding FFT (e) in thick area of the sample. One-dimensional modulation revealed from (c, f) and the unmodulated structure (d, g).

A medium resolution image of $\text{Ca}_2\text{Mg}_{0.9}\text{Co}_{0.1}\text{Si}_2\text{O}_7$ with the large area is shown in Fig.4.3.12a. Thickness of the sample increases from the right to the left according to the wedge shape, which can be distinguished by changeable contrast. Two-dimensional modulation was observed from area 1 (Fig.4.3.12b, e). In area 2, one can observe one-dimensional modulation or the modulation exhibiting stronger in one direction than another direction (Fig.4.3.12c, f). The unmodulated structure is revealed in the area 3 (Fig.4.3.12d, g).

The atomic position of the heavy cation of the constituent atom can be distinguished from these high-resolution images, but the position of oxygen can not be discerned. The resolution limitation of TEM itself and the weak scattering of the light oxygen atom to the electron beam are reasons for that. In the modulated structure, it is more difficult to resolve the atomic position. Although images are always taken in the thin area, many layers of tetrahedral sheets are still included and the overlapping of atoms also lowers the resolution.

The observations in a thick area show the two-dimensional incommensurate modulation of $\text{Ca}_2\text{Mg}_{1-x}\text{Co}_x\text{Si}_2\text{O}_7$ system at room temperature. Dark lines with spacing of 3 and 4 subunits are observed along the two modulation directions and alternating microdomains separated by such lines exhibit slightly different brightness as investigated by von Heurck et al. [28]. They also observed various arrangements of octagons from high-resolution images using a smaller objective aperture. At room temperature, such arrangements of octagons partly overlap in a non-periodic way, but almost completely overlap in the low-temperature lock-in structure as confirmed by Schaper et al. [30].

4.3.3 Conclusions

The series of $\text{Ca}_2\text{Mg}_{1-x}\text{Zn}_x\text{Si}_2\text{O}_7$ crystals were grown by floating zone melting method. The evaporation of Zn and the quality of a seed crystal influence the final crystal quality. T_{1-N} increases with the increase of the ratio of $\text{Zn}/(\text{Mg} + \text{Zn})$ from 353K for $\text{Ca}_2\text{MgSi}_2\text{O}_7$ to 393K for $\text{Ca}_2\text{ZnSi}_2\text{O}_7$.

The average structure of melilites was exhibited by the high-resolution image and electron diffraction patterns in thin area in $\text{Ca}_2\text{Mg}_{1-x}\text{Co}_x\text{Si}_2\text{O}_7$ system and all heavy cation can be distinguished. Two-dimensional incommensurate modulation was observed in thick area of the sample. The existence of microdomain structure was revealed from high-resolution images.

4.4 Modulation and phase transitions of $\text{Ca}_2\text{Co}_{1-x}\text{Zn}_x\text{Si}_2\text{O}_7$ in dependence on temperature and composition

In this section, first the crystal characterization is described. The average structure was resolved by high-resolution imaging and simulation. The two-dimensionally modulated structure, including the variation of the modulation with the atomic substitution as well as of the microdomain morphology, was studied by TEM. The phase transition behavior was revealed by electron diffraction and thermal analysis. The domains and discommensurations (DCs) formed during the phase transition are described in detail. Finally, the crystal structure of the commensurate phase of $\text{Ca}_2\text{Co}_{0.9}\text{Zn}_{0.1}\text{Si}_2\text{O}_7$ was refined by XRD according to the orthorhombic space group $P2_12_12$ and the commensurate modulation was discussed.

4.4.1 Crystal growth and characterization

Crystals of the series of $\text{Ca}_2\text{Co}_{1-x}\text{Zn}_x\text{Si}_2\text{O}_7$ with $x = 0.0, 0.1, 0.3, 0.5, 0.7, 0.9, 1.0$ were grown by the FZ melting method. The charge rod and the seed crystal were centered and mounted on the upper and lower shafts, respectively. The charge rod was counter-rotated relatively to the rotation of the seed crystal with a speed of 40 rpm. The growth rates were chosen between 0.5-1.2 mm/h.

The charge rods showed a color from pale blue to deep blue and, therefore, absorb effectively the radiation energy, which is indicated by the close value between the melting voltage and the stable voltage during growth. Supplementary 1 mol % ZnO was added to all nominal charges except the end-member $\text{Ca}_2\text{CoSi}_2\text{O}_7$ for compensating the loss of ZnO during the growth process.

As already mentioned, low speeds have the advantage of avoiding possible crack formations, the occurrence of bubbles, or inclusions. However, a too low growing speed (< 0.5 mm/h) increases the unbalance of the components in the zone melting process due to the evaporation of ZnO. On the other hand, high growing speeds (> 1.2 mm/h) may cause the formation of bubbles in the bulk. Therefore, in most experiments, a speed of 1.0 mm/h was used. Note that under the condition of low oxygen pressure, bubble-free crystals could be obtained at a growing speed higher than the one in air atmosphere.

Fig.4.4.1 shows macroscopic pictures of two as-grown crystals of the $\text{Ca}_2\text{Co}_{1-x}\text{Zn}_x\text{Si}_2\text{O}_7$ system. The formation of microcracks approaching the crystal surface was observed when the ratio of $\text{Zn}/\text{Co}+\text{Zn}$ reached 0.5. These cracks increased in number with increasing Zn content or prolonging the time of growth. Nevertheless, good crystals could be obtained even at Zn contents as high as 70%.

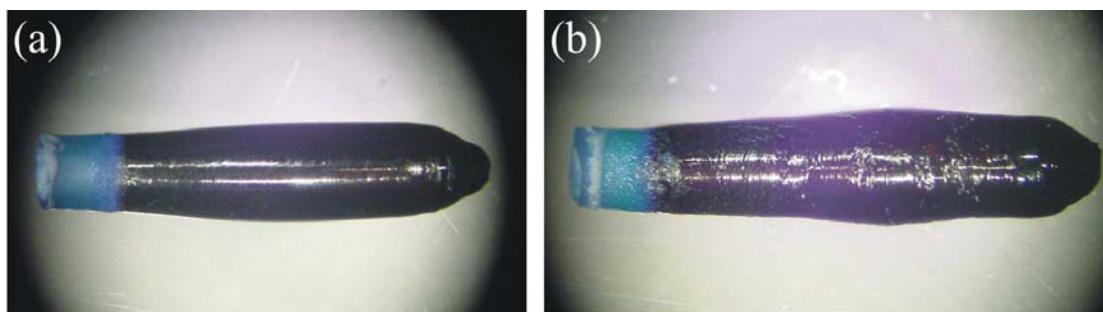


Fig.4.4.1 Single crystals of $\text{Ca}_2\text{Co}_{0.7}\text{Zn}_{0.3}\text{Si}_2\text{O}_7$ (a) and $\text{Ca}_2\text{Co}_{0.3}\text{Zn}_{0.7}\text{Si}_2\text{O}_7$ (b) grown at *ca.* 1320 °C. The region of deep blue color corresponds to a length of 10mm; on the left hand side the seed crystal is seen.

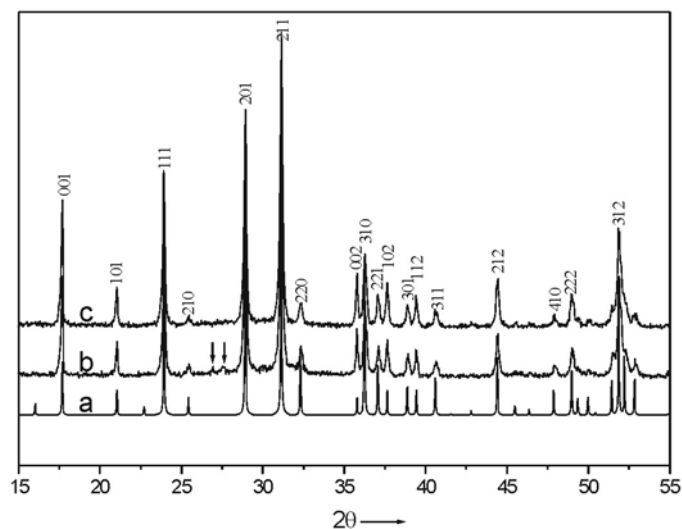


Fig.4.4.2 XRD diagram of a $\text{Ca}_2\text{ZnSi}_2\text{O}_7$ crystal: a) data of the ICSD standard; b) first as-grown crystal with large melting zone; c) second crystal grown applying a small melting zone. The arrows indicate peaks originating from the $\text{Ca}_3\text{Si}_3\text{O}_9$ phase.

The growth of high purity crystal phases by the FZ technique generally requires a careful control of the growth conditions and, in some cases, several repeats of the growing run. For instance, in the end-member $\text{Ca}_2\text{ZnSi}_2\text{O}_7$ a certain amount of

4.4 Modulation and phase transitions of $\text{Ca}_2\text{Co}_{1-x}\text{Zn}_x\text{Si}_2\text{O}_7$

$\text{Ca}_3\text{Si}_3\text{O}_9$ has been found after the first experimental run: 5% according to the results of XRD refinement (Fig.4.4.2a, b). Efforts to lower the evaporation of ZnO in a second run have been successful through adjusting the zone volume to a size as small as possible (Fig.4.4.2c).

All grown crystals were characterized by X-ray diffraction. The calculated and observed relative intensities of the $\text{Ca}_2\text{Co}_{1-x}\text{Zn}_x\text{Si}_2\text{O}_7$ samples are in a good agreement, which indicates a pure phase. The results for the example of $\text{Ca}_2\text{Co}_{0.5}\text{Zn}_{0.5}\text{Si}_2\text{O}_7$ are listed in Table 4.4.1 and plotted in Fig.4.4.3.

Table 4.4.1 Indices, 2 theta values, d-spacing and calculated and observed relative intensities of XRD analysis of $\text{Ca}_2\text{Co}_{0.5}\text{Zn}_{0.5}\text{Si}_2\text{O}_7$

h	k	l	2Theta	d-spacing	$I_{\text{calc.}}$	$I_{\text{obs.}}$
0	0	1	17.653	5.02019	76	75
0	1	1	21.004	4.22617	26	26
1	1	1	23.908	3.71904	94	94
0	2	1	28.897	3.08723	138	155
1	2	1	31.115	2.87205	232	241
2	2	0	32.312	2.76835	18	17
0	0	2	35.743	2.51009	33	33
1	3	0	36.251	2.47609	58	58
2	2	1	37.054	2.42419	23	23
0	1	2	37.600	2.39028	30	37
0	3	1	38.858	2.31575	16	20
1	1	2	39.382	2.28613	19	21
1	3	1	40.593	2.22066	15	15
1	2	2	44.368	2.04010	48	47
1	4	0	47.860	1.89907	13	12
2	2	2	48.944	1.85952	30	29
1	4	1	51.402	1.77623	17	19
1	3	2	51.823	1.76276	101	106
2	4	0	52.202	1.75086	24	21
3	3	1	52.807	1.73222	16	14
1	1	3	57.487	1.60183	20	24
0	2	3	60.080	1.53873	20	21
1	2	3	61.352	1.50985	26	27
1	5	1	63.279	1.46844	15	16
2	4	2	64.879	1.43602	10	10
2	2	3	65.080	1.43209	21	22
0	3	3	66.297	1.40872	11	12
2	5	1	66.947	1.39661	15	15
1	3	3	67.502	1.38646	11	12
1	4	3	75.691	1.25551	15	17
0	0	4	75.724	1.25505	15	16
3	3	3	76.833	1.23968	12	14

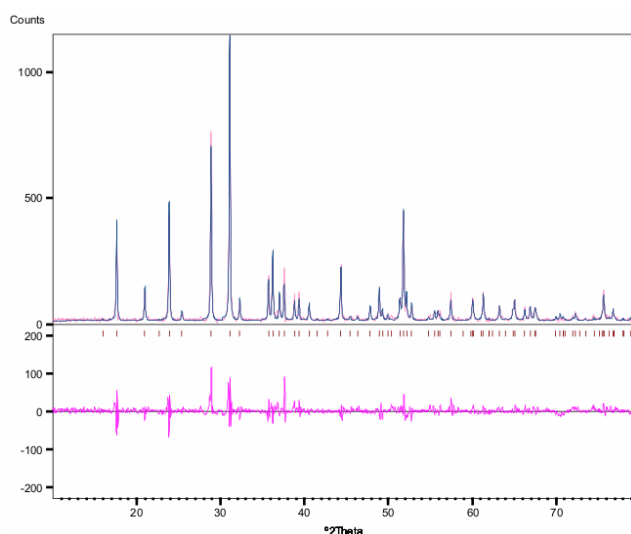


Fig.4.4.3 XRD diagram of $\text{Ca}_2\text{Co}_{0.5}\text{Zn}_{0.5}\text{Si}_2\text{O}_7$ indicating the observed (blue line) and the calculated (red line) results. The difference between both is shown in the lower part.

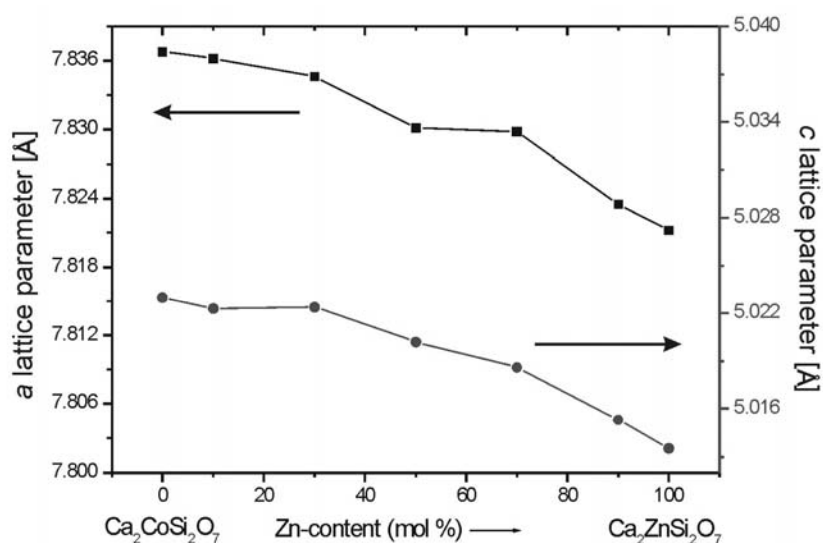


Fig.4.4.4 XRD lattice parameters a and c versus composition in the system $\text{Ca}_2\text{Co}_{1-x}\text{Zn}_x\text{Si}_2\text{O}_7$.

The refined lattice constants of $\text{Ca}_2\text{Co}_{1-x}\text{Zn}_x\text{Si}_2\text{O}_7$ obtained from the Rietveld analysis are plotted in Fig.4.4.4. Because of the general rule that the substitution of the T^I -sites by larger tetrahedral cations should result in an increase in the dimensions of the tetrahedral sheet, an increase of the a lattice parameter should be expected^[53]. In the present system, the ionic radius of Zn^{2+} (0.60\AA) is larger than that of Co^{2+}

4.4 Modulation and phase transitions of $\text{Ca}_2\text{Co}_{1-x}\text{Zn}_x\text{Si}_2\text{O}_7$

(0.57Å), the experimental finding, however, is a decrease in both a and c cell parameters with increasing Zn concentration. The explanation of this behavior lies in the particular changes of the bond lengths of $\text{T}^1\text{-O}_3$, Si-O and Ca-O . In comparison with the single crystal data of the end-member $\text{Ca}_2\text{CoSi}_2\text{O}_7$ [19], the bond lengths in $\text{Ca}_2\text{ZnSi}_2\text{O}_7$ [54] are shortened by a considerable amount which explains the tendency of decreasing lattice constants.

Table 4.4.2 The compositional analysis of $\text{Ca}_2\text{Co}_{1-x}\text{Zn}_x\text{Si}_2\text{O}_7$ by EDS

Nominal x	Measured x	Analyzed formula
0.0	0.0	$\text{Ca}_{1.98}\text{Co}_{0.98}\text{Si}_{2.04}\text{O}_7$
0.1	0.13	$\text{Ca}_{1.99}\text{Co}_{0.87}\text{Zn}_{0.13}\text{Si}_{2.01}\text{O}_7$
0.3	0.30	$\text{Ca}_{1.89}\text{Co}_{0.70}\text{Zn}_{0.30}\text{Si}_{2.06}\text{O}_7$
0.5	0.50	$\text{Ca}_{2.0}\text{Co}_{0.50}\text{Zn}_{0.50}\text{Si}_{2.04}\text{O}_7$
0.7	0.69	$\text{Ca}_{1.96}\text{Co}_{0.31}\text{Zn}_{0.69}\text{Si}_{2.05}\text{O}_7$
0.9	0.84	$\text{Ca}_{2.02}\text{Co}_{0.16}\text{Zn}_{0.84}\text{Si}_{2.22}\text{O}_7$
1.0	1.0	$\text{Ca}_{1.94}\text{Zn}_{1.00}\text{Si}_{2.06}\text{O}_7$



Fig.4.4.5 Density map of Ca, Co, Zn and Si elements in $\text{Ca}_2\text{Co}_{0.9}\text{Zn}_{0.1}\text{Si}_2\text{O}_7$ bulk crystal detected by EDS.

The compositional analysis of this series was carried out by SEM-EDS and the results are listed in Table 4.4.2. The measured values are very close to the nominal ones for most compositions. Zn evaporation was lowered greatly in this system. The crystal quality was higher as compared to the Mg/Zn-system. This was confirmed by a polarized optical microscopy of thin cross-sections as well as by chemical mappings in the SEM-EDS mode (Fig.4.4.5). The results show that all constituent elements are distributed uniformly in the crystal.

4.4.2 The average structure observed by high-resolution transmission electron microscopy and corresponding image simulation

The observation of the structure from the atomic resolution image is still lacking. High-resolution micrographs of the relevant average structure of the incommensurate phase can be obtained from very thin parts of the specimen. The images in Fig.4.4.6a and b of the $\text{Ca}_2\text{CoSi}_2\text{O}_7$ sample taken at 1250kV reveal the average orthorhombic Co-melilite structure. The positions of the heavy atoms Ca and Co in the unit cell can be seen clearly. Although the Si and O atom positions are not really resolved, the dimer in the unit cell can be discerned. The corresponding simulated image (Fig.4.4.6c) is in good agreement with the experimental one and is helpful for estimating the Si and O positions in the experimental high-resolution image.

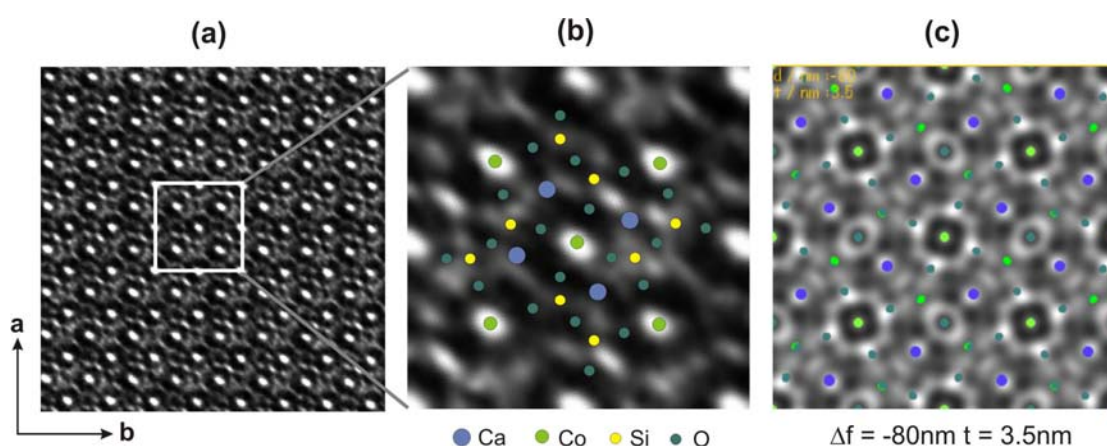


Fig.4.4.6 (a) High-voltage, high-resolution transmission electron micrograph of a thin specimen area of a Co-melilite crystal; (b) close-up of the region marked in a) with the atoms indication overlaid; (c) multi-slice image simulation showing the positions of all constituent atoms in the unit cell.

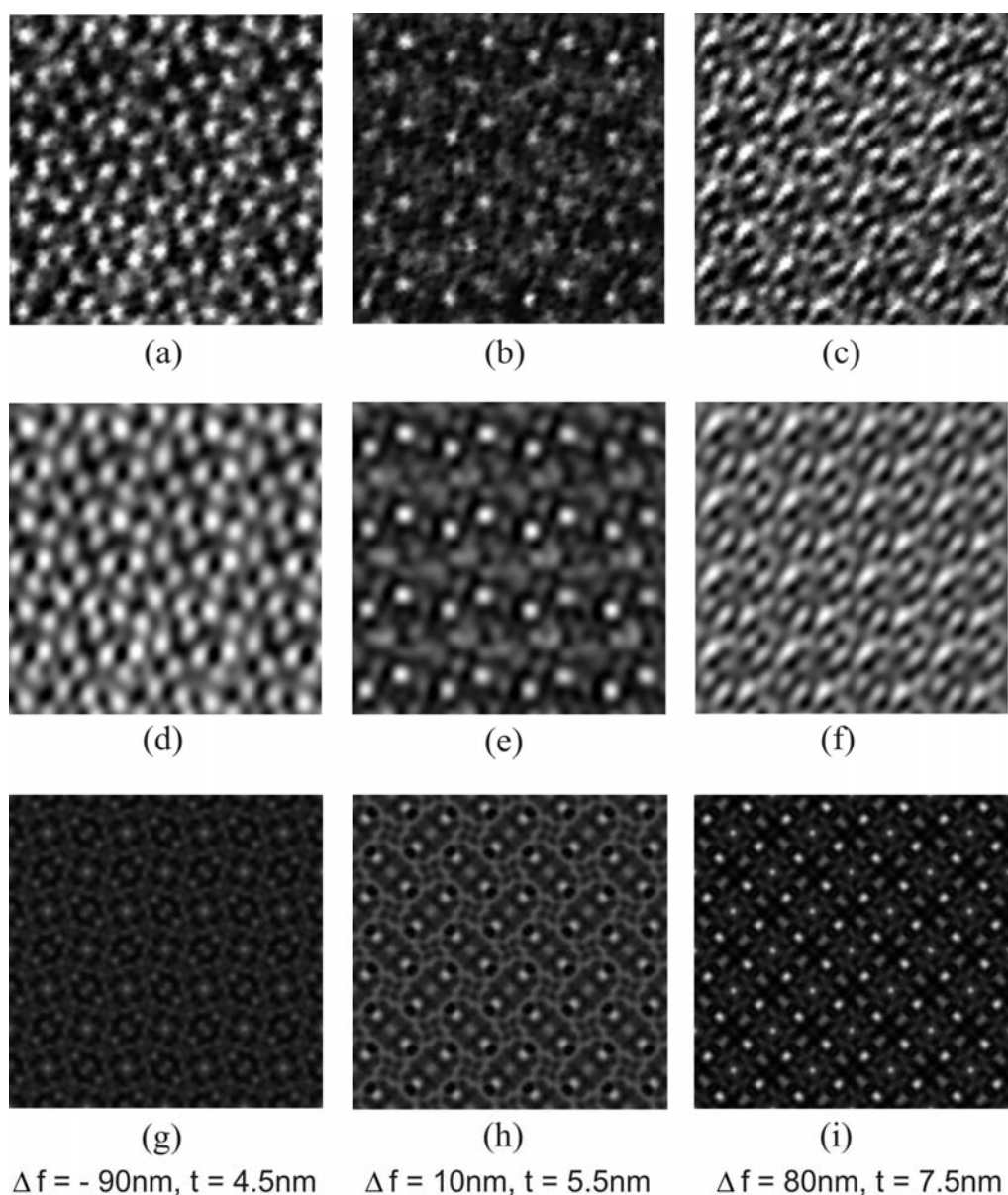


Fig.4.4.7 (a-c) High-resolution images of different areas of thin specimens of $\text{Ca}_2\text{CoSi}_2\text{O}_7$ taken by ARM-1250 microscope showing the average structure of the incommensurate phase; (d-f) The corresponding Fourier-filtered images by selecting most intense diffraction spots; (g-i) multislice image simulation for different defocus and thickness conditions using the EMS software package.

Fig.4.4.7a-c shows how the contrast of the lattice atoms varies with different defocus and specimen thickness conditions. The inverse fast Fourier transforms (IFFT) of the images by selecting the most intense diffraction spots provide better image contrasts and a clearer structure imaging (Fig.4.4.7d-f). Corresponding multislice image simulations are shown in Fig.4.4.7g-i for a variety of defocus and thickness conditions. High-resolution images have also been taken using JEM 3010 microscope.

Fig.4.4.8a-c shows three images taken at different defocus and thickness conditions by JEM 3010 microscope. The corresponding IFFT and image simulations are given for comparison (Fig.4.4.8d-i). Analyzing many high-resolution images, the experimental images always showed a certain degree of distortion relative to the corresponding simulations. Ruling out the error from operation and machine conditions, this kind of distortion may come from the existence of the modulation, which produces atomic shifts and deformation of the coordination polyhedra.

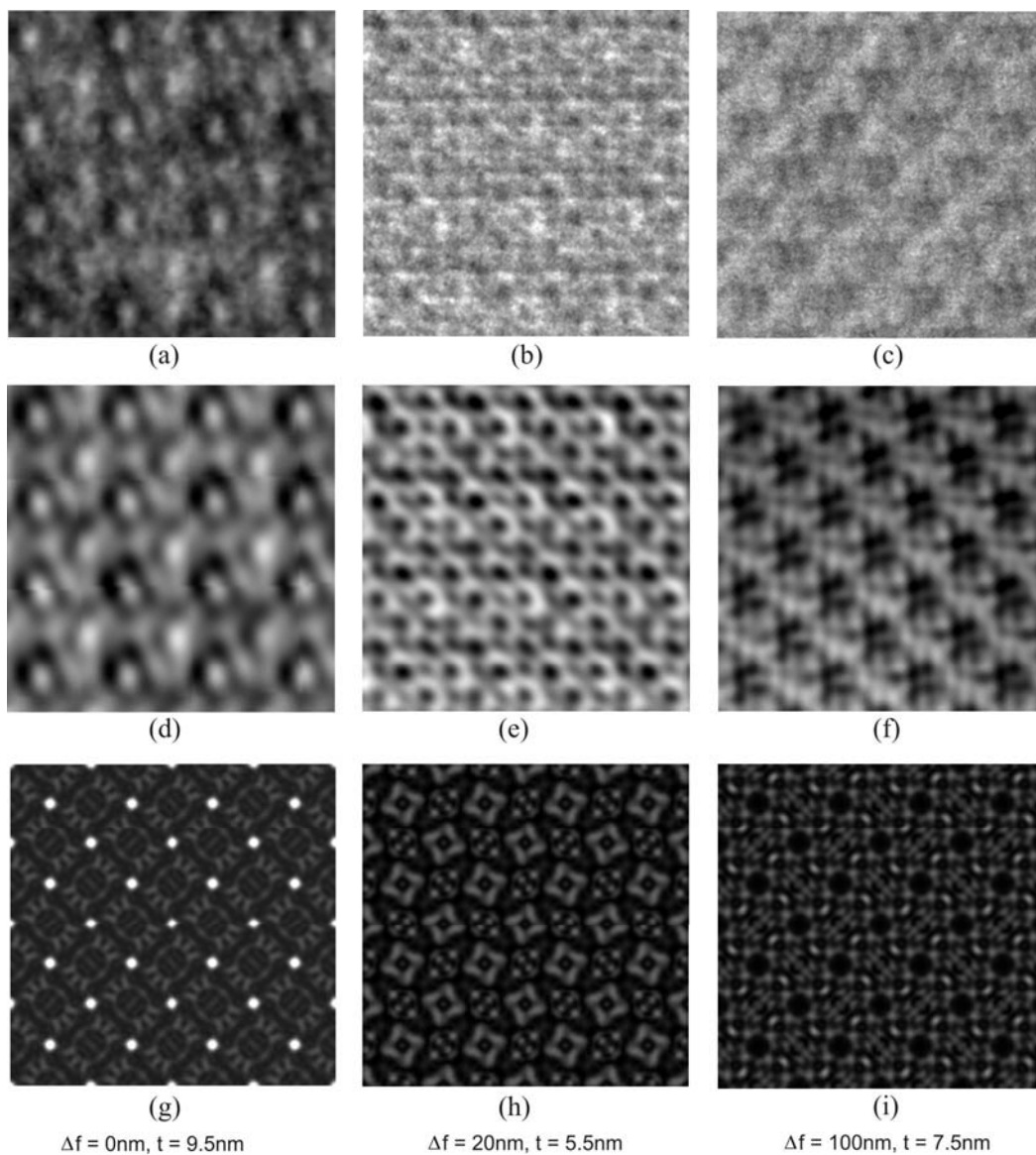


Fig.4.4.8 (a-c) High-resolution images of different areas of thin specimens of $\text{Ca}_2\text{Co}_{0.9}\text{Zn}_{0.1}\text{Si}_2\text{O}_7$ taken by JEM 3010 microscope showing the average structure of the incommensurate phase; (d-f) The corresponding Fourier-filtered images by selecting most intense diffraction spots; (g-i) multislice image simulation for different defocus and thickness conditions using the EMS software package.

4.4.3 Electron microscope studies of the modulated structure

In the $\text{Ca}_2\text{Co}_{1-x}\text{Zn}_x\text{Si}_2\text{O}_7$ system, satellite reflections of the modulated lattice were observed in the $(hk0)$ plane within the whole compositional range. Upon close inspection of the diffraction patterns, systematic differences are observed between low and high Zn content samples (Fig.4.4.9). While in the former the first and second order satellites are clearly observed, and even third order reflections are weakly to be detected, with increasing Zn content satellites higher than the first order disappear. This behavior is illustrated by the two selected diffraction patterns inserted in Fig.4.4.9 for the cases $x = 0.1$ (left inset), and $x = 0.7$ (right inset). As the diagram curve shows, the changes in the intensity of the satellites goes along with an initial increase and, above $x \sim 0.5$, nearly constant modulation wavelength in the $\langle 110 \rangle$ direction at room temperature. Thereby, the wavelength ranges from 18.27 Å to 19.21 Å.

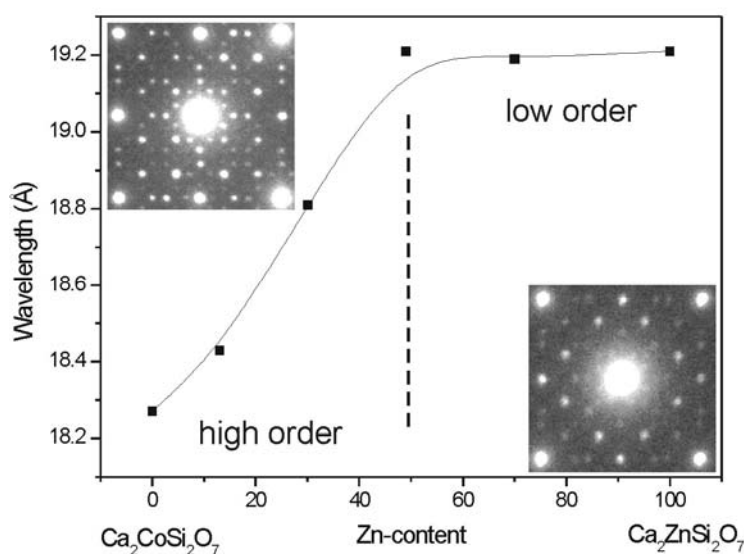


Fig.4.4.9 Variation of the modulation wavelength with increasing Zn content in $\text{Ca}_2\text{Co}_{1-x}\text{Zn}_x\text{Si}_2\text{O}_7$, and typical $[001]$ ED patterns for the case $x = 0.1$ (left inset) and $x = 0.7$ (right inset). Regions of high order (up to third order satellites are detectable), and of low order (only first order satellites are present) can be distinguished.

In an earlier publication Schosnig et al. ^[11] reported a very similar behavior of the satellite intensity of Sr-åkermanite in dependence on temperature during in situ heating and cooling experiments. They denoted two regions, well distinguished with respect to the appearance or disappearance of higher order satellites, to a high order

and a low order incommensurate phase so as in Fig.4.4.9. Evaluation of the intensity and broadening (FWHM) of the satellite reflections in x-ray diffraction studies by Kusz and Böhm ^[55] led to the same conclusion.

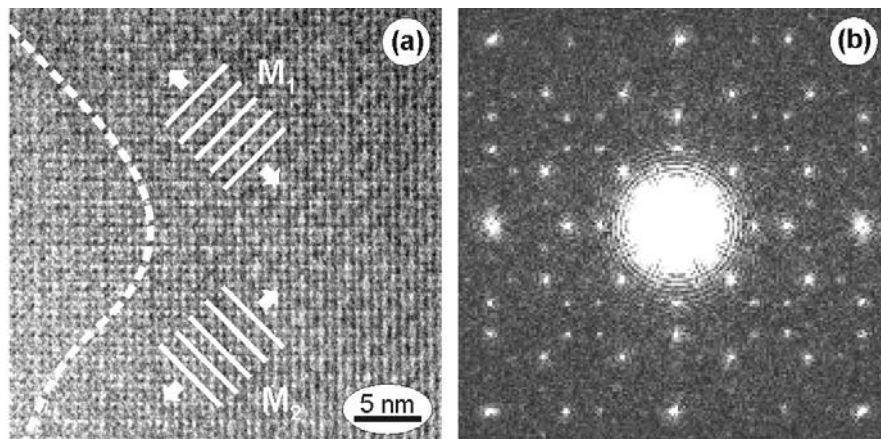


Fig.4.4.10 a) High-resolution TEM micrograph taken along [001] of extended two-dimensionally modulated superdomains at $x = 0.1$ (M_1 and M_2 denote the two modulation waves); b) Fourier power spectrum of the image in a) revealing up to second order satellite spots.

In Fig.4.4.10 the two-dimensional incommensurate modulation of $\text{Ca}_2\text{Co}_{0.9}\text{Zn}_{0.1}\text{Si}_2\text{O}_7$ is revealed in a transmission electron micrograph taken along the [001] direction (Fig.4.4.10a), and in the power spectrum of the image (Fig.4.4.10b). The direction and period of the two modulation waves M_1 and M_2 indicated in Fig.4.4.10a are almost equally detected through extended crystal areas with only slight variations in contrast. Correspondingly, superdomain formations with sizes larger than 30 nm were found in the low Zn-content crystals. In accordance with this, the main reflections and the satellite spots in the power spectrum (Fig.4.4.10b) appear as sharp small dots without considerable amounts of diffuse scattering contributions. Satellites up to second order are displayed characterizing the crystal as high order incommensurate phase (comparing Fig.4.4.9).

Electron microscope studies of the incommensurate modulation of melilites are usually restricted to the (001) projection; an example of the projection onto the (100) plane is found in the work of van Heurck et al. ^[28]. The a -axis view shown in Fig.4.4.11a of the Co end-member from our sample series reveals undulated vertical stripes with an average spacing of $\sim 8\text{\AA}$, approximately equal the a -axis lattice constant. Clear expression of the modulation pattern is provided by electron

diffraction: The visible satellite reflections in Fig.4.4.11b (the reciprocal unit cell viewed along [100] is marked by a black line) are due to combinations of the two modulation vectors \mathbf{q}_1 and \mathbf{q}_2 with $m \times n = \pm 1$ and are, therefore, very closely spaced on \mathbf{a}^* . They give rise to an averaged image contrast that overlies the regular (100) lattice image. This superposition is supposed to be the reason for the formation of the wavy stripes in the lattice image in Fig.4.4.11a.

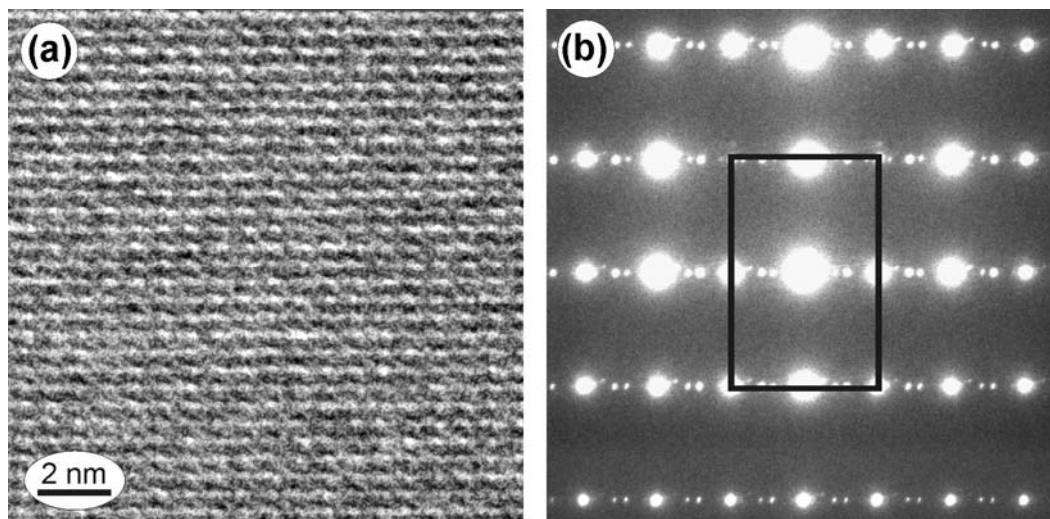


Fig.4.4.11 a) TEM micrograph and b) selected area electron diffraction pattern along the [100] zone axis of $\text{Ca}_2\text{CoSi}_2\text{O}_7$. The wavy stripes parallel c in the image are due to overlapping of the lattice planes and the modulation pattern formed by the combination $\pm (\mathbf{q}_1\mathbf{q}_2)$ of the two modulation vectors. The reciprocal unit cell is drawn in b).

The structural picture changes when the Zn-content in $\text{Ca}_2\text{Co}_{1-x}\text{Zn}_x\text{Si}_2\text{O}_7$ is increased up to $x = 0.5$ and higher. In the high-resolution image in Fig.4.4.12a, variations in the modulated structure pattern are discernible which are reflected in the Fourier power spectrum of the image in Fig.4.4.12b showing substantial diffuse scattering intensity located on arcs connecting the first order satellites. Its successful detection strongly depends on the appropriate specimen thickness. The circular diffuse intensity patterns formed around the main reflections of the tetragonal lattice at radius $|\mathbf{q}|$ are evidence of a short-range ordering scheme of the two-dimensional modulation pattern.

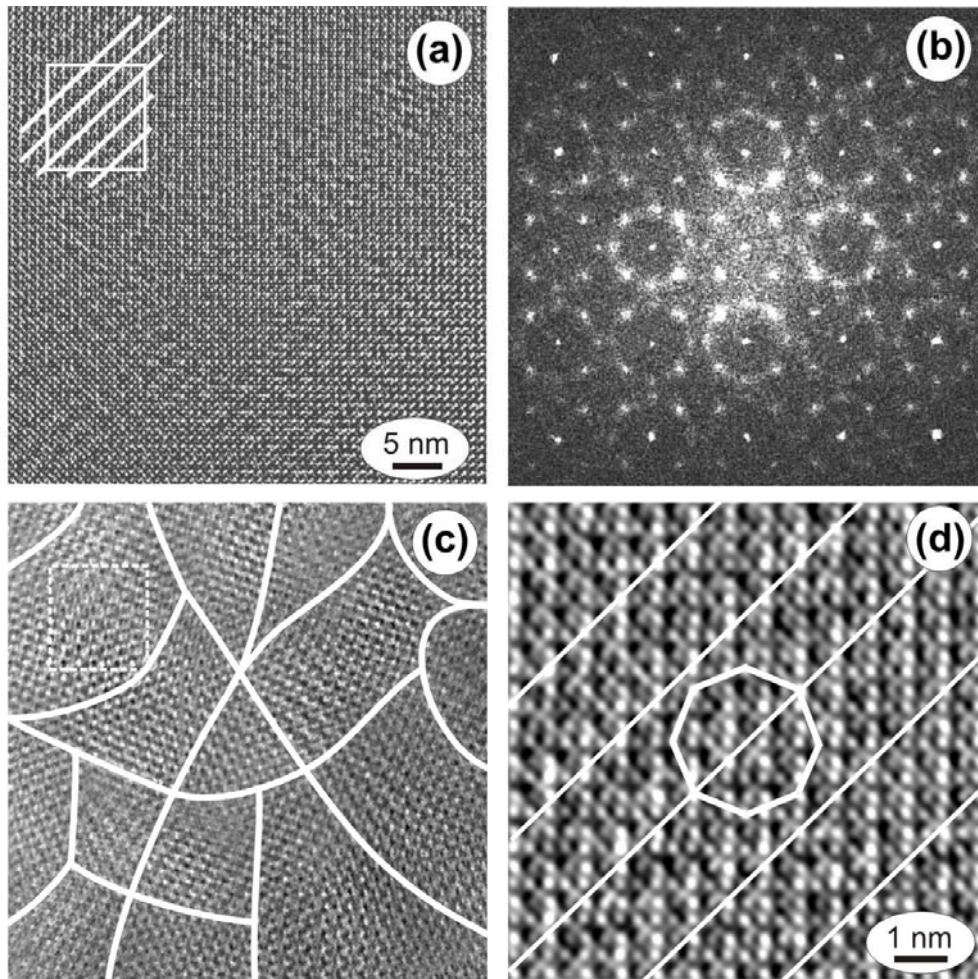


Fig.4.4.12 a) TEM image of $\text{Ca}_2\text{Co}_{0.5}\text{Zn}_{0.5}\text{Si}_2\text{O}_7$ taken along the [001] direction; b) corresponding Fourier power spectrum; c) filtered inverse Fourier transform clearly revealing the varying modulation pattern and arrangement of superdomains (domain boundary traces indicated); d) high-resolution close-up of the area marked in a) and c) with a few modulation periods and an octagonal cluster therein indicated.

The ordering is established in form of a complex arrangement of small superdomains which can be seen only weakly in Fig.4.4.12a, but become developed by appropriate filtering and processing of the Fourier transform as shown in Fig.4.4.12c. The modulation pattern varies from area to area in its propagation direction, phase of modulation wave and spatial coherency extent, thereby creating irregular domains of sizes typically < 30 nm, on average. From a number of observations it is suggested that the intensity of the diffuse scattering has its maximum around $x = 0.5$ and decreases towards larger values of x . This behavior is indicative of a contribution by occupational ordering of Co and Zn species to the overall displacive modulation and ordering.

Diffuse scattering due to short-range ordering within a many-domain structure that has been observed here in dependence on compositional variations, also occurs when the temperature changes. It is typically an intermediate state in phase transitional processes as will be shown in a forthcoming subpart.

Fig.4.4.12d is a close-up of the area framed in Fig.4.4.12a showing the modulation pattern at atomic resolution. Several modulation periods are indicated along with the octagonal arrangement of bright intensity dots that mark a typical cluster formation of T^j tetrahedra. Such a clustering was predicted by van Heurck et al. [28], Riester et al. [16], Kusaka et al. [19], and Hagya et al. [56]. According to these models the misfit-induced strains cause changes of the Ca-O bonding resulting in a reduction of the calcium-to-oxygen coordination from eight- to six-fold for different sections through the superspace. Internal stress release is the driving force for the modulation formation. It is realized on both a nanoscopic as well as microscopic scale by octagonal clustering of the low-coordinated calcium polyhedra as well as by the introduction of a network of domain boundaries.

4.4.4 The transition from the incommensurate phase to the commensurate lock-in phase and to the normal phase

The incommensurate - commensurate phase transition

With changing temperature, the process of the phase transition from the incommensurate to the commensurate lock-in state could be revealed from the positional shift of the satellite reflections. Fig.4.4.13 shows the electron diffraction patterns of $\text{Ca}_2\text{Co}_{0.9}\text{Zn}_{0.1}\text{Si}_2\text{O}_7$ taken after cooling down to different temperatures for 1h.

At 297K an incommensurate structure exists (Fig.4.4.13a). The satellite reflections up to second order can be observed clearly as marked by numbers. Upon cooling down to 168K, evident diffuse scattering of satellites was observed (Fig.4.4.13b). Satellites tended to shift closely each other along $[110]$ or $[1\bar{1}0]$ as indicated by arrows. Finally, the commensurate lock-in structure was formed as shown in the EDP taken at 91K (Fig.4.4.13c).

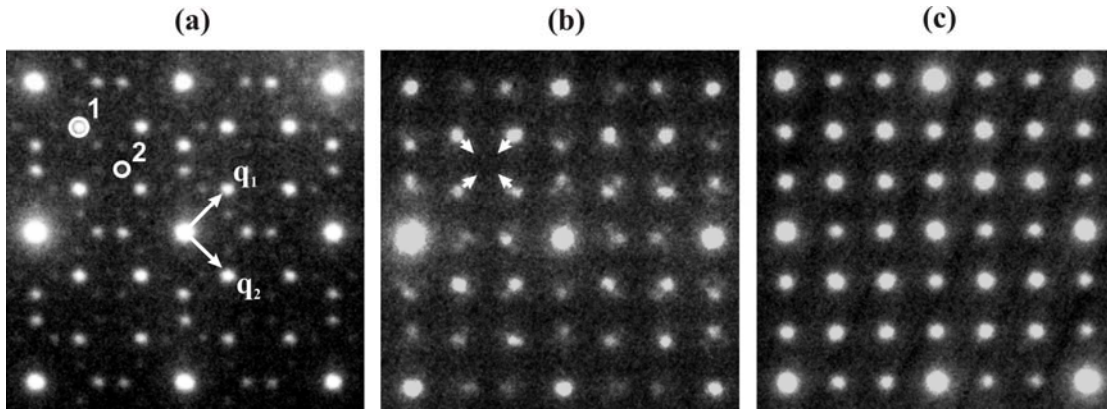


Fig.4.4.13 Electron diffraction patterns of $\text{Ca}_2\text{Co}_{0.9}\text{Zn}_{0.1}\text{Si}_2\text{O}_7$ depending on temperature. a) Incommensurately modulated structure at 297K; b) diffuse scattering around Bragg reflections indicating the occurrence of the phase transition from the incommensurate to the commensurate lock-in phase at 168K; c) the commensurate lock-in structure at 91K.

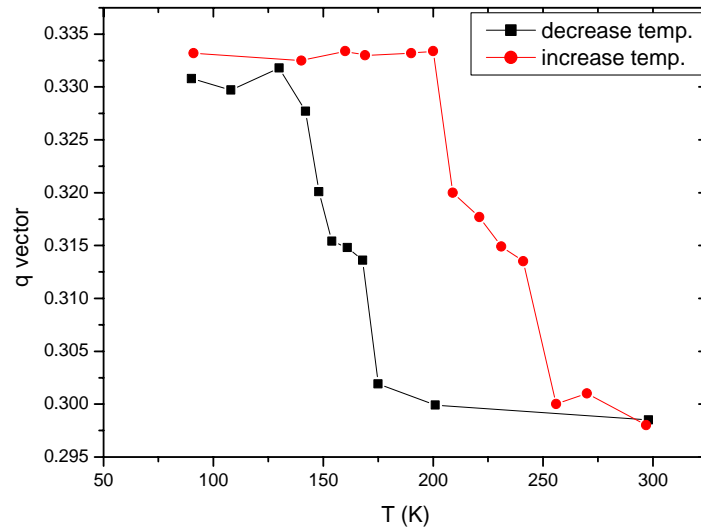


Fig.4.4.14 The q -value as a function of temperature for the $\text{Ca}_2\text{Co}_{0.9}\text{Zn}_{0.1}\text{Si}_2\text{O}_7$ crystal calculated from the corresponding EDPs. The sharp increase of the q -value between 175K and 130K indicated the phase transition occurred.

The change of the modulation vector with temperature calculated from EDPs is shown in the diagram Fig.4.4.14. In order to reach thermal equilibration of the structure, every EDP was taken after the temperature remained unchanged for 1h. With the lowering of temperature from 300K to 91K, the q -vector is related linearly to temperature within the intermediate incommensurate phase, and then jumps to 0.331 at about 130K. After that, it remains constant. The jumping of the modulation wave vector between 175K and 130K indicates the phase transition from the

incommensurate to the commensurate lock-in phase. The q value with varying temperature from 90K to 300K is also given in Fig.4.4.14. It begins to decrease rapidly after 200K. A strong hysteresis exists between the cooling and heating run of the *in situ* experiments.

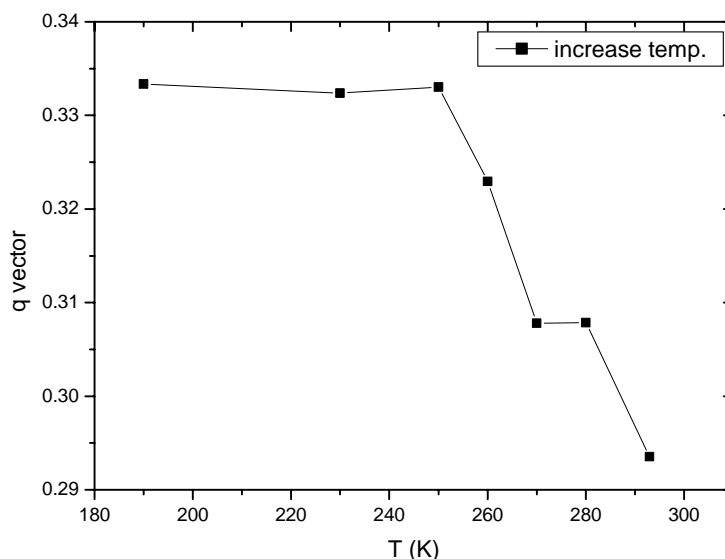


Fig.4.4.15 The q -value as a function of temperature for the $\text{Ca}_2\text{Co}_{0.9}\text{Zn}_{0.1}\text{Si}_2\text{O}_7$ crystal was investigated by single crystal X-ray diffraction. The measurements conformed to the ascending temperature sequence.

For comparison, the structural variation of the same crystal with temperature at cooling from 300K to 90K was also investigated by X-ray diffraction (Most XRD measurements and all refinements mentioned later were carried out by Prof. Werner Massa, Chemistry Department). The results in Fig.4.4.15 show the same tendency of the q -value as observed from the EDPs. However, the transformation point from the commensurate to the incommensurate phase measured by X-ray diffraction was about 250K which is higher than 200K measured by EDPs. This difference can be explained by the differently measured range. The measured area in electron diffraction is in the order of nanometer. As it is discussed in the following, domains in the order of nanometer are formed during the phase transition and the point of the phase transition is different from one domain to another. The q -value obtained from the electron diffraction represents very local structural information of the crystal. On the contrary, the measurement of X-ray diffraction is related to millimeter scale and, thus, gives more average information. Another possible reason is due to the influence of the

electron beam irradiation in the microscope. The formation of domains described later are considered responsible for the phenomenon of the prominent hysteresis observed by X-ray diffraction ^[29] and in our experiments.

The phase transition into the commensurate lock-in phase was found to occur up to x -values < 0.5 at liquid nitrogen (LN_2) temperature. Considering the plenty of EDPs taken from different areas under the phase transition temperature, it was found that the process of the phase transition is rather slow and also uneven from place to place. Some areas started the phase transition firstly, but other areas not yet even at much lower temperature. This is proved by Fig.4.4.16, where quite different diffraction patterns from different areas of the same sample at 126K represent the incommensurate phase (Fig.4.4.16a) and an almost commensurate lock-in phase (Fig.4.4.16b). The quite different domain formations result in the hysteresis phenomenon described above.

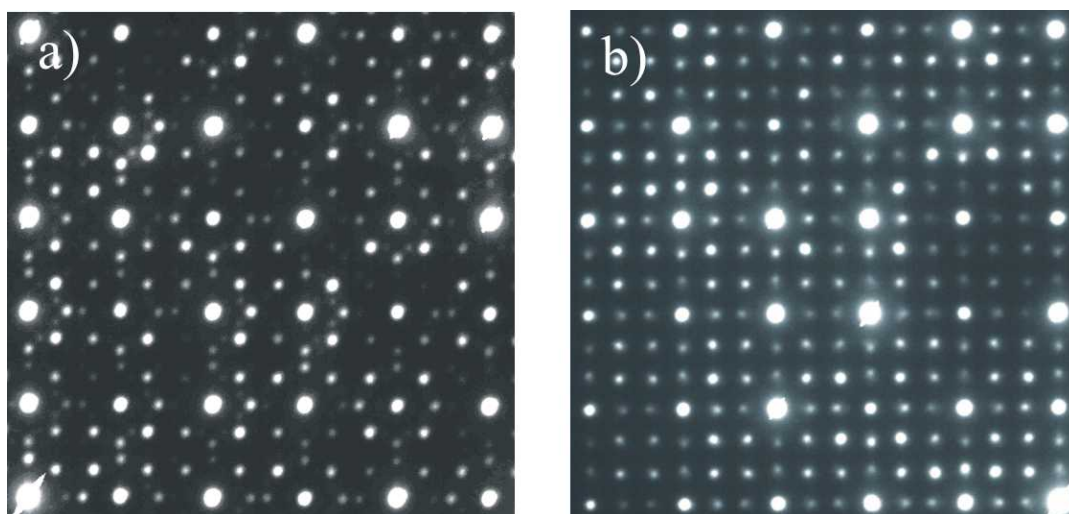


Fig.4.4.16 The EDPs of $\text{Ca}_2\text{Co}_{0.9}\text{Zn}_{0.1}\text{Si}_2\text{O}_7$ crystal taken from different areas at 126K, indicating that incommensurate and commensurate domains exist in parallel.

Microdomains and discommensurations

Fig.4.4.17 shows a domain structure and its evolution in $\text{Ca}_2\text{CoSi}_2\text{O}_7$ with prolonging cooling time and lowering temperature. Many domains separated by the intersection of discommensuration (DC) walls are formed at the beginning of the phase transition (Fig.4.4.17a). The size of the majority of the domains was about 10nm. With further cooling and proceeding time the domains increased in size

(Fig.4.4.17b-d) and finally developed into a random network structure (Fig.4.4.17e). Lowering the temperature accelerated the increase of the domains in size.

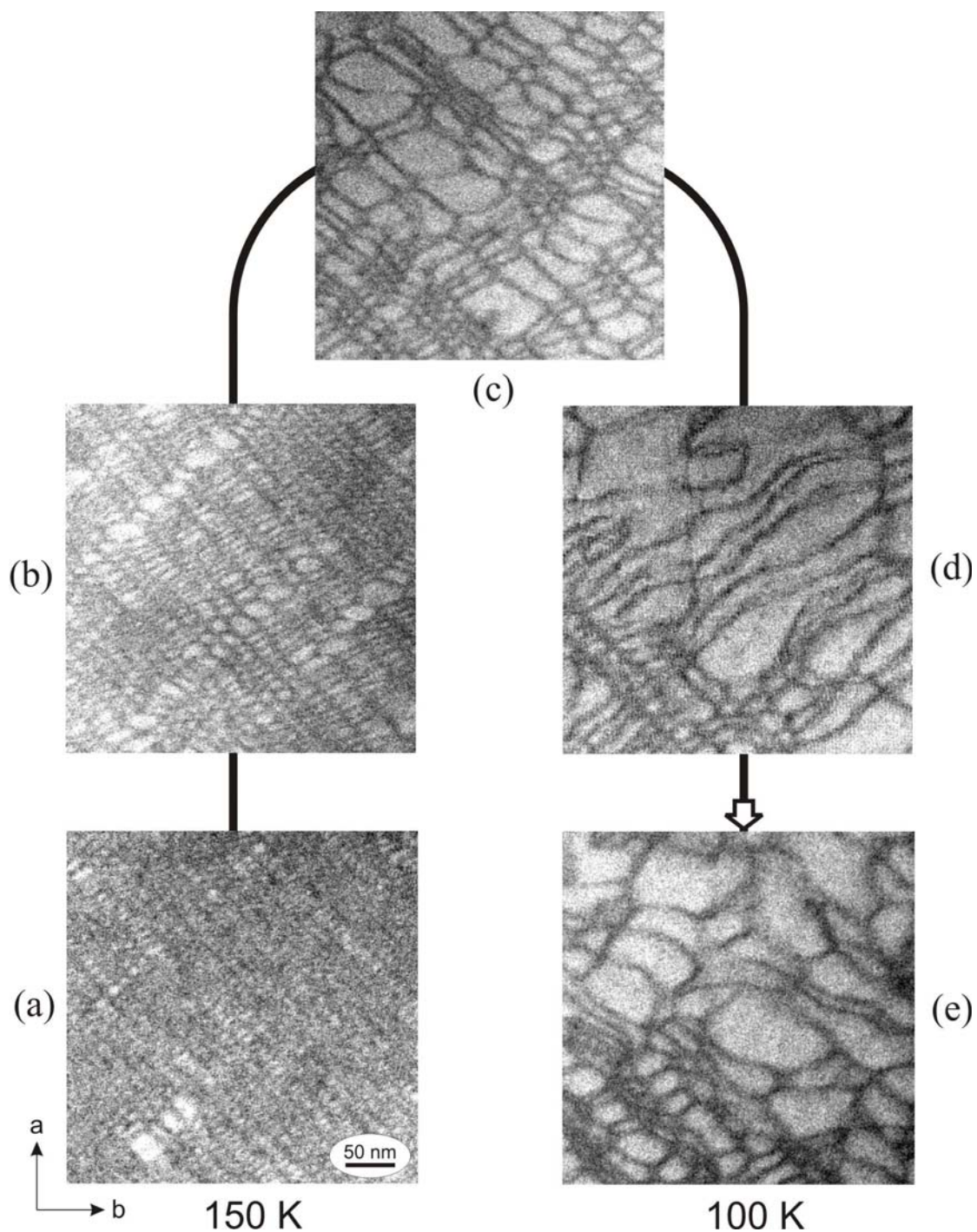


Fig.4.4.17 Bright-field electron micrographs taken during the phase transition showing microdomains and the changes of the domains and the discommensuration network with time at decreasing temperature: (a) $t_1 = 50\text{min}$ at 150K ; (b) $t_2 = t_1 + 30\text{min}$ at 100K ; (c) $t_3 = t_2 + 30\text{min}$; (d) $t_4 = t_3 + 40\text{min}$; (e) $t_5 = t_4 + 50\text{min}$.

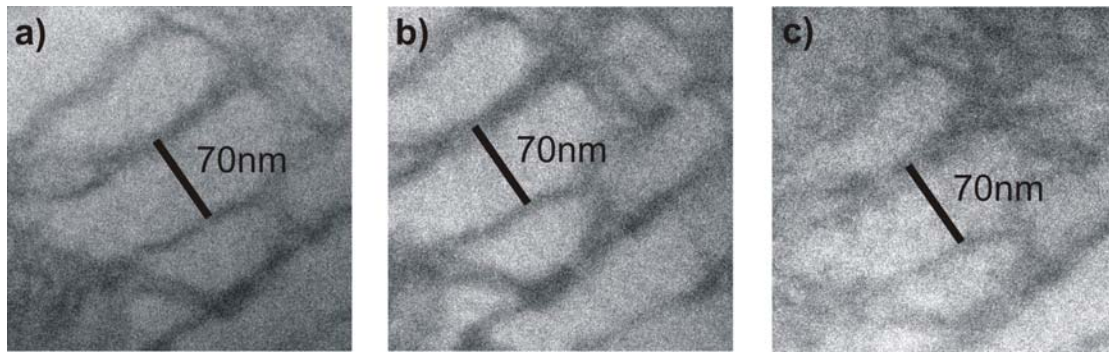


Fig.4.4.18 Microdomain in $\text{Ca}_2\text{CoSi}_2\text{O}_7$ taken at 130K in other area after cooling different time. a) 240 min; b) 300 min; c) 360 min.

Fig.4.4.18 shows some domains of $\text{Ca}_2\text{CoSi}_2\text{O}_7$ observed in the same specimen area at 130K after different cooling times. As indicated in the images, the width of one domain was about 70 nm and kept the same in size and shape during cooling for 240 min up to 360 min, which means that the area almost reached the commensurate lock-in phase.

Comparable TEM measurements under liquid He condition are shown in Fig.4.4.19. Even at He temperature, the uncompleted commensurate lock-in phase could still be observed (Fig.4.4.19a) ^[57]. A high-resolution image taken at this temperature shows two dimensional modulations assigned as M_1 and M_2 (Fig.4.4.19b).

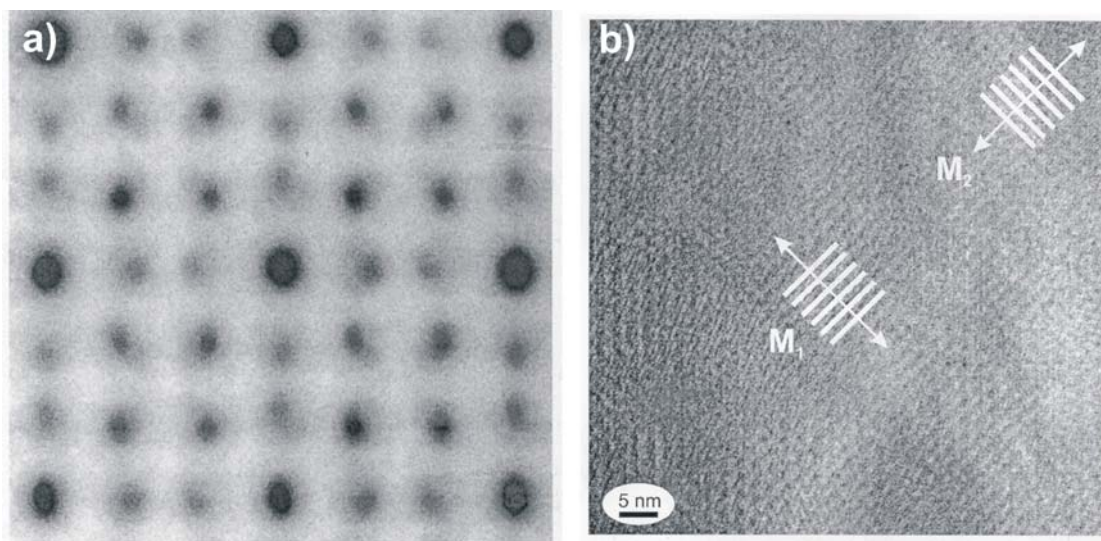


Fig.4.4.19 Electron diffraction pattern (a) and high-resolution image (b) of $\text{Ca}_2\text{CoSi}_2\text{O}_7$ taken at liquid He temperature. M_1 and M_2 assign to two-dimensional modulated directions.

In fact, despite various cooling regimes applied to reach an equilibrium situation always DC walls could be detected. This finding is in close correspondence with the results of electron (Fig.4.4.19a) and X-ray diffraction ^[29] investigations according to which in no case a complete transformation of the crystal into the final commensurate lock-in phase was reached. In the commensurate phase there should be no discommensurations (DCs) in the lowest-energy state ^[58].

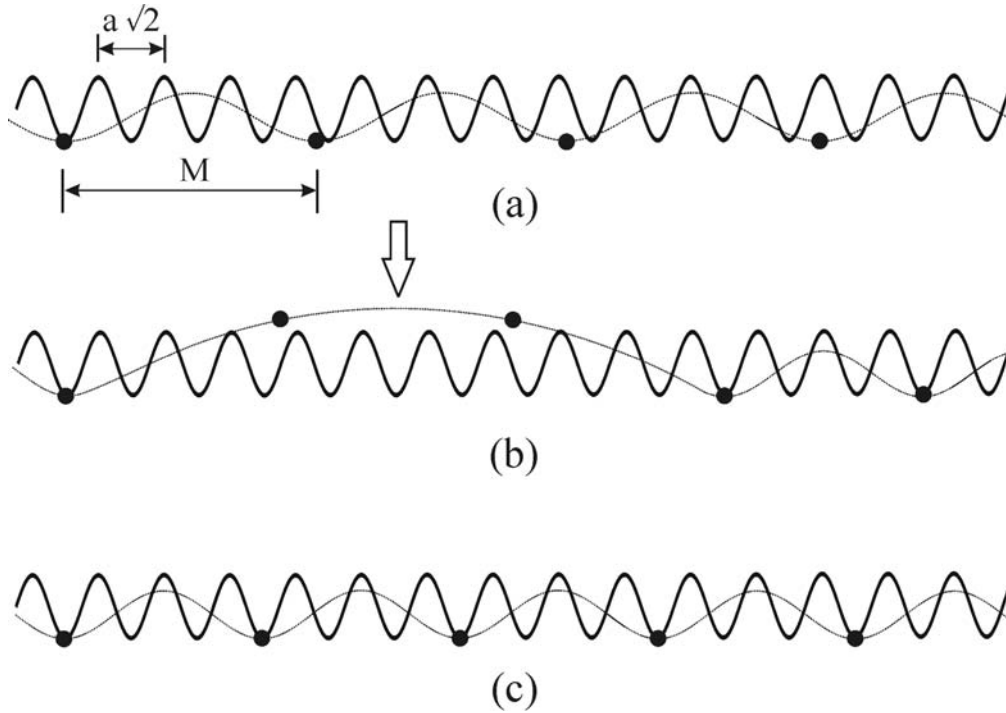


Fig.4.4.20 One-dimensional model of successive stages in the incommensurate-to-commensurate transition. (a) incommensurate structure ($3/2 a\sqrt{2} < M < 2a\sqrt{2}$), (b) positive DC separating commensurate domains; (c) commensurate structure ($M = 3/2 a\sqrt{2}$).

In the course of the phase transformational process, the alignment of the DCs parallel $\{110\}$ is successively lost and a more irregular network is formed with the enclosed commensurate domains growing in size. The *in situ* observations suggest that the incommensurate-to-commensurate transition is initiated at a large number of nucleation sites densely distributed over the whole crystal area. The process in the phase transformation and the nature of DCs is schematically depicted in Fig.4.4.20. Fig.4.4.20a illustrates a one-dimensionally modulated structure completely incommensurate with the basic crystal lattice, i.e. possessing a wavelength M that is an irrational multiple of the lattice spacing $|a + b|$ along the $\langle 110 \rangle$ direction.

Approaching the phase transitional temperature region, the rearrangement and dense packing on the nanometer level of the structural units under the influence of increasing misfit stress leads to the nucleation of commensurate ‘islands’ within the incommensurate phase (Fig.4.4.20b). The commensurate kernels grow on the expense of the number (and of the width) of the incommensurate walls (Fig.4.4.20c), which adopt the character of narrow boundaries: these boundaries we call discommensurations. In this view, the DCs represent regions where the developing commensurate registry between the basic lattice and the modulation wave is broken [59]

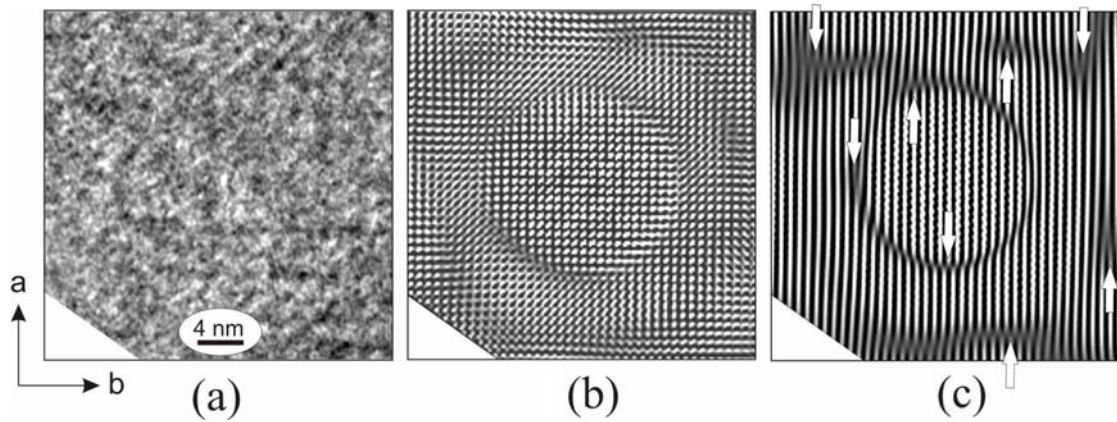


Fig.4.4.21 Discommensuration loop observed at 130K. (a) original image; (b) Fourier-filtered image using the eight basic orthorhombic reflections; (c) Fourier-filtered two-beam (± 100) lattice fringe image with dislocation-like defects arrowed.

Within the above-described two-dimensionally extended networks special configurations of the DCs were observed, such as those in Fig.4.4.21. The relevant information is selected by Fourier-filtering of the original high-resolution micrograph (Fig.4.4.21a) using the eight basic nearest $\{hk0\}$ reflections of the orthorhombic lattice (Fig.4.4.21b), or the two (± 100) spots only (Fig.4.4.20c). Fig.4.4.21c is synonymous with a symmetrical two-beam lattice fringe image. What cannot be seen in the original unprocessed image is revealed in Fig.4.4.21b: the central area of the image contains an almost circularly shaped domain with very homogeneous structure, enclosed by a DC boundary loop. Relics of a tetragonal mesh built-up by orthogonally intersecting DCs surround the loop. Fig.4.4.21c clearly displays a lattice shift across the DC constituting the loop as well as DCs separating other domains parts in the surrounding crystal. This shift is usually connected with the presence of dislocation-

like defects as they are pointed out by arrows. Such a shift of the lattice fringes alongside a discommensuration was detected also in other materials, e.g., by Jiang and Zou [60]. However, the actual situation in the present case is more complicated than it is shown in Fig.4.4.21c where only one crystal orientation has been filtered out for clarity.

The formation of loops clearly indicates the tendency of the DCs to adopt low-energy configurations. Quite a similar behavior is well known from dislocation type defects [61, 62].

The incommensurate - normal phase transition

The phase transition of $\text{Ca}_2\text{Co}_{1-x}\text{Zn}_x\text{Si}_2\text{O}_7$ from the incommensurate to the normal state was investigated by DSC between 350K and 500K and the results are shown in Fig.4.4.22. The T_{I-N} of Co and Zn end members are 478K and 390K, respectively, similar to the results of R othlisberger et al. [7]. T_{I-N} shifts to lower temperature with increasing Zn content and the peaks become broader. The heating and cooling investigations revealed the peak of the heat capacity at the same temperature, which indicates no hysteresis between the incommensurate and the normal phase transition.

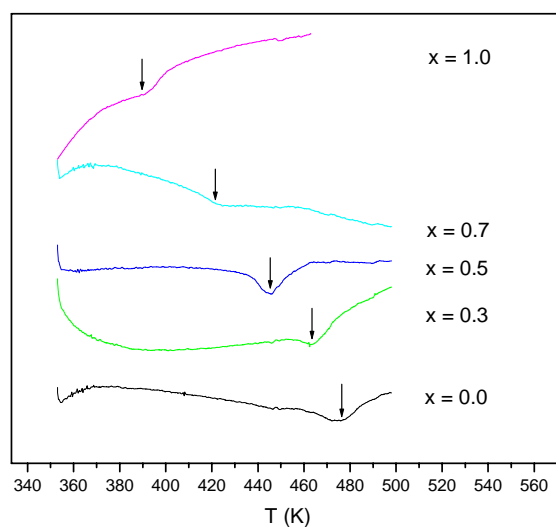


Fig.4.4.22 Temperature dependence of the heat capacity of $\text{Ca}_2\text{Co}_{1-x}\text{Zn}_x\text{Si}_2\text{O}_7$ compounds. The endothermic peak as indicated by arrow appears during the phase transition from the incommensurate to the normal structure.

4 Results and discussions

Table 4.4.3 T_{I-N} and T_{I-C} obtained through the measurements of the heat capacity of $\text{Ca}_2\text{Co}_{1-x}\text{Zn}_x\text{Si}_2\text{O}_7$ solid solutions.

Zn/(Co+Zn)	T_{I-N} (K)	T_{I-C} (K)
0.0	478	153.7
0.1	477.7	146.5-165
0.3	463.6	145.5-123
0.5	446.4	-
0.7	422.7	-
0.9	404	-
1.0	388-394	-

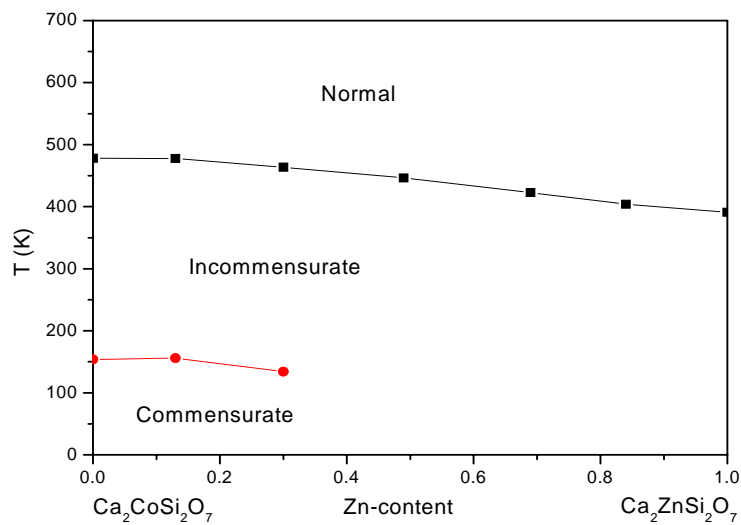


Fig.4.4.23 Phase diagram of $\text{Ca}_2\text{Co}_{1-x}\text{Zn}_x\text{Si}_2\text{O}_7$ system.

The temperature of the phase transition of the $\text{Ca}_2\text{Co}_{1-x}\text{Zn}_x\text{Si}_2\text{O}_7$ system as investigated by DSC are listed in Table 4.4.3 and plotted in Fig.4.4.23. The data about the I-C phase transition are included. The T_{I-N} values exhibit a linear decrease with increasing Zn content, similar to that in $\text{Ca}_2\text{Mg}_{1-x}\text{Zn}_x\text{Si}_2\text{O}_7$ solid solutions.

The hysteresis between the incommensurate and the commensurate phase transition was revealed, but no hysteresis existed between the incommensurate and the normal phase transitions.

4.4.5 Refinement of the commensurate lock-in structure of $\text{Ca}_2\text{Co}_{0.9}\text{Zn}_{0.1}\text{Si}_2\text{O}_7$

As indicated by the q -vector measured by X-ray diffraction the almost commensurate phase can be reached at liquid N_2 temperature, and reversed into the incommensurate phase at temperature higher than 250K. In the commensurate phase the satellite reflections are located on rational positions with respect to the main reflections in the reciprocal lattice. McConell^[63] derived by group theoretical methods $P\bar{4}$ and $P2_12_12$ as only suitable subgroups that are related to the modulation of the melilite structure. The space group $P\bar{4}$ was used for the description of the commensurate lock-in phase of $\text{Ca}_2\text{CoSi}_2\text{O}_7$ ^[16], but refinements as (110) twin could be held stable only by applying constraints in geometry for all SiO_4 groups and by using common isotropic displacement parameters. Based on the diffraction studies of $\text{Ca}_2\text{CoSi}_2\text{O}_7$ at low temperature, Hagiya et al.^[56] refined the same structure according to $P\bar{4}$ and $P2_12_12$ and found much better agreement of satellite intensities for the latter space group.

Based on our area detector data measured at 190K for $\text{Ca}_2\text{Co}_{0.9}\text{Zn}_{0.1}\text{Si}_2\text{O}_7$ we performed refinements of both models and could clearly confirm the results of Hagiya. Though all atoms could be refined without any positional constraints in s.g. $P\bar{4}$, some of the displacement parameters became irregular. Even for the heavy Ca and Co atoms, refinement of anisotropic parameters became unstable, the residuals were $wR_2 = 19.4\%$ (all F^2) and $R = 7.56\%$ ($F > 2\sigma$). In s.g. $P2_12_12$ however, for all heavy atoms sensible anisotropic displacement parameters could be refined. Even for most of the O atoms good anisotropic displacement parameters could be refined, but for the final cycles isotropic parameters were used only in order to reduce the number of parameters. The crystal structure has been refined in the orthorhombic space group $P2_12_12$ as (110)-twin with a twin ratio of 46.5(3)%. The residuals were $wR_2 = 15.6\%$ (all F^2) and $R = 6.05\%$ ($F > 2\sigma$). The crystal data, structure refinement parameters and the interatomic distances are given in Appendix A. for s.g. $P2_12_12$ and in Appendix B. for s.g. $P\bar{4}$.

The mean Si-O distance of each tetrahedron ranges from 1.620(10) to 1.643(9)Å. The distance between the Si and O atoms bridging two Si tetrahedra forming a dimer is the longest Si-O distance and the bond length between Si and the apical O atom is

the shortest. Taking into account both bond length and bond angle five classes of Si tetrahedra exist in the 3×3 super unit.

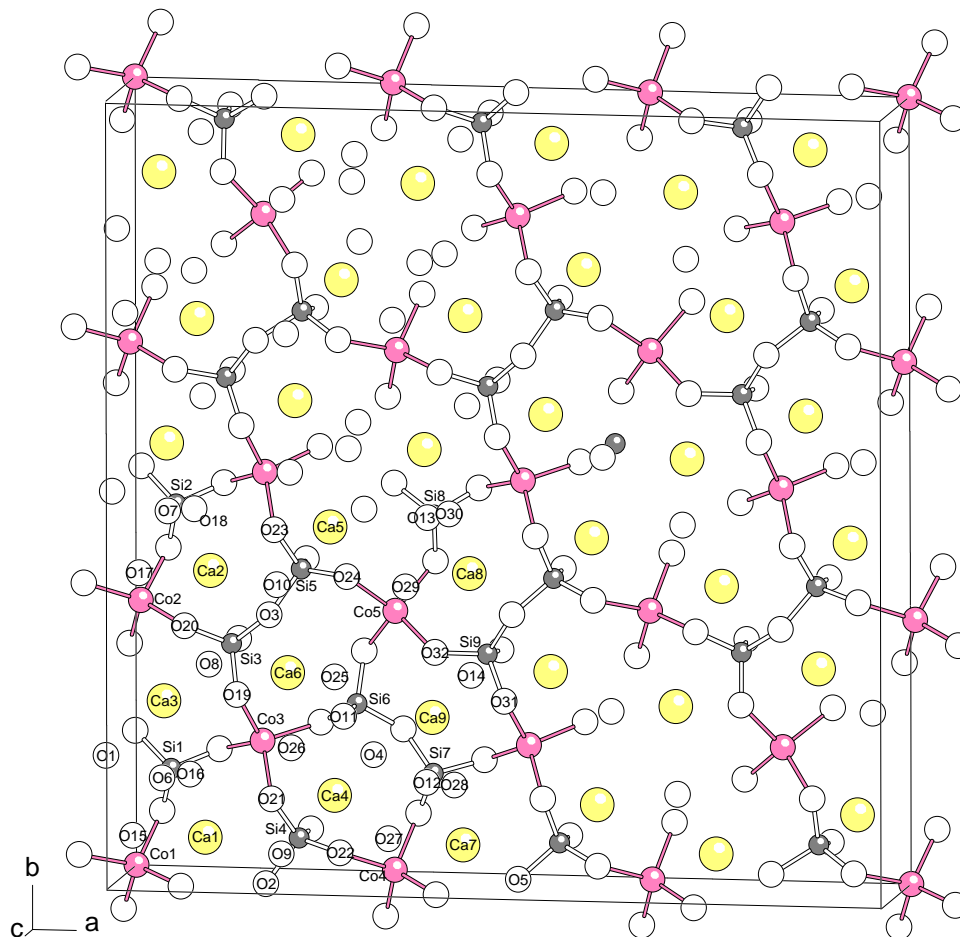


Fig.4.4.24 The commensurate lock-in structure of $\text{Ca}_2\text{Co}_{0.9}\text{Zn}_{0.1}\text{Si}_2\text{O}_7$ determined at 190K. Projection of a part of the structure from about $[001]$. All atoms of the asymmetric unit are labeled (same selection and labeling scheme as in Hagiya et al. 2001).

As known from the structural description of the average structure, Ca atoms are located between the tetrahedral layers and are surrounded by eight O atoms. In the 3×3 superstructure, the Ca-O distances of each polyhedron show wide variations (Fig.4.4.24). Based on a critical bond length of 2.6 \AA , the Ca polyhedra can be assigned to be of six-fold (Ca5, Ca6, Ca8, Ca9), of seven-fold (Ca2) and of eight-fold coordination (Ca1, Ca3, Ca4). The “bundles” of the six-fold coordinated Ca polyhedra were suggested to form octagonal arrangements ^[16, 18], which is thought to be responsible for the formation of the incommensurate phase.

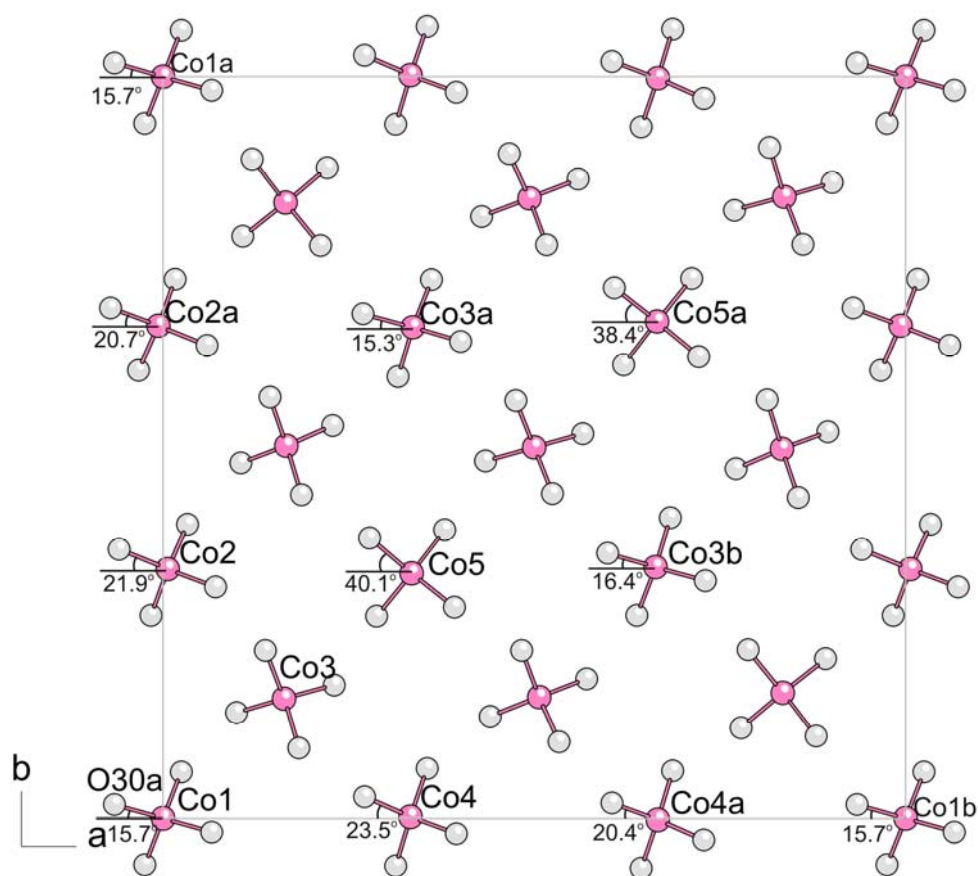


Fig.4.4.25 Projection of the T^1 tetrahedra of the commensurate lock-in structure of $\text{Ca}_2\text{Co}_{0.9}\text{Zn}_{0.1}\text{Si}_2\text{O}_7$ in [001]. T^1 sites actually occupied by Co and Zn. The angle formed by the Co-O bond and a axis is named as Co1, Co1a, Co2 and so on.

There are five independent Co(Zn) atoms in the 3×3 superstructure. The mean (Co,Zn)-O distances of $T^1\text{O}_4$ tetrahedra are in the range $1.945(9) - 1.958(9)\text{\AA}$, which is the same as obtained by Hagiya et al. ^[56] in $\text{Ca}_2\text{CoSi}_2\text{O}_7$. The substitution of a small amount of Zn for Co in the $T^1\text{O}_4$ tetrahedra has no evident effect on the T^1 -O bond because of the close ionic radius. Each tetrahedron shows a distortion and a rotation with different degree. Especially, the Co,Zn(5) tetrahedron is very much flattened along [001] and the two independent angles intersecting [001], 127.1° and 125.4° , are much larger than the regular tetrahedral angle of 109.47° . In comparison to the corresponding values in $\text{Ca}_2\text{CoSi}_2\text{O}_7$ ^[56], the substitution of Zn for Co makes the $T^1\text{O}_4$ tetrahedra to become more distorted. The rotation of $T^1\text{O}_4$ tetrahedra is evident and varies from one to another (Fig.4.4.25). The rotation angle between the a axis and one of the T^1 -O bonds of each tetrahedron projected on the (001) plane was determined

and marked in Fig.4.4.25. The angle varies from 15.3° for the Co,Zn (3a) tetrahedron to 40.1° for the Co,Zn (5) tetrahedron.

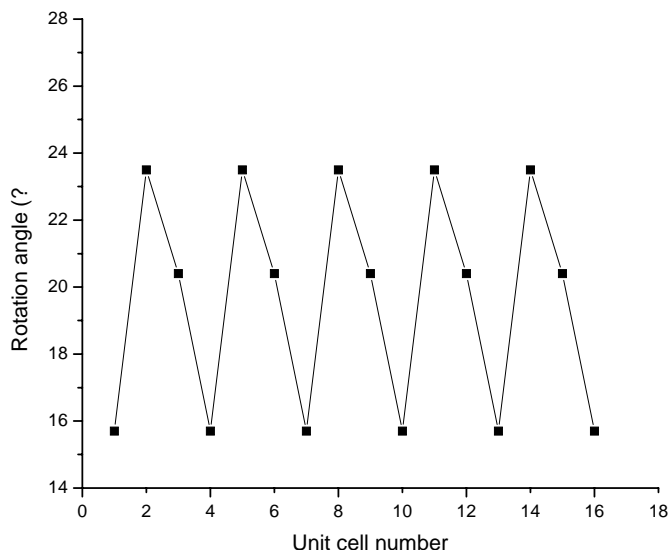


Fig.4.4.26 A saw-tooth-like ordering repeating according to the 3×3 superstructure. Each solid spot represents a T^1 -tetrahedron.

The octagonal distribution of the bundles formed by T^1 -tetrahedra and four six-fold Ca polyhedra, which characterizes the incommensurate structure ^[18, 37], is not found in the commensurate phase. The structural models in $P\bar{4}$ and $P2_12_12$ show different arrangement of “clusters” with 6-coordinated Ca. In the $P\bar{4}$ model of Riestler et al. ^[16] octagons can be seen. But the clusters are more dilute and show no octagons in the $P\bar{4}$ model of Hagiya and in the $P\bar{4}$ model used in this work. In the $P2_12_12$ model, there are no complete octagons only parts of it. Many fractions of the octagons are scattered in the structure. The commensurate modulation must be due to other reason. Considering the structural analysis from our experimental data the strong rotation of these tetrahedra as well as the tetrahedra distortion should contribute to the strain of tetrahedra sheet relative to the Ca polyhedra and regard as the main reason of the formation of the incommensurately modulated structure. In the commensurate lock-in phase a saw-tooth-like variation of Co,Zn-tetrahedra along a and b directions can be observed clearly, formed due to the different rotation of Co,Zn-tetrahedra. Fig.4.4.26 shows a saw-tooth-like variation in one dimension. The saw-tooth-like variation

repeats according to the 3×3 super unit, which was not observed in the incommensurate phase until now, is assumed as the equilibrium state of lowest energy. This periodic ordering along a and b directions, formed by the distortion and rotation of Co,Zn -tetrahedra, especially the rotation of Co,Zn -tetrahedra, causes the commensurate modulated structure with $q = 1/3$.

4.4.6 Conclusions

Single crystals of $\text{Ca}_2\text{Co}_{1-x}\text{Zn}_x\text{Si}_2\text{O}_7$ free of inclusions and bubbles could be obtained through precise control of the growing speed. Using a small melting length made it possible to efficiently avoid undesired evaporation of Zn during the growth process.

Two-dimensional incommensurate modulation of the $\text{Ca}_2\text{Co}_{1-x}\text{Zn}_x\text{Si}_2\text{O}_7$ structure was observed by electron diffraction and high-resolution imaging. Different ordering schemes within the modulated structure were observed, and changes of the domain morphology were found in dependence on the Co/Zn ratio. The diffuse diffraction intensity has been proved a clear indicator of short-range ordering associated with the incommensurate modulation. The octagonal arrangement of T^I tetrahedra surrounded by six-coordinated Ca atoms could be confirmed by HRTEM observations.

The phase transition process of $\text{Ca}_2\text{Co}_{0.9}\text{Zn}_{0.1}\text{Si}_2\text{O}_7$ does not occur homogeneously over extended crystal areas but is initiated at a great number of nucleation sites, and that the growing commensurate phase becomes separated by a network of straight DCs. In an early state of development the network resembles large-scale regular “bundles composed of four CaO_6 arrays and a central array of CaO_4 tetrahedra” as postulated in a recent simulation treatment by Kusaka et al. ^[64]. Progress in the very slow first order I-C transition process can be thus read, on a mesoscale, from the increasing separation of the DC lines. The equilibrium commensurate phase could be approached but not reached completely as the number of DCs show which survived even after prolonged and deep cooling. The T_{I-C} and T_{I-N} decreased slightly with increasing amount of Zn.

The commensurate lock-in structure is orthorhombic $P2_12_12$. The substitution of Zn for Co makes the $T^I\text{O}_4$ tetrahedra even more distorted. The distortion and rotation of

T^1 -tetrahedra is responsible for the commensurately modulated structure of $\text{Ca}_2\text{Co}_{0.9}\text{Zn}_{0.1}\text{Si}_2\text{O}_7$.

4.5 Investigations of the structural modulation of $(\text{Ca}_{1-x}\text{Sr}_x)_2\text{CoSi}_2\text{O}_7$

The temperature T_{I-N} at which the incommensurately modulated structure turns into the basic high-temperature structure depends on the chemical composition of the melilites. $\text{Ca}_2\text{CoSi}_2\text{O}_7$ with $T_{I-N} = 210\text{-}220^\circ\text{C}$ shows the incommensurate structure at room temperature, but $\text{Sr}_2\text{CoSi}_2\text{O}_7$ with $T_{I-N} \ll 24^\circ\text{C}$ shows the basic structure at room temperature^[7]. The shift of T_{I-N} with the substitution of Sr for Ca is interesting and helpful to understand the strain release by enlarging the cell. This chapter describes the single crystal growth of $(\text{Ca}_{1-x}\text{Sr}_x)_2\text{CoSi}_2\text{O}_7$. The chemical analyses were carried out by EDS and WDS. The structural variation caused by the substitution of Sr for Ca in $(\text{Ca}_{1-x}\text{Sr}_x)_2\text{CoSi}_2\text{O}_7$ was investigated by TEM and XRD methods. Measurements were carried out to determine the magnetic behavior of the material.

4.5.1 Crystal characterization

To obtain a crystal with a certain composition synthetic Ca- and Sr-end member melilites were proportionally mixed and prepared into the nutrient rods for crystal growth. The crystal growth of this system is comparatively easy because all raw materials used are stable at high temperature. Comparing with the $(\text{Ca}_{1-x}\text{Sr}_x)_2\text{MgSi}_2\text{O}_7$ solid solutions, which were grown in the range $x \leq 0.32$ using the Czochralski technique^[9], high-quality single crystals of $(\text{Ca}_{1-x}\text{Sr}_x)_2\text{CoSi}_2\text{O}_7$ in the whole range of x were grown in air from the melt using the FZ method.

Diameter and length of the growing crystal can be adjusted by controlling the moving speeds of the upper and lower shaft and the length of the nutrient rod. Single crystals of *ca.* 3mm diameter and *ca.* 20mm length were obtained shown in Fig.4.5.1. The crystals are dark blue. The observation of a smooth surface and the characterization by polarized optical microscopy confirmed that the crystals are of good quality i.e. free of bubbles, cracks and inclusions. The numbered areas (see figure caption) of the bulk crystal were used for different investigations.

The good agreement of the observed and calculated diffraction peaks confirms the pure phase. From all crystals EDS chemical analyses were performed. The measurements were carried out in different areas of each sample. The mean values are listed in Table 4.5.1. They are rather close to the nominal ones.

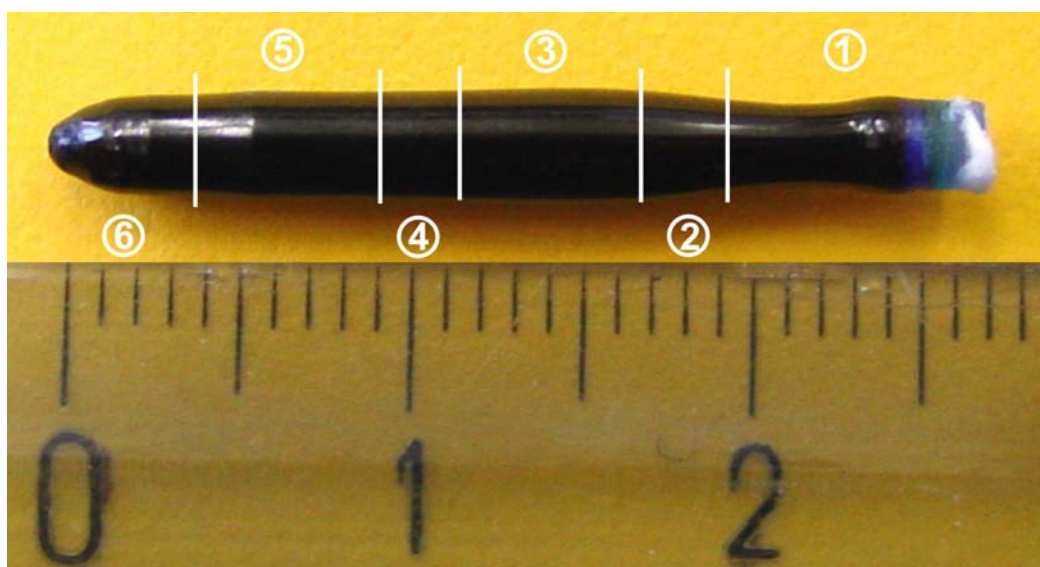


Fig.4.5.1 The as-grown crystal of $(\text{Ca}_{0.75}\text{Sr}_{0.25})_2\text{CoSi}_2\text{O}_7$. The length and the diameter of the crystal are 23mm and 3mm, respectively. The areas marked by numbers were used for a variety of measurements. (1) as seed crystal for other growth; (2) for single crystal X-ray diffraction; (3) for TEM; (4) for compositional analysis by EDS and WDS; (5) for magnetic measurements; (6) for phase identification by X-ray powder diffraction.

Table 4.5.1 The chemical analysis of $(\text{Ca}_{1-x}\text{Sr}_x)_2\text{CoSi}_2\text{O}_7$ by EDS

Nominal x	Measured x	Analyzed formula
0.00	0.00	$\text{Ca}_{1.98}\text{Co}_{0.98}\text{Si}_{2.04}\text{O}_7$
0.10	0.10	$(\text{Ca}_{0.90}\text{Sr}_{0.10})_2\text{Co}_{0.98}\text{Si}_{2.06}\text{O}_7$
0.12	0.11	$(\text{Ca}_{0.89}\text{Sr}_{0.11})_2\text{Co}_{0.96}\text{Si}_{2.13}\text{O}_7$
0.25	0.25	$(\text{Ca}_{0.75}\text{Sr}_{0.25})_2\text{Co}_{0.98}\text{Si}_{2.08}\text{O}_7$
0.30	0.30	$(\text{Ca}_{0.70}\text{Sr}_{0.30})_2\text{Co}_{0.96}\text{Si}_{2.09}\text{O}_7$
0.35	0.36	$(\text{Ca}_{0.64}\text{Sr}_{0.36})_2\text{Co}_{0.96}\text{Si}_{2.27}\text{O}_7$
0.50	0.57	$(\text{Ca}_{0.43}\text{Sr}_{0.57})_2\text{Co}_{0.96}\text{Si}_{2.23}\text{O}_7$
0.75	0.71	$(\text{Ca}_{0.29}\text{Sr}_{0.71})_2\text{Co}_{0.83}\text{Si}_{2.04}\text{O}_7$

The crystal $(\text{Ca}_{0.75}\text{Sr}_{0.25})_2\text{CoSi}_2\text{O}_7$ was also investigated by WDS technique for comparison. The diameter of the beam selected was $10\mu\text{m}$ and 30 points along both x and y were selected for analysis. The weight percent of each element as oxide shows an almost straight line along the points (Fig.4.5.2), which means that the constituent elements are homogeneously distributed in the bulk crystal. The content of Sr and Ca is the same as the nominal concentration.

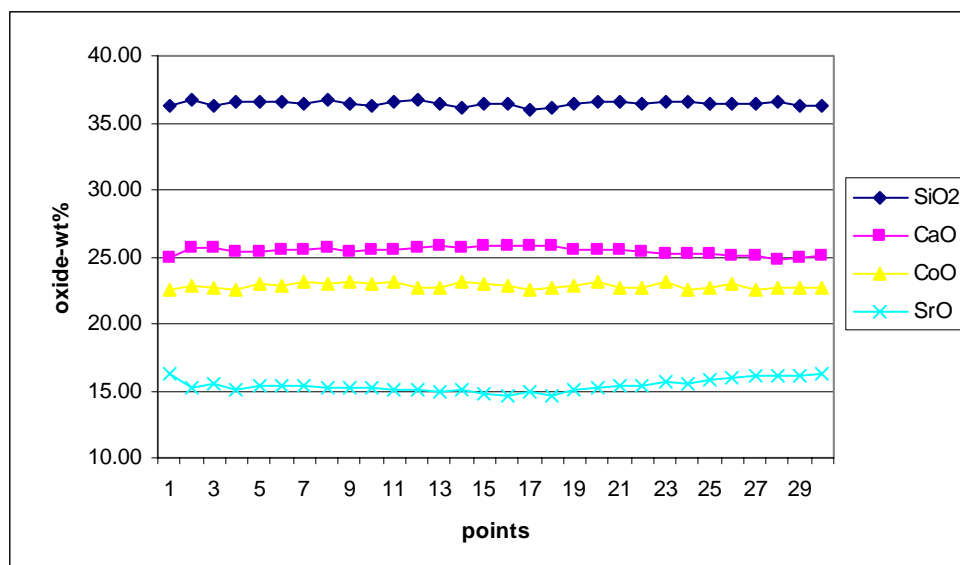


Fig.4.5.2 The correlation of the weight percent of each element as oxide with the measured spots by WDS.

Cell parameters of $(\text{Ca}_{0.75}\text{Sr}_{0.25})_2\text{CoSi}_2\text{O}_7$ were determined using the intense reflections in the range of $3.65 \leq \theta \leq 29.15$ at 233K. The basic structure was refined only using the main reflections. The refinement in the non-centrosymmetric space group $P\bar{4}2_1m$ by the least-squares program SHELXL-97, using 438 independent main reflections, led to $R(F) = 0.0207$ and $wR(F) = 0.0519$. Details of the experiment and the refinement are summarized in Table 4.5.2.

The basic structure of $(\text{Ca}_{0.75}\text{Sr}_{0.25})_2\text{CoSi}_2\text{O}_7$ determined at 233K is depicted in Fig.4.5.3. The structural features are similar to those of $(\text{Ca}_{0.87}\text{Sr}_{0.13})_2\text{CoSi}_2\text{O}_7$ [12, 15] and $\text{Ca}_2\text{CoSi}_2\text{O}_7$ [12]. The structure is characterized by a strong anisotropy of the displacement ellipsoid of all O and Ca/Sr atoms which lie almost in the (001) plane and the long axes of the ellipsoids are oriented toward the $\langle 110 \rangle$ direction except the axis of O(3). The ellipsoids of Co and Si are almost spherical. O(1) bridging the two tetrahedra in the Si_2O_7 dimer shows the largest anisotropy. The shift of O(1) towards the center of the channels should be coupled with the displacement of the Ca/Sr atoms located in the channels, because the displacement directions of Ca/Sr and O(1) atoms are mutually perpendicular. The anomalously large displacement feature in the average structure probably reflects the amplitudes of the displacive modulation and the occupational disorder due to the substitution of Ca by Sr.

4 Results and discussions

Table 4.5.2. Crystal data and main structure refinement for $(\text{Ca}_{0.75}\text{Sr}_{0.25})_2\text{CoSi}_2\text{O}_7$ at 233 K

Empirical formula	$\text{Ca}_{1.57}\text{Sr}_{0.43}\text{CoSi}_2\text{O}_7$	
Formula weight	327.71	
Temperature	233(2) K	
Wavelength	0.71073 Å	
Crystal system	tetragonal	
Space group	$P\bar{4}2_1m$	
Unit cell dimensions	$a = 7.8912(9)$ Å	$\alpha = 90^\circ$.
	$b = 7.8912(9)$ Å	$\beta = 90^\circ$.
	$c = 5.0461(6)$ Å	$\gamma = 90^\circ$.
Volume	$314.23(6)$ Å ³	
Z	2	
Density (calculated)	3.464 Mg/m ³	
Absorption coefficient	7.993 mm ⁻¹	
F(000)	317	
Crystal size	0.36 x 0.22 x 0.16 mm ³	
Theta range for data collection	3.65 to 29.15°.	
Index ranges	-10 ≤ h ≤ 10, -10 ≤ k ≤ 10, -6 ≤ l ≤ 6	
Reflections collected	2661	
Independent reflections	438 [R(int) = 0.0270]	
Completeness to theta = 29.15°	94.0 %	
Absorption correction	multi-scan	
Refinement method	Full-matrix least-squares on F ²	
Data / restraints / parameters	438 / 0 / 35	
Goodness-of-fit on F ²	1.197	
Final R indices [I > 2σ(I)]	R1 = 0.0208, wR2 = 0.0520	
R indices (all data)	R1 = 0.0210, wR2 = 0.0521	
Absolute structure parameter	-0.02(3)	
Extinction coefficient	0.028(12)	
Largest diff. peak and hole	0.592 and -0.443 e.Å ⁻³	

Interatomic distances (Table 4.5.3) show that (Ca,Sr) is coordinated by eight oxygens and the (Ca,Sr)-O distances range from 2.460(3) to 2.629(3). The average distance of 2.593(4) is between the sum of the ionic radii of Ca^{2+} - O^{2-} (2.54Å) and that of Sr^{2+} - O^{2-} (2.68Å). There are four compressed and four stretched (Ca,Sr)-O bonds.

The CoO_4 tetrahedron contains four regular Co-O bonds which are equal to 1.946(2)Å. However, both angles $\text{O}(3)^5$ -Co-O(3)⁶ and $\text{O}(3)^2$ -Co-O(3)⁷ are 113.10° and indicate that the CoO_4 tetrahedron is slightly flattened on [001]. The SiO_4 tetrahedron, being more distorted, has three different Si-O bonds. The Si-O(2)⁸ is compressed and the Si-O(1)² and the Si-O(3)^{1,4} are stretched. The $\text{O}(2)^8$ -Si-O(3)¹ and $\text{O}(2)^8$ -Si-O(3)⁵ angles are 117.93° and deviate clearly from the regular tetrahedral angle of 109.47°.

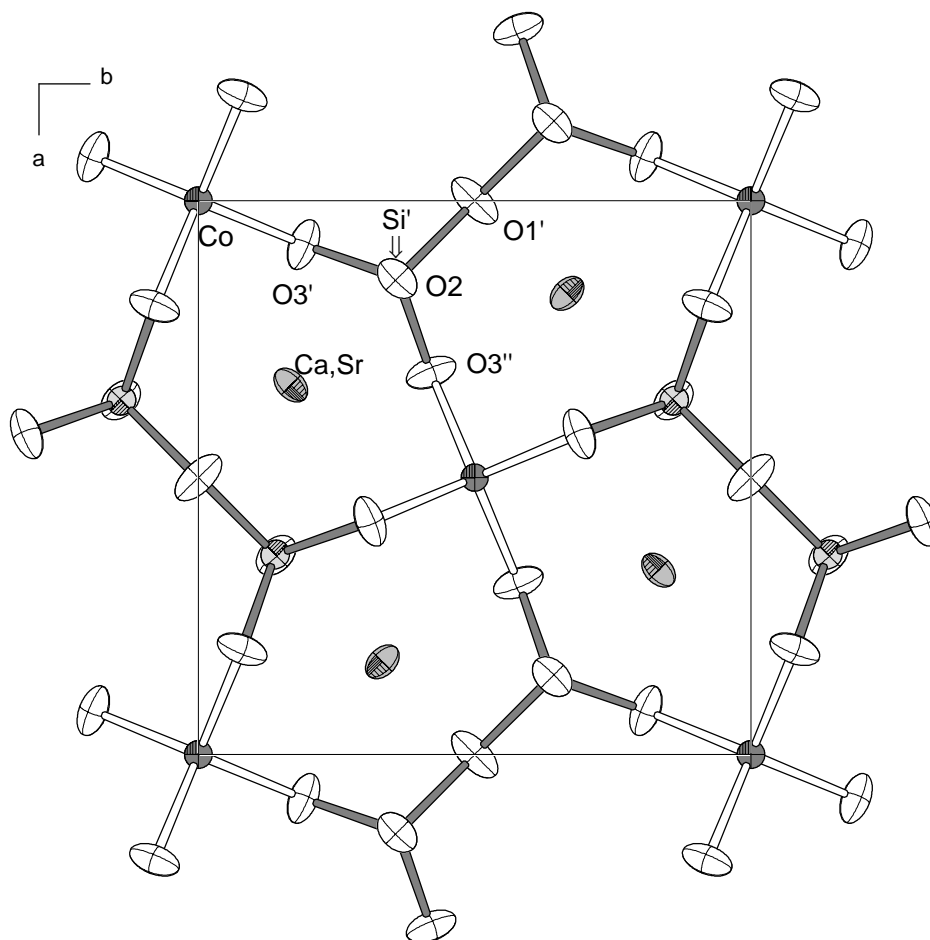


Fig.4.5.3 Projection in [001] of $(\text{Ca}_{0.75}\text{Sr}_{0.25})_2\text{CoSi}_2\text{O}_7$ according to main structure refinement at 233K. Section of an anionic layer around $z = 0$ and cations at $z = 0.5$. Displacement ellipsoids at the 50% level.

Table 4.5.3 Interatomic distances (Å) and tetrahedral angles ($^\circ$)

	$(\text{Ca}_{0.75}\text{Sr}_{0.25})_2\text{CoSi}_2\text{O}_7$		$(\text{Ca}_{0.787}\text{Sr}_{0.13})_2\text{CoSi}_2\text{O}_7$
	233K	100K	297K
$(\text{Ca,Sr})\text{-O}(3)^{1,4}$	2.460(3)	2.461(3)	2.446(2)
$(\text{Ca,Sr})\text{-O}(3)^{2,3}$	2.692(3)	2.690(4)	2.690(2)
$(\text{Ca,Sr})\text{-O}(2)^{1,3}$	2.720(2)	2.717(3)	2.716(2)
$(\text{Ca,Sr})\text{-O}(2)^2$	2.490(3)	2.489(4)	2.487(2)
$(\text{Ca,Sr})\text{-O}(1)^2$	2.511(3)	2.515(4)	2.505(2)
Mean	2.593(4)	2.592(9)	2.587(2)
$\text{Co-O}(3)^{2,5,6,7}$	1.946(2)	1.942(3)	1.944(2)
$\text{Si-O}(1)^2$	1.652(18)	1.649(2)	1.651(1)
$\text{Si-O}(2)^8$	1.595(3)	1.590(4)	1.596(2)
$\text{Si-O}(3)^{1,4}$	1.622(2)	1.621(3)	1.621(2)
$\text{O}(3)^{2(5)}\text{-Co-O}(3)^{7(6)}$	113.10(13)	113.24(19)	112.70(7)
$\text{O}(2)^8\text{-Si-O}(3)^{5(1)}$	117.93(10)	117.94(10)	118.00(9)
$\text{O}(3)^{1(4)}\text{-Si-O}(1)$	101.40(13)	101.37(18)	101.47(9)
$\text{O}(3)\text{-Si-O}(3)^1$	105.14(18)	105.30(3)	104.92(10)

Comparing the data in Table 4.5.3 taken at 233K and at 100K, the variation with temperature has a small effect on the bond lengths and bond angles i.e. on the tetrahedra. Increasing the substitution of Sr for Ca increases the Ca-O bond length.

4.5.2 The modulated structure and the transition from the incommensurate to the normal phase with varying Sr-content

The modulated structure can be shown easily by electron diffraction patterns at room temperature if the Sr content is lower than 25% (Fig.4.5.4). Satellite reflections in $(\text{Ca}_{0.75}\text{Sr}_{0.25})_2\text{CoSi}_2\text{O}_7$, which were observed by Iishi et al. [8], could not be observed. Even at low temperature, the satellite reflections are quite weak and show strong diffusion around the main reflections (Fig.4.5.4b). The reason for the different results probably comes from the actual content of Sr in the specimen. As described above, the Sr-content in our sample was investigated by the precise WDS technique and also by EDS and XRD. Therefore, we think that $x = 0.25$ is close to the composition at which the phase transition occurs from the incommensurate to the normal state.

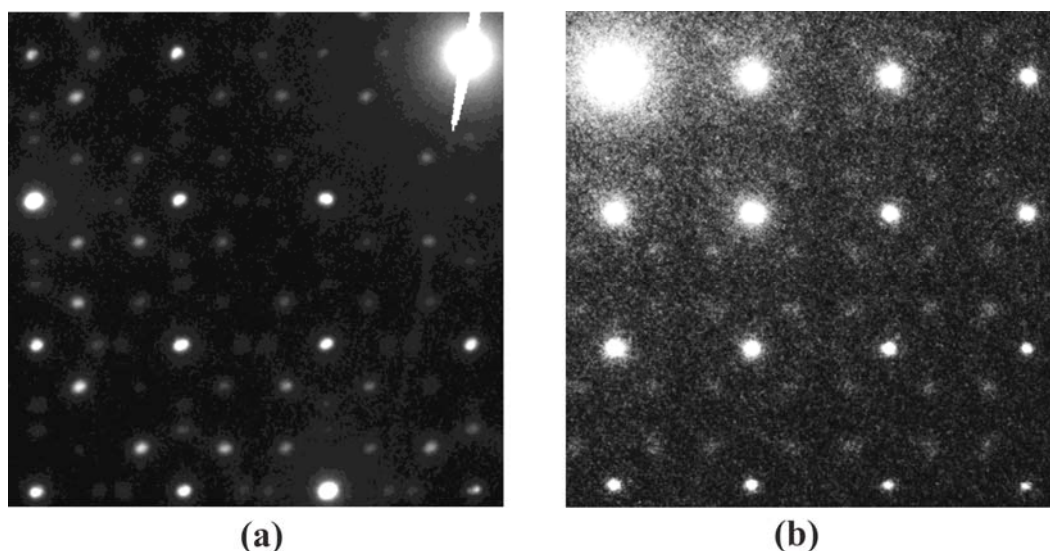


Fig.4.5.4 Electron diffraction patterns of Ca,Sr-melilites taken from [001]. (a) $(\text{Ca}_{0.9}\text{Sr}_{0.1})_2\text{CoSi}_2\text{O}_7$ at room temperature; (b) $(\text{Ca}_{0.75}\text{Sr}_{0.25})_2\text{CoSi}_2\text{O}_7$ at 90K.

XRD measurements were also performed for $(\text{Ca}_{0.75}\text{Sr}_{0.25})_2\text{CoSi}_2\text{O}_7$. The satellite reflections can be detected but only with a long collecting time at room temperature. It is intelligible that satellites are not observed from EDPs. The variation of the satellites

intensity with respect to the main reflections is shown in Fig.4.5.5. The intensity decreases with increasing temperature and is less than 0.01 at 300K. The intensity of satellites at 100K increases with cooling time indicating the existence of hysteresis.

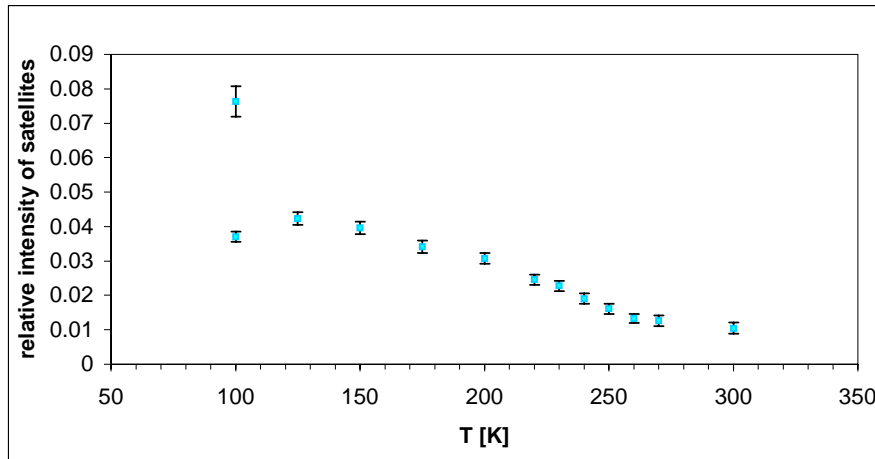


Fig.4.5.5 Intensity ratio of the satellite $\bar{3}\bar{4}\bar{3}10$ to the main reflection $\bar{3}\bar{4}\bar{3}$ with varying temperature. The spot with stronger intensity at 100K was measured after a long cooling time

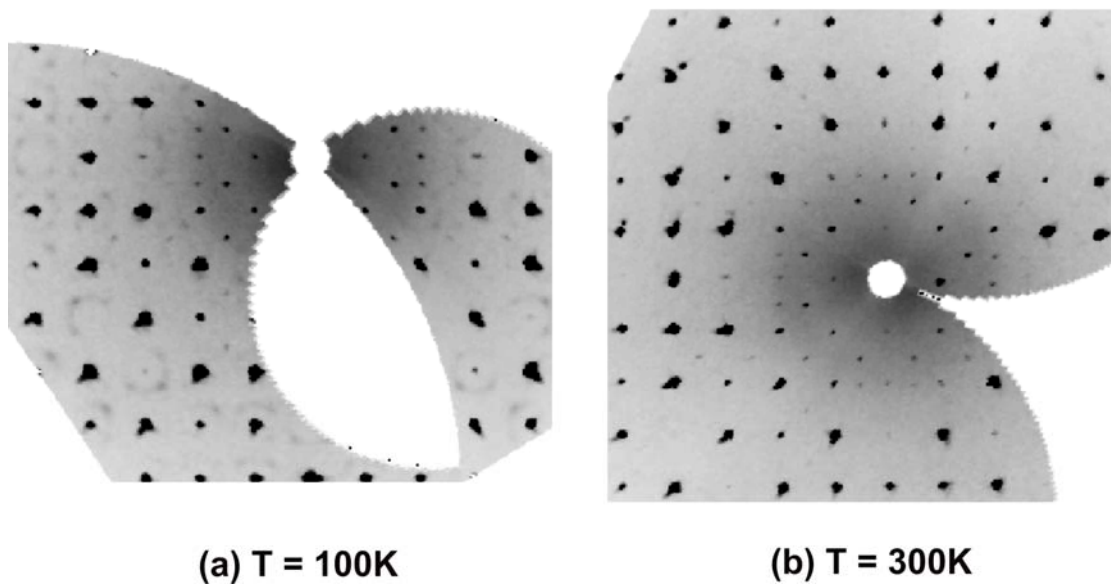


Fig.4.5.6 The $hk0$ -layers of $(\text{Ca}_{0.7}\text{Sr}_{0.3})_2\text{CoSi}_2\text{O}_7$ calculated from IPDS-II images. The weak satellite reflections and its strong diffuse scattering forming rings around the main reflections are observable at 100K, revealing the modulated structure. Only the main reflections are observed at RT. The low-angle reflections seemingly causing doubling of a and b axes (as well as of c in other layers) are probably due to the $\lambda/2$ -effect.

Until now, the modulated structure in $(\text{Ca}_{1-x}\text{Sr}_x)_2\text{CoSi}_2\text{O}_7$ was revealed by electron diffraction patterns in the range of $0 \leq x \leq 0.25$ [8]. For $(\text{Ca}_{0.7}\text{Sr}_{0.3})_2\text{CoSi}_2\text{O}_7$, the X-ray diffraction investigations were performed between room temperature and 100K. No satellite reflections were observed at RT, but one could see weak satellites at 100K (Fig.4.5.6). This means that the phase transition from the normal to the incommensurate state occurs during decreasing the temperature down to 100K, which confirmed the conjecture by Bagautdinov et al. [15]. The series of measurements with temperature revealed that the T_{1-N} is about 275K. The intensity of satellite reflections increases with lowering the temperature. These experiments gave a powerful confirmation that the modulated structure is caused by the misfit between the interlayer X cation and the tetrahedra sheet. The substitution of Ca by Sr should cause a relaxation in the distortion of the structure through increasing the X-O bond length.

Some magnetic measurements

The magnetic measurements of polycrystalline samples of melilites containing Co^{2+} ions were carried out. The magnetisation of a substance is normally expressed by a term of magnetic susceptibility χ . The change of χ with temperature reveals the magnetic state at corresponding temperature. Despite the magnetic moment of Co^{2+} these melilites show no net magnetic moment at room temperature because of the random orientation of the magnetic moments. Fig.4.5.7 shows the temperature dependence of the susceptibility χ measured between 2K and 330K under an external field of $H=10.000\text{Oe}$. The curve of the inverse susceptibility $1/\chi$ vs T was plotted. The experimental data were fitted independently in the ranges 50K-150K and 250K-330K, respectively. From the linear fits the Curie constants C and the paramagnetic Curie temperatures θ_p (see in Table 4.5.4) were derived according to the formula $\frac{1}{\chi} = \frac{1}{C}(T - \theta_p)$. The negative values of θ_p indicate antiferromagnetic (AF) interactions of the Co^{2+} ions. The effective paramagnetic moment μ_{eff} can also be calculated by the formula $\mu_{eff} = \sqrt{\frac{3k_B C}{N \cdot z \cdot \mu_B^2}}$, where μ_B is the Bohr magneton, N Avogadro's number, k_B Boltzmann's constant and z the number of magnetic ions (Co^{2+} , $z = 1$) per formula unit. The calculated results were also listed in Table 4.5.4.

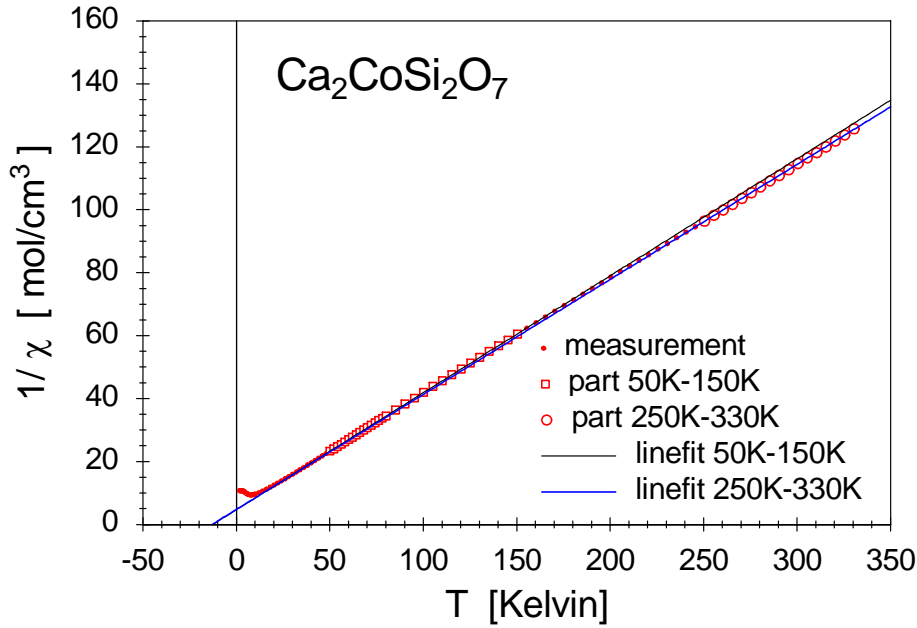


Fig.4.5.7 χ^{-1} of $\text{Ca}_2\text{CoSi}_2\text{O}_7$ as a function of temperature for an external magnetic field of $H = 10.000\text{Oe}$. Two linear fits are shown for the temperature ranges: 50K – 150K and 250K – 330K.

Table 4.5.4 The Curie constants C and the temperatures θ_p obtained from the linear fits and the calculated μ_{eff} for $\text{Ca}_2\text{CoSi}_2\text{O}_7$.

50K – 150K	250K – 330K
$C = 2.69\text{cm}^3\text{K/mol}$	$C = 2.74\text{cm}^3\text{K/mol}$
$\theta_p = -12.5\text{K}$	$\theta_p = -13.0\text{K}$
$\mu_{eff} = 4.64\mu_B$	$\mu_{eff} = 4.68\mu_B$

The effective paramagnetic moments, μ_{eff} , calculated from two temperature ranges of 50K-150K and 250K-330K have a slight difference. This may be caused by the slight change of the structure with temperature. The commensurate lock-in to the incommensurate phase transition of $\text{Ca}_2\text{CoSi}_2\text{O}_7$ takes place at *ca.*250K^[29]. The structure before and after the transition temperature shows a slight change which is indicated in the diffraction patterns by positional shifts of satellites. This kind of change of the structure is ascribed to the change of the strain between the tetrahedra framework and the Ca cations layer as well as the rotation and distortion of CoO_4 - and SiO_4 -tetrahedra, which results in the change of the sum magnetic moment of the Co^{2+} ions.

Similarly, magnetic measurements have been done for the $(\text{Ca}_{0.75}\text{Sr}_{0.25})_2\text{CoSi}_2\text{O}_7$ compound. The correlation between the inverse magnetic susceptibility and temperature as well as the fit lines is plotted in Fig.4.5.8. The change of $1/\chi$ with

temperature is also divided into two parts. The Curie constants C and the paramagnetic Curie temperatures θ_p as well as the calculated effective paramagnetic moments μ_{eff} are quite different below and above 200K (Table 4.5.5). Comparing these values with the values for $\text{Ca}_2\text{CoSi}_2\text{O}_7$, the substitution of 25% Sr for Ca increases the difference of the magnetic parameters in the two temperature ranges.

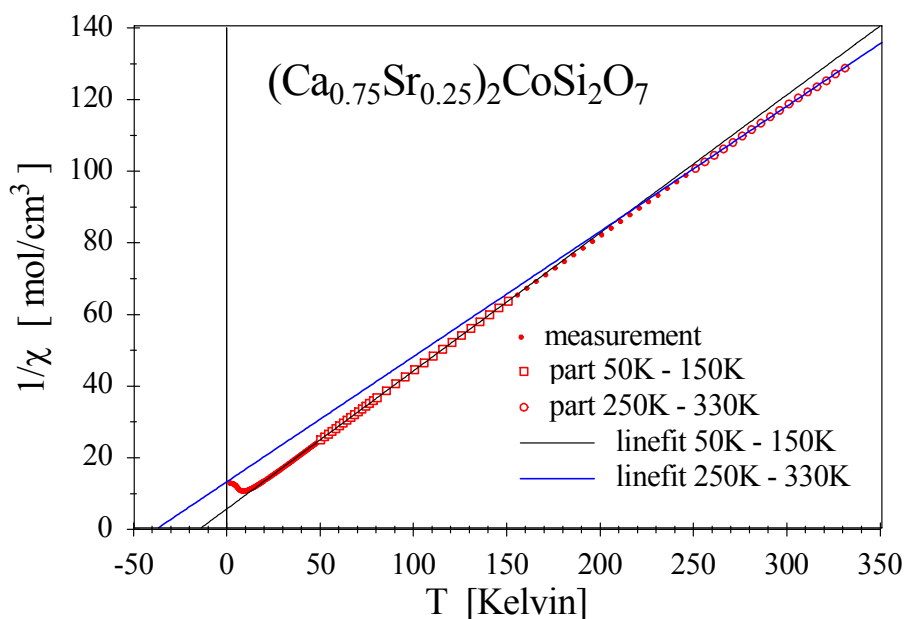


Fig.4.5.8 χ^{-1} of $(\text{Ca}_{0.75}\text{Sr}_{0.25})_2\text{CoSi}_2\text{O}_7$ as a function of temperature for an external magnetic field of $H=10.000\text{Oe}$ (ZFC-mode). Two fits are shown for the temperature ranges: 50K – 150K and 250K – 330K.

Table 4.5.5 The Curie constants C and the paramagnetic Curie temperatures θ_p obtained from the linear fits and the calculated magnetic moments μ_{eff} for $(\text{Ca}_{0.75}\text{Sr}_{0.25})_2\text{CoSi}_2\text{O}_7$.

50K – 150K	250K – 330K
$C = 2.60\text{cm}^3\text{K/mol}$	$C = 2.86\text{cm}^3\text{K/mol}$
$\theta_p = -14.2\text{K}$	$\theta_p = -37.2\text{K}$
$\mu_{eff} = 4.56\mu_B$	$\mu_{eff} = 4.78\mu_B$

All investigated compounds are isomorphous. In the paramagnetic state we find different behaviour below and above 200K. This effect can be corrected by assuming a temperature independent paramagnetic susceptibility of about $\chi_0 \approx 0.001\text{ cm}^3/\text{mol}$.

The transition from the paramagnetic state to a magnetically ordered state with long-range correlations between the magnetic moments is a real magnetic phase transition. From the paramagnetic Curie temperature obtained from the fit lines the final low-temperature transition should be an antiferromagnetic one ($\theta_p < 0$). The

magnetic susceptibility at low temperatures was measured and the Neel temperature T_N is *ca.*5.7K. An additional effect plays an important role, namely a weak ferromagnetism (WF) when temperature is lower than T_N . A canting of the spins is then formed with a canting angle, α , far less than 1° ($\alpha \approx 0.1^\circ$).

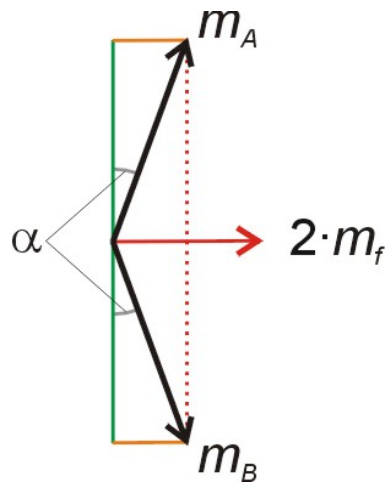


Fig.4.5.9 A scheme of canting resulting in a weak antiferromagnetism. α -the canting angle; m_A and m_B -two magnetic moments in mirror symmetry; $2m_f$ - the sum moment from m_A and m_B .

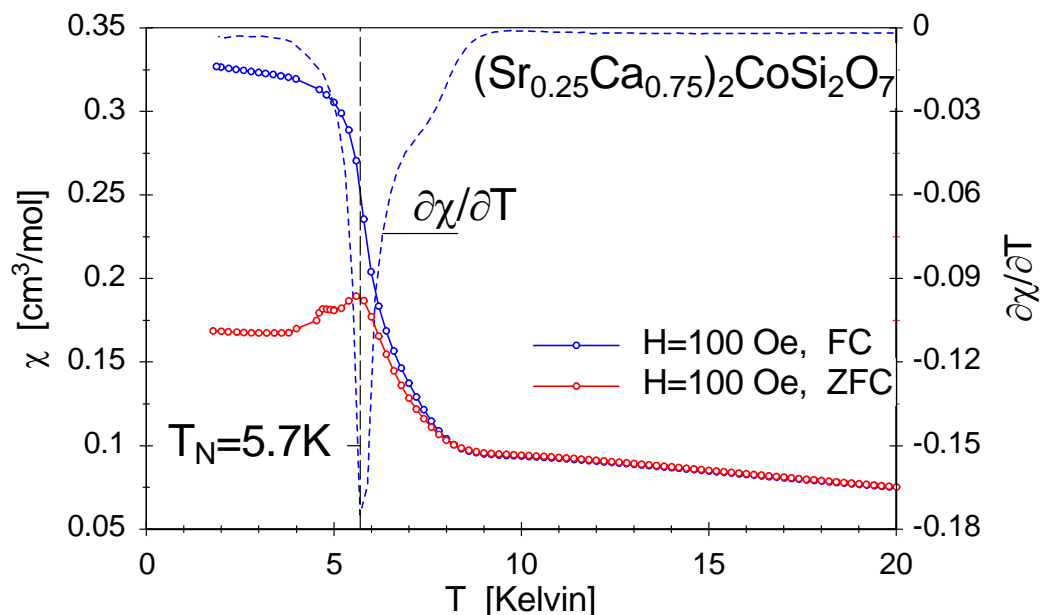


Fig.4.5.10 The temperature dependence of the magnetic susceptibility in $\text{Ca}_{0.75}\text{Sr}_{0.25}\text{CoSi}_2\text{O}_7$ at an external field of $H = 100$ Oe measured with the Zero-Field-Cooled (ZFC) and Field-Cooled (FC) mode. The Neel temperature $T_N = 5.7\text{K}$ is fixed by the inflection point of the blue curve (FC-mode). The minimum of the first partial derivative $\partial\chi/\partial T$ (dotted blue curve) is identical with the maximum of the red curve (ZFC-mode) typical for antiferromagnetism.

The two sublattices m_A and m_B exist spontaneously canted without external magnetic field. The magnetic phase transition was determined very clearly at a low field of $H=100$ Oe (Fig.4.5.10).

The weak ferromagnetism (WF) is manifested macroscopically once the 3D order sets in; for this reason the WF transition temperature will be associated with the 3D AF order of the Co^{2+} ions. The separation of the tetrahedral planes plays an important role in the difference between the intralayer interactions (J_{\parallel}) and the interlayer ones (J_{\perp}) of the Co^{2+} ions. Low dimensional correlations as 1D or 2D are still active above T_N . Whether the relation $J_{\parallel} > J_{\perp}$ is appropriate or not must be decided by theoretical calculations.

Just below the Neel temperature i.e. at $T = 5\text{K}$ we measured the complete field dependence of the magnetisation of $\text{Ca}_{0.75}\text{Sr}_{0.25}\text{CoSi}_2\text{O}_7$. The parameter of the hysteresis loop are given by the coercivity $H_{C1} = 274$ Oe, $H_{C2} = -272$ Oe and the remanent moment $m_{r1} = 0.0054\mu_B$, $m_{r2} = -0.0054\mu_B$.

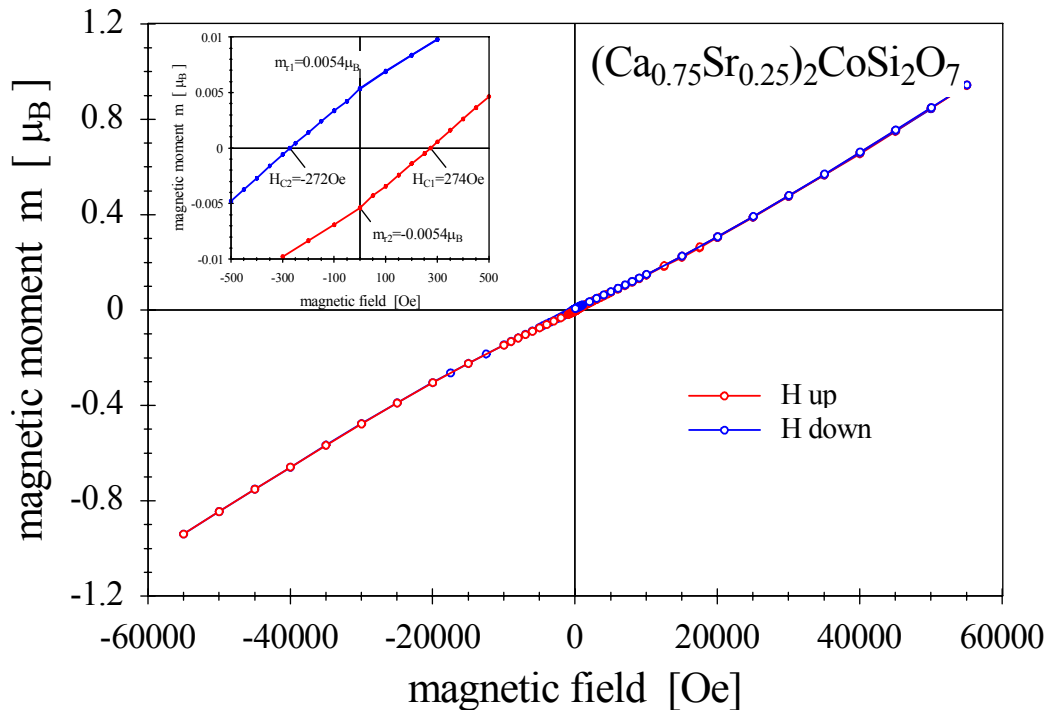


Fig.4.5.11 The magnetic moment m of $(\text{Ca}_{0.75}\text{Sr}_{0.25})_2\text{CoSi}_2\text{O}_7$ as a function of the external magnetic field H at $T = 5\text{K}$. The inset illustrates the loop parameter of the hysteresis.

All magnetisation measurements of the samples $(\text{Ca}_{1-x}\text{Sr}_x)_2\text{CoSi}_2\text{O}_7$ show in principle the same characteristic features as presented above. Weak ferromagnetism is

generated in these materials by a very slight canting of the Co moments from a perfect antiferromagnetic structure below T_N . The intra- and interlayer interactions of the Co^{2+} ions regulate the 3D character at the point at which the phase transition occurs. Due to a weaker interlayer coupling (J_{\perp}) above T_N J_{\parallel} may still be active and then a lower dimensional magnetism will follow up to about 10K.

4.5.3 Conclusions

High-quality crystals of $(\text{Ca}_{1-x}\text{Sr}_x)_2\text{CoSi}_2\text{O}_7$ with $0 \leq x \leq 1$ were grown by FZ technique. A homogenous distribution of every constituent element is reached.

The refinement data of $(\text{Ca}_{0.75}\text{Sr}_{0.25})_2\text{CoSi}_2\text{O}_7$ according to the average structure show that the variation of temperature hardly affects the situation of Si-, Co-tetrahedra distortion. The substitution of Sr for Ca increases the X-O bond length, and accordingly, causes a relaxation of the distorted strain resulting to the phase transition from the incommensurate to the normal structure. The susceptibility in the paramagnetic state shows a slight change with temperature. Weak ferromagnetism exists below the Neel temperature 5.7K. Low dimensional magnetism remains up to 10K because the low dimensional correlations (1D or 2D) are still active well above T_N .

4.6 Investigations of $\text{Ca}_2(\text{Mg},\text{Co})\text{Si}_2\text{O}_7$ doped with Cr and Eu

The end-members of $\text{Ca}_2\text{MgSi}_2\text{O}_7$ and $\text{Ca}_2\text{CoSi}_2\text{O}_7$ exhibit at room temperature an incommensurately modulated structure along $\langle 110 \rangle$ and $\langle \bar{1} 10 \rangle$. Many studies have been done on both systems to understand the modulation formation. In addition, these compounds are also potential substrates for some active ions which can realize laser output or long-lasting fluorescence. In this section investigations on the Cr and Eu doping of $\text{Ca}_2\text{MgSi}_2\text{O}_7$ and $\text{Ca}_2\text{CoSi}_2\text{O}_7$ were described.

4.6.1 Synthesis and characterization of $\text{Ca}_2\text{MgSi}_2\text{O}_7:\text{Cr}$ solid solutions

Since the laser action of $\text{Cr}^{4+}:\text{Mg}_2\text{Si}_2\text{O}_4$ in the near infra-red region was reported [65], Cr^{4+} -doped crystals have been attracted and studied extensively to find new and more suitable hosts [66-68]. Cr^{4+} is often unstable and may be reduced to Cr^{3+} , which is the most common valence state in nature, or oxidized to Cr^{6+} . Within melilites no suitable sites are present for Cr^{3+} , however, tetrahedral sites needed by Cr^{4+} may be provided by the Si-sites.

$\text{Ca}_2\text{MgSi}_2\text{O}_7:\text{Cr}$ polycrystalline powder was synthesized using high purity CaCO_3 (99.97%, Merck), MgO (99.999%, Ventron GMBH) and Cr_2O_3 (99.997%, Alfa Aesar) powders as raw materials. The molar concentration of added Cr_2O_3 was 1, 2 and 10 mol %, respectively. The synthesizing procedure was similar to that for the end-member $\text{Ca}_2\text{MgSi}_2\text{O}_7$. Crystals with pale purple color and usually about 30-40mm length and 3-5mm diameter were obtained. Fig.4.6.1 shows the as-grown crystal $\text{Ca}_2\text{MgSi}_2\text{O}_7$ with nominal 1 mol % Cr. One part was cut from the top marked in Fig.4.6.1 and used for phase identification by XRD. All peaks can be indexed to the $\text{Ca}_2\text{MgSi}_2\text{O}_7$ phase according to ICSD-100736 (Fig.4.6.2), indicating that no foreign phase had formed.

One polished section cut from the middle part (see Fig.4.6.1) was used for chemical analysis by WDS. Data from three different areas of the sample show that the incorporated Cr content (*ca.* 0.01%) is much lower than the nominal one. So the measurement gives no quantitative Cr content but proves that only a small amount of Cr can be incorporated into the crystal. A similar result was obtained for $\text{Ca}_2\text{MgSi}_2\text{O}_7$ doped with nominal 2 mol % and 10 mol % Cr crystals. The Cr concentration increases only slightly with increasing nominal Cr content and the quality of the

crystals become increasingly worse. The reason is obviously the formation of additional phase of $\text{Ca}_3\text{MgSi}_2\text{O}_8$. This can be clearly seen in polarized-light optical images in Fig.4.6.3.

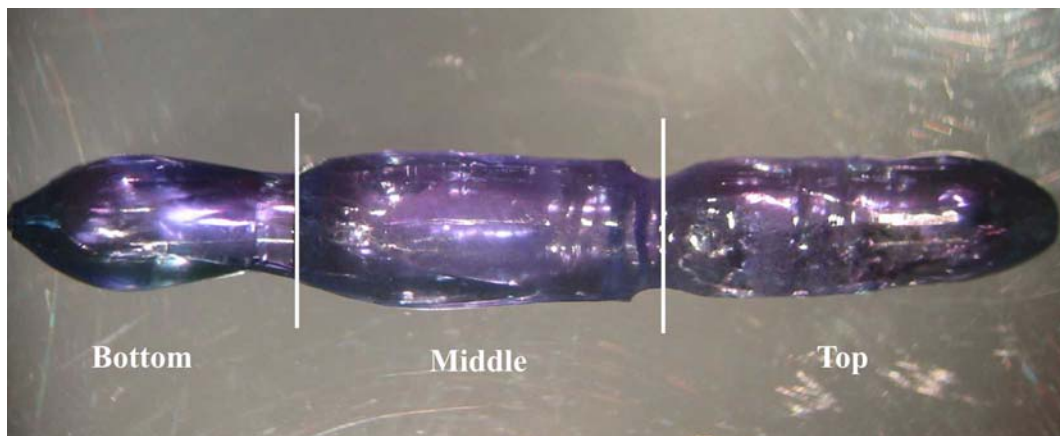


Fig.4.6.1 As-grown crystal of $\text{Ca}_2\text{MgSi}_2\text{O}_7$ with nominal 1 mol % Cr. The crystal is 30mm in length and 3-5mm in diameter.

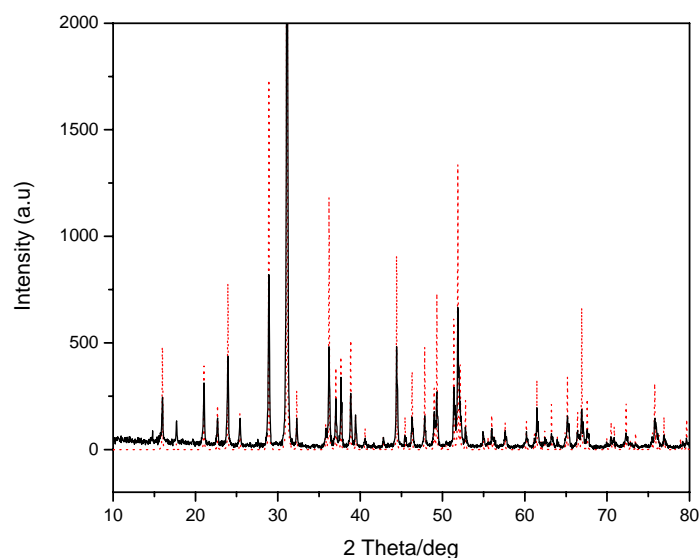


Fig.4.6.2 XRD diagram of the $\text{Ca}_2\text{MgSi}_2\text{O}_7$ crystal with nominal 1 mol % Cr (black solid line) and the data of $\text{Ca}_2\text{MgSi}_2\text{O}_7$ from ICSD (red dotted line).

The as-grown crystal $\text{Ca}_2\text{MgSi}_2\text{O}_7$ with nominal 1 mol % Cr appears almost homogenous (Fig.4.6.3a). The $\text{Ca}_2\text{MgSi}_2\text{O}_7$ crystal with nominal 10 mol % Cr shows many cracks and includes two additional phases, $\text{Ca}_3\text{MgSi}_2\text{O}_8$ and properly Mg_2CrO_4

(Fig.4.6.3b). The cracks in $\text{Ca}_2\text{MgSi}_2\text{O}_7$ with nominal 1 mol % Cr can be explained by the fact that a Pt wire instead of a seed crystal was used as growth nucleus.

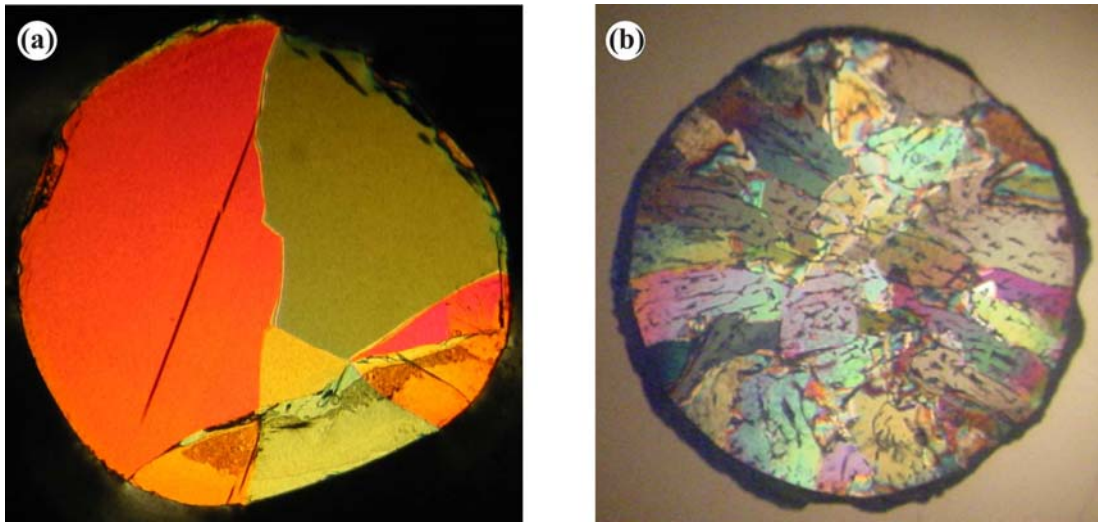


Fig.4.6.3 Thin polished sections (*ca.* $50\mu\text{m}$) observed by polarized-light optical microscopy. (a) $\text{Ca}_2\text{MgSi}_2\text{O}_7$ with nominal 1 mol % Cr crystal; (b) $\text{Ca}_2\text{MgSi}_2\text{O}_7$ with nominal 10 mol % Cr crystal.

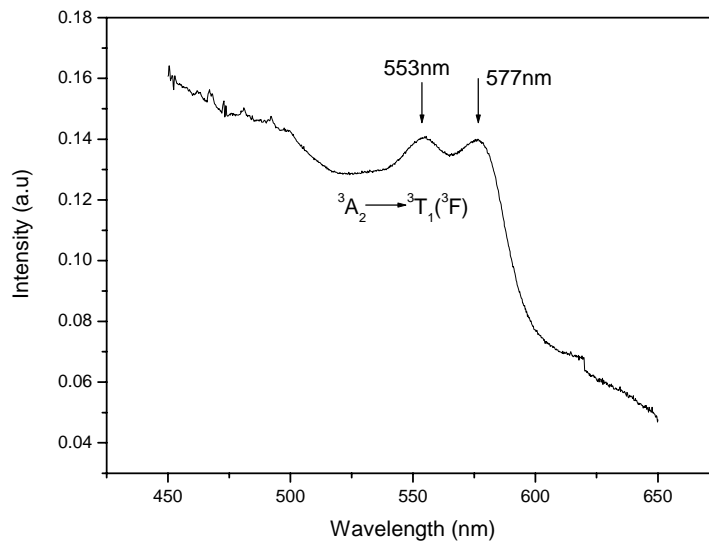


Fig.4.6.4 The excitation spectrum of $\text{Ca}_2\text{MgSi}_2\text{O}_7$ with nominal 1 mol % Cr crystal. Two evident peaks correspond to the transitions of $A_2 - {}^3T_1 ({}^3F)$ of Cr^{4+} ion.

From the chemical analyses, a small amount of Cr was distributed into $\text{Ca}_2\text{MgSi}_2\text{O}_7$, but the valence state of Cr was unknown. The photoluminescent measurements have been performed which are more sensitive than other methods. An excitation spectrum

of $\text{Ca}_2\text{MgSi}_2\text{O}_7$ with nominal 1 mol % Cr is given in Fig.4.6.4. Two peaks with the maximum values of 553nm and 577nm are observed. Comparison of this result with the theoretically calculated data for Cr^{4+} by Ishii et al. [69], and with experimental results by Sugimoto et al. [70] for $\text{Ca}_2\text{MgSi}_2\text{O}_7$ shows that these two peaks correspond to the transitions of ${}^3\text{A}_2 - {}^3\text{T}_1$, ${}^3\text{A}_2 - {}^3\text{F}$ of Cr^{4+} . The intensity of the two peaks is quite weak in accordance with the chemical analysis, which indicates only a small amount of Cr^{4+} at Si^{4+} sites.

4.6.2 Synthesis, characterization and optical properties of $\text{Ca}_2\text{Mg}(\text{Co})\text{Si}_2\text{O}_7:\text{Eu}$ solid solutions

Eu occurs in the valence states +2 or +3. Eu^{2+} may emit long-lasting fluorescence in some substrates e.g. $\text{Ca}_3\text{MgSi}_2\text{O}_8$ [71-73]. It is also a potential ion realizing near ultraviolet-wavelength laser action.

Eu_2O_3 (99.99%, Merck) was used as raw material. High purity powders were precisely weighed, mixed and calcined in a program-controlled oven at different atmospheres.

Fig.4.6.5 shows the XRD diagram of $\text{Ca}_2\text{MgSi}_2\text{O}_7$ with nominal 5 mol % Eu synthesized at different conditions. The sample synthesized in air condition shows mainly the $\text{Ca}_2\text{MgSi}_2\text{O}_7$ phase, but some additional weak peaks were also observed and marked by arrows. They do not belong to $\text{Ca}_2\text{MgSi}_2\text{O}_7$ phase and could not be removed even by synthesizing the sample in high-purity N_2 atmosphere or by additional sintering runs in air. $\text{Ca}_2\text{MgSi}_2\text{O}_7$ doped with low concentrations Eu, e.g. 2, 1, 0.5 and 0.1 mol %, showed the same impurity peaks. Based on these experiments it must be assumed that the Eu may substitute Ca but form another compound in oxidative and inert atmosphere.

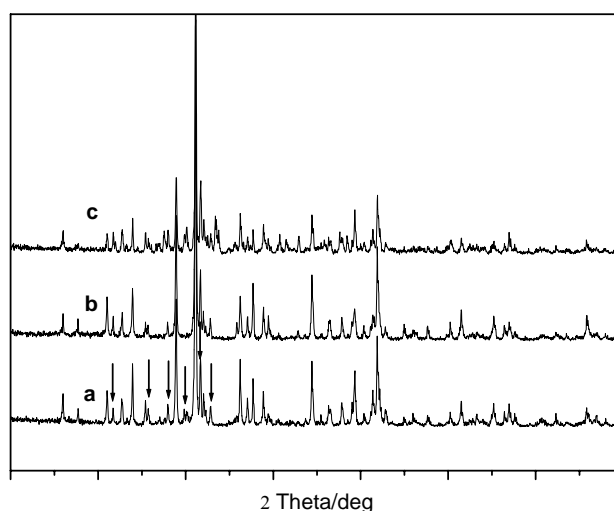


Fig.4.6.5 XRD diagram of $\text{Ca}_2\text{MgSi}_2\text{O}_7$ with nominal 5 mol % Eu synthesized at different conditions. a) at air atmosphere; b) crystal sample; c) at high purity N_2 atmosphere. Additional diffraction peaks are marked by arrows.

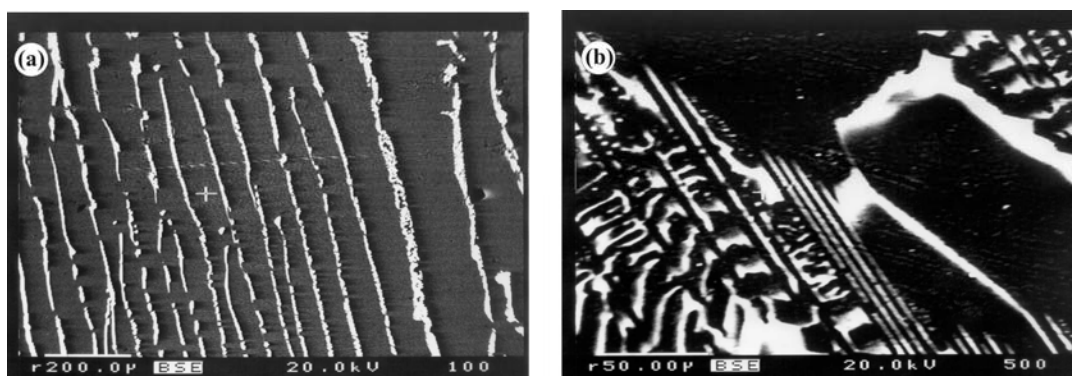


Fig.4.6.6 Backscattered electrons images of (a) $\text{Ca}_2\text{MgSi}_2\text{O}_7$ with nominal 5 mol % Eu and (b) $\text{Ca}_2\text{MgSi}_2\text{O}_7$ with nominal 2 mol % Eu. The white stripes observed in both images are due to the formation of $\text{Ca}_2\text{Eu}_8\text{Si}_6\text{O}_{26}$ compound.

Further experiments have been done to find out more about the impurity phase. Thin sections cut from the bulk crystals were polished and the backscattered electrons images were taken (Fig.4.6.6) show white stripes perpendicular to the growing direction. The shapes and the distribution of these stripes are affected by the stability of the growing process. The chemical analysis of $\text{Ca}_2\text{MgSi}_2\text{O}_7$ with nominal 5 mol % Eu sample was carried out along the growing direction by selecting 200 spots ($\phi = 10\mu\text{m}$) at a small interval. The results of the Eu concentration are shown in Fig.4.6.7. The Eu concentration in dark areas is low (*ca.* 0.24 wt %), however, rises evidently to

4.6 Investigations of $\text{Ca}_2(\text{Mg},\text{Co})\text{Si}_2\text{O}_7$ doped with Cr and Eu

ca. 53.13 wt % in the white stripe areas, indicating the existence of two different compounds. Combining the chemical analysis for all elements with the XRD database, $\text{Ca}_2\text{Eu}_8\text{Si}_6\text{O}_{26}$ can be ascribed to the white stripes, and $\text{Ca}_2\text{MgSi}_2\text{O}_7$ doped with a small amount of Eu to the dark areas.

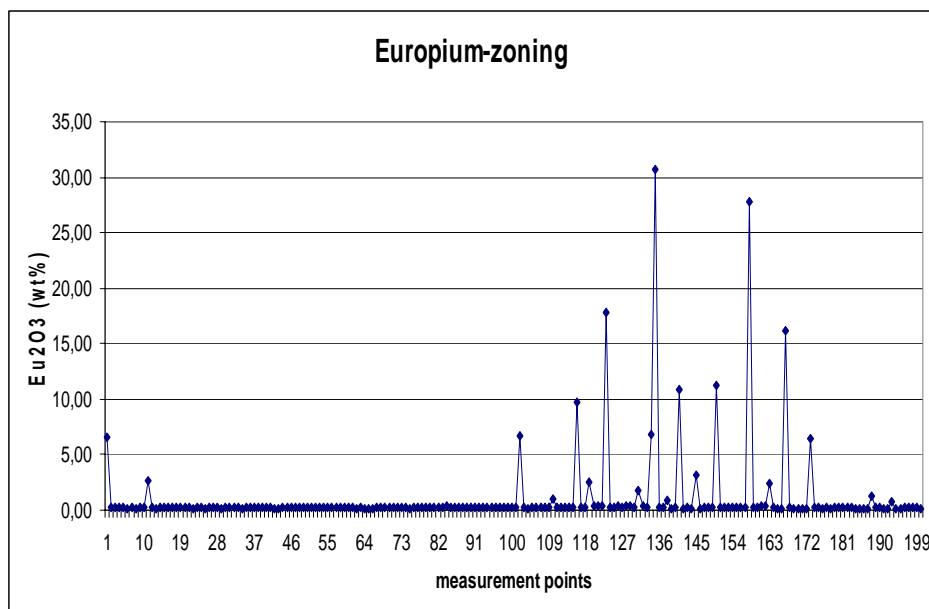


Fig.4.6.7 The compositional analysis of $\text{Ca}_2\text{MgSi}_2\text{O}_7$ with nominal 5 mol % Eu by selecting 200 spots along the growing direction. The Eu content obviously rises in the white area.

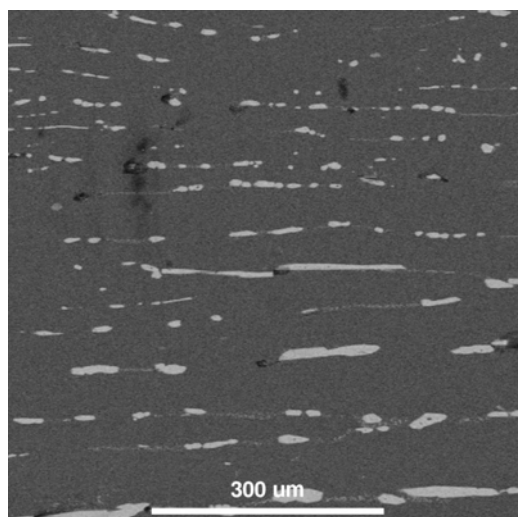


Fig.4.6.8 Backscattered electrons image of $\text{Ca}_2\text{MgSi}_2\text{O}_7$:5 mol % Eu after annealing 120h at 1350°C . The continuous stripes became discontinuous.

After annealing $\text{Ca}_2\text{MgSi}_2\text{O}_7$ with nominal 5 mol % Eu at 1350°C for 120h, the backscattered electrons image of the same area shows that the continuous stripes become discontinuous (Fig.4.6.8). An increase of Eu has not been found in the dark areas. This means annealing makes the $\text{Ca}_2\text{Eu}_8\text{Si}_6\text{O}_{26}$ compound more aggregative.

The photoluminescent spectra of $\text{Ca}_2\text{MgSi}_2\text{O}_7$ crystals with nominal 5 mol % Eu, 2 mol % Eu and the powder $\text{Ca}_2\text{Eu}_8\text{Si}_6\text{O}_{26}$ compound are shown in Fig.4.6.9. The spectra have similar shape, but the emission intensity of the crystal samples is stronger than that of the powder sample. This is because the crystal samples have better crystallization than the powder sample. Due to the valence state Eu^{3+} in $\text{Ca}_2\text{Eu}_8\text{Si}_6\text{O}_{26}$, the emission from all three samples results from the Eu^{3+} . The emission from Eu^{2+} is not observed in these spectra. Therefore, further experiments were carried out using reduced atmosphere.

The synthesis of the $\text{Ca}_2\text{MgSi}_2\text{O}_7:\text{Eu}$ compound was also carried out in reduced atmosphere (90% N_2 and 10% H_2). The synthetic powder is pale yellow. The photoluminescent spectroscopic and ESR measurements were performed. The emission spectra are plotted in Fig.4.6.10. A peak at maximum 524nm is observed, which is different from that in Fig.4.6.9. This emission peak agrees with that of Eu^{2+} which is measured by Jiang et al. [24]. In our experiments, the emission peak at 447nm observed by Jiang et al. is almost invisible. The ESR spectrum taken at liquid He temperature shows a broad peak indicating the existence of Eu^{2+} (Fig.4.6.11).

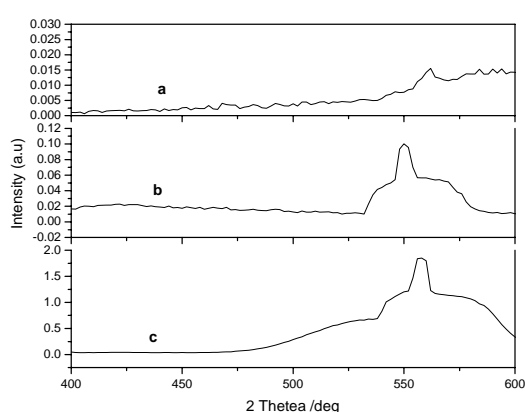


Fig.4.6.9 Emission spectra of (a) $\text{Ca}_2\text{Eu}_8\text{Si}_6\text{O}_{26}$ powder; (b) $\text{Ca}_2\text{MgSi}_2\text{O}_7$ with nominal 2 mol % Eu crystal; (c) $\text{Ca}_2\text{MgSi}_2\text{O}_7$ with nominal 5 mol % Eu crystal synthesized at air atmosphere.

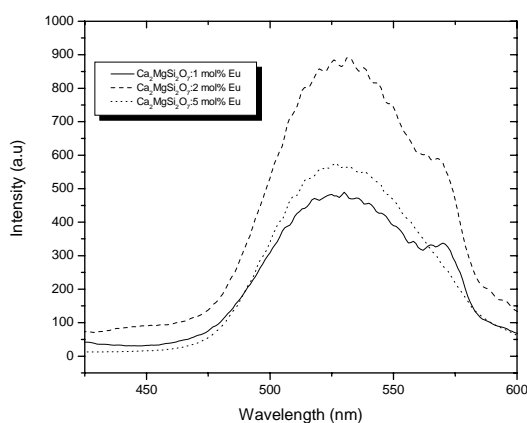


Fig.4.6.10 Emission spectra of $\text{Ca}_2\text{MgSi}_2\text{O}_7$ with nominal 1 mol % Eu synthesized at reduced atmosphere (90% N_2 + 10% H_2).

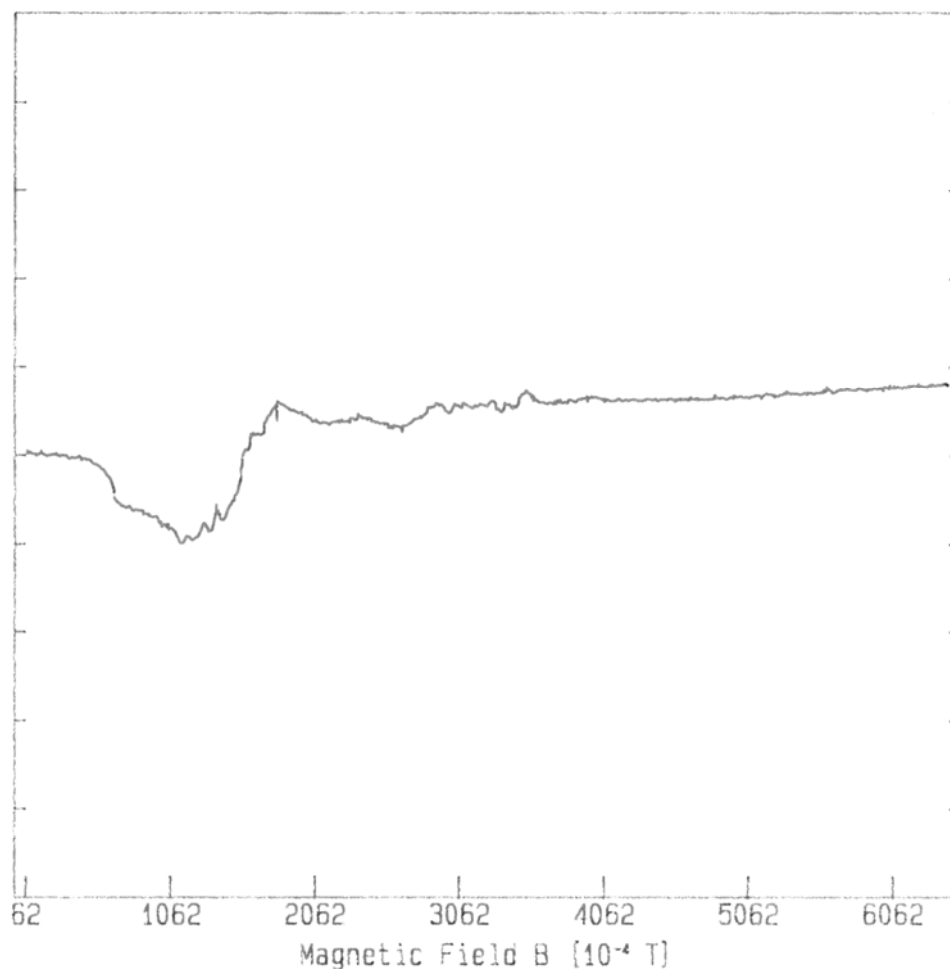


Fig.4.6.11 ESR spectrum of $\text{Ca}_2\text{MgSi}_2\text{O}_7$ with nominal 1 mol % Eu synthesized at reduced atmosphere (90% N_2 + 10% H_2).

The syntheses of $\text{Ca}_2\text{CoSi}_2\text{O}_7$ with x mol % Eu and $x = 0.1, 0.5, 1.0$ were also carried out in different atmospheres. Because of the sensitivity of Eu^{2+} to oxidation atmosphere, the synthesis was performed under the protection of inert or reduced atmosphere.

The stoichiometric mixture was first calcined in a tube-type oven at high-purity N_2 atmosphere. Each sintering run had been lasted for 48h. Even after three sintering runs, there were still the diffraction peaks which do not belong to the $\text{Ca}_2\text{CoSi}_2\text{O}_7$ phase as indicated by arrows in Fig.4.6.12b. The pure phase of $\text{Ca}_2\text{CoSi}_2\text{O}_7$ could be obtained after five sintering runs (Fig.4.6.12c). The crystallization process of Co-melilite is slower in N_2 than in air.

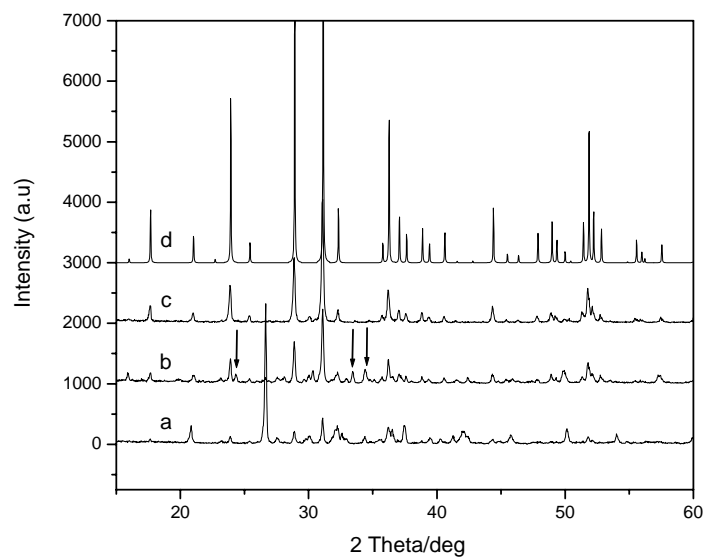


Fig.4.6.12 XRD diagrams of $\text{Ca}_2\text{CoSi}_2\text{O}_7$: 0.1 mol % Eu after several sintering runs at N_2 atmosphere. (a) first; (b) third; (c) fifth; (d) the data from ICSD-31236.

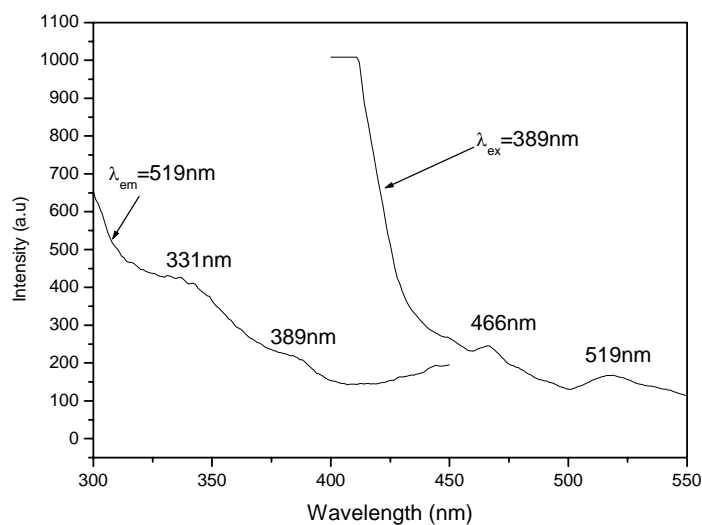


Fig.4.6.13 Excitation and emission spectra of $\text{Ca}_2\text{CoSi}_2\text{O}_7$: 0.5 mol % Eu.

The photoluminescent spectra of $\text{Ca}_2\text{CoSi}_2\text{O}_7$: 0.5 mol % Eu are shown in Fig.4.6.13. Two broad excitation peaks with the maxima at 331nm and at 389nm can be observed. After excitation, two different emissions with wavelengths of 466nm and 519nm are visible. The emission peaks are typical emission of Eu^{2+} ascribed to the 4f-5d transitions. The observation of two emission peaks indicated that there are two different luminescent centers. This can be explained by different Eu^{2+} sites substituting for Ca^{2+} . Kusaka et al ^[19] determined the structure of $\text{Ca}_2\text{CoSi}_2\text{O}_7$ at room

temperature and found six-fold coordinated Ca^{2+} sites except eight-fold coordinated ones. Therefore, Eu^{2+} also may occupy two kinds of sites, which form two different luminescent centers.

The sample synthesized at N_2 was also sintered again at the same heating procedure but under a reduced atmosphere (90% N_2 + 10% H_2). The obtained sample turned into grey color from deep blue. The XRD measurement shows that the $\text{Ca}_2\text{CoSi}_2\text{O}_7:\text{Eu}$ phase was decomposed in three other phases, i.e. Co, EuO and $\text{Ca}_3\text{Si}_3\text{O}_9$. This means that the $\text{Ca}_2\text{CoSi}_2\text{O}_7:\text{Eu}$ compound can not be synthesized in a reducing atmosphere.

4.6.3 Conclusions

Cr can substitute Si^{4+} as Cr^{4+} ion. The weak intensity from the excitation spectrum indicates that only a small amount of Cr enters the melilite structure in tetrahedral sites.

Eu can not be doped into $\text{Ca}_2\text{MgSi}_2\text{O}_7$ compound as Eu^{2+} neither in air nor in N_2 atmosphere. Another compound, $\text{Ca}_2\text{Eu}_8\text{Si}_6\text{O}_{26}$ is formed. However, Eu^{2+} substitutes Ca^{2+} in an atmosphere (90% N_2 + 10% H_2) as proved by photoluminescent spectroscopy.

$\text{Ca}_2\text{CoSi}_2\text{O}_7:\text{Eu}^{2+}$ compounds can be synthesized in N_2 in a rather slow process, but cannot be obtained in an atmosphere (90% N_2 + 10% H_2).

5 Summary and outlook

In this work, the modulation structure of melilites and their phase behavior upon transition from the incommensurately modulated phase to the non-modulated normal phase, and from the incommensurate phase into the commensurate lock-in phase, was studied by various methods, such as electron microscopy, X-ray diffraction, X-ray microanalysis and calorimetry. The successful growth of single crystals with well defined chemical composition was a general precondition of these studies. Based on the structural investigations, experiments on the doping behavior and the optical properties of certain melilites were carried out. In summary, the experiments and the corresponding results are:

1. Using the floating zone melting technique, single crystals of about 3 mm diameter and lengths up to 50 mm could be grown out of the series $\text{Ca}_2\text{Mg}_{1-x}\text{Zn}_x\text{Si}_2\text{O}_7$, $\text{Ca}_2\text{Co}_{1-x}\text{Zn}_x\text{Si}_2\text{O}_7$, $(\text{Sr}_{1-x}\text{Ca}_x)_2\text{CoSi}_2\text{O}_7$ through the whole compositional range $0 \leq x \leq 1$. For the series $\text{Ca}_2\text{Mg}_{1-x}\text{Zn}_x\text{Si}_2\text{O}_7$ and $\text{Ca}_2\text{Co}_{1-x}\text{Zn}_x\text{Si}_2\text{O}_7$ it was found that the evaporation of Zn is the main factor that determines the crystal quality but that this factor can effectively be reduced by certain additives and under appropriate experimental conditions.
2. In the $\text{Ca}_2\text{Mg}_{1-x}\text{Zn}_x\text{Si}_2\text{O}_7$ system, the temperature of the incommensurate-to-normal phase transition T_{I-N} increases linearly with the increase of the ratio of $\text{Zn}/(\text{Mg} + \text{Zn})$ from 353K for $\text{Ca}_2\text{MgSi}_2\text{O}_7$ to 393K for $\text{Ca}_2\text{ZnSi}_2\text{O}_7$. An anomalous behavior was observed of the lattice parameters in dependence on the substitution of Mg by Zn as well as of Zn by Co within the system $\text{Ca}_2\text{Co}_{1-x}\text{Zn}_x\text{Si}_2\text{O}_7$. The reason of this behavior could not unequivocally be clarified within the scope of this work.
3. The normal as well as the incommensurately modulated structures within the $\text{Ca}_2\text{Mg}_{1-x}\text{Co}_x\text{Si}_2\text{O}_7$ system were studied in detail using high-resolution TEM and electron diffraction. The findings relating the average structure were in good agreement with the predictions of image simulation. The value of the modulation vector $|\mathbf{q}|$ as calculated from the corresponding diffraction patterns increases from 0.280 for $\text{Ca}_2\text{MgSi}_2\text{O}_7$ to 0.307 for $\text{Ca}_2\text{CoSi}_2\text{O}_7$. The observation

of one-dimensional and two-dimensional modulations at different areas indicates the existence of domains.

4. Different ordering schemes within the modulated structure and changes of the domain morphology were observed in the system $\text{Ca}_2\text{Co}_{1-x}\text{Zn}_x\text{Si}_2\text{O}_7$ in dependence on the Co/Zn compound ratio. The intensity of the diffuse scattering has been proved a clear indicator of short-range ordering associated with the incommensurate modulation. The occurrence of octagonal arrangements of T^I tetrahedra surrounded by six-coordinated Ca atoms could be confirmed by HRTEM observations. The transformation of the incommensurate into the commensurate phase (T_{1C}) and the associated domain evolution were observed up to a Zn concentration of 50%. The transition does not occur homogeneously over extended crystal areas at the same time but gets initiated at a great number of nucleation sites, and shows a prominent hysteresis. The domain formation is an expression of the release of misfit-induced internal stresses which increase toward low temperatures. The growing commensurate domains are separated by a network of discommensurations, but the complete commensurate phase has not been reached even at liquid helium temperature. The X-ray refinement has led to an orthorhombic space group $P2_12_12$ for the commensurate phase. The ordering scheme of the six-, seven- and eight-coordinated Ca environment seems to adopt a saw-tooth-like pattern of repetition moieties formed by characteristic rotations and distortions of the T^I tetrahedra. A clear description of these superstructures requires additional future investigations.
5. Refinements of the average structure of $(\text{Ca}_{1-x}\text{Sr}_x)_2\text{CoSi}_2\text{O}_7$ according to the XRD data at 100K as well as at 233K were performed. The normal-to-incommensurate phase transition of $(\text{Ca}_{0.7}\text{Sr}_{0.3})_2\text{CoSi}_2\text{O}_7$ was confirmed by observation of the weak satellite reflections at low temperature.
6. Doping experiments were performed of the end-members $\text{Ca}_2\text{MgSi}_2\text{O}_7$ and $\text{Ca}_2\text{CoSi}_2\text{O}_7$ using Cr and Eu. Low amounts of Cr^{4+} doping on the Si-sites could be reached in air atmosphere, and of Eu^{2+} on the Ca-sites at reduced atmosphere, however, the capability of doping became increasingly impeded by the

formation of foreign phases and of other valence states. The degree of doping achieved yielded a measurable but rather weak photoluminescence, however, further intense studies are needed to improve the optical emission of melilites for potential applications.

6 Zusammenfassung und Ausblick

In der vorliegenden Arbeit wurden die Modulationsstruktur und das Phasenumwandlungsverhalten beim Übergang von der inkomensurable modulierte Phase in die unmodulierte Normalphase und von der inkomensurablen in die komensurable lock-in Phase mit verschiedenen Methoden, vorrangig der Elektronenmikroskopie, der Röntgenbeugung, der Röntgenmikroanalyse und kalorimetrischen Methoden, untersucht. Grundvoraussetzung für diese Untersuchungen war das erfolgreiche Wachstum von Einkristallen definierter chemischer Zusammensetzung. Aufbauend auf den strukturellen Arbeiten wurden Untersuchungen zu den optischen Eigenschaften dotierter Melilite durchgeführt. Die Experimente und die daraus gewonnenen Erkenntnisse lassen sich wie folgt zusammenfassen:

1. In der Serie $\text{Ca}_2\text{Mg}_{1-x}\text{Zn}_x\text{Si}_2\text{O}_7$, $\text{Ca}_2\text{Co}_{1-x}\text{Zn}_x\text{Si}_2\text{O}_7$ und $(\text{Ca}_{1-x}\text{Sr}_x)_2\text{CoSi}_2\text{O}_7$ konnten im gesamten Bereich $0 \leq x \leq 1$ durch Floating-Zone-Technik Einkristalle mit Durchmessern von *ca.* 3 mm und Längen bis zu 50 mm hergestellt werden. Es wurde herausgefunden, dass der wesentliche qualitätsbestimmende Faktor die Verdampfung von Zn ist, dass dieser Effekt aber effektiv durch Hinzufügung verschiedener Additive sowie durch die Wahl geeigneter experimenteller Bedingungen minimiert werden kann.
2. Im System $\text{Ca}_2\text{Mg}_{1-x}\text{Zn}_x\text{Si}_2\text{O}_7$ steigt die Temperatur des Phasenumwandlungspunktes T_{I-N} von der normalen in die inkomensurable Phase mit dem Verhältnis $\text{Zn}/(\text{Mg} + \text{Zn})$ linear von 353K für $\text{Ca}_2\text{MgSi}_2\text{O}_7$ auf 393K für $\text{Ca}_2\text{ZnSi}_2\text{O}_7$ an. Es wurde ein anomaler Verlauf der Gitterparameter bei der Substitution von Mg durch Zn ebenso wie bei der Substitution von Zn durch Co im System $\text{Ca}_2\text{Co}_{1-x}\text{Zn}_x\text{Si}_2\text{O}_7$ beobachtet, die Ursache hierfür konnte im Rahmen dieser Arbeit nicht eindeutig geklärt werden.
3. Im System $\text{Ca}_2\text{Mg}_{1-x}\text{Co}_x\text{Si}_2\text{O}_7$ wurde sowohl die Normalstruktur als auch die inkomensurabel modulierte Struktur durch Hochauflösungs-TEM und Elektronenbeugung näher untersucht. Für die Normalstruktur wurde eine gute

Übereinstimmung mit den Vorhersagen aus der Bildsimulatuion gefunden. Der Betrag des Modulationsvektors $|q|$ wächst von 0.280 für $\text{Ca}_2\text{MgSi}_2\text{O}_7$ auf 0.307 für $\text{Ca}_2\text{CoSi}_2\text{O}_7$. Der Nachweis ein- und zwei-dimensionaler Modulationen in unterschiedlichen Probenbereichen deutet auf die Existenz von Domänen hin.

4. Im System $\text{Ca}_2\text{Co}_{1-x}\text{Zn}_x\text{Si}_2\text{O}_7$ wurden unterschiedliche Ordnungsstrukturen innerhalb der modulierten Struktur und Änderungen in der Domänenmorphologie in Abhängigkeit von dem Co/Zn-Verhältnis beobachtet. Die Intensität diffuser Beugung erwies sich als deutlicher Indikator für das Vorliegen kurzreichweitiger Ordnungserscheinungen in Zusammenhang mit der inkommensurablen Modulation. Eine bevorzugt oktagonale Anordnung der T^1 Tetraeder, die von sechsfach koordinierten Ca-Atomen umgeben sind, konnte durch HRTEM bestätigt werden. Die Umwandlung der inkommensurablen in die kommensurable Phase (T_{I-C}) und die damit verbundene Domänenentwicklung wurde bis zu einer Zn-Konzentration von 50% verfolgt. Sie erfolgt nicht gleichzeitig und homogen über den gesamten Kristall, sondern wird durch eine Vielzahl von Keimen initiiert, woraus sich das starke Hysterese-Verhalten erklärt. Die Domänenbildung ist Ausdruck der Freisetzung von Spannungen, die durch Fehlpassung zwischen den Tetraederschichten eingebaut werden und die sich zu tiefen Temperaturen hin verstärken. Die sich ausbreitenden kommensurablen Domänen sind dementsprechend durch ein Netzwerk von Diskommensurationen unterbrochen, eine komplette Phasenumwandlung wurde selbst bei der Temperatur flüssigen Heliums nicht erreicht. Die röntgenographische Verfeinerung ergab die orthorhombische Raumgruppe $P2_12_12$ für die kommensurable Phase. Das Ordnungsschema der sechs-, sieben- und acht-fach koordinierten Calcium-Umgebung scheint einem Sägezahn-förmigen Verlauf von Wiederholungseinheiten zu folgen, die durch charakteristische Rotationen und Deformationen der T^1 -Tetraeder bestimmt sind. Eine nähere Beschreibung dieser Überstrukturen wird erst nach weitergehenden zukünftigen Untersuchungen möglich sein.
5. Die Basisstruktur von $(\text{Ca}_{1-x}\text{Sr}_x)_2\text{CoSi}_2\text{O}_7$ wurde anhand der XRD-Daten für 100K and 233K verfeinert. Die Umwandlung von der Normalphase in die

inkommensurable Phase von $(\text{Ca}_{0.7}\text{Sr}_{0.3})_2\text{CoSi}_2\text{O}_7$ wurde durch Beobachtung der schwachen Satellit-Reflexe bei niedriger Temperatur bestätigt.

6. Dotierungs-Experimente mit Cr und Eu wurden an den Endgliedern $\text{Ca}_2\text{MgSi}_2\text{O}_7$ und $\text{Ca}_2\text{CoSi}_2\text{O}_7$ durchgeführt. Es konnte gezeigt werden, dass geringe Dotierungen mit Cr^{4+} auf den Si-Plätzen in Luft-Atmosphäre und von Eu^{2+} auf den Ca-Plätzen in reduzierter Atmosphäre möglich sind, jedoch durch die Ausbildung von Fremdphasen und anderen Valenz-Zuständen begrenzt werden. Die erzielten Dotierungen ergaben eine schwache, nachweisbare Photolumineszenz, eine Verbesserung der optischen Emission der Melilite für mögliche zukünftige Anwendungen erfordert jedoch weitere intensive Untersuchungen.

7 References

- [1] R. Comes, G. Shirane, S. M. Shapiro, A. F. Garito, A. J. Heeger, *Physical Review B* **1976**, *14*, 2376.
- [2] S. V. Dmitriev, T. Shigenari, K. Abe, *Ferroelectrics* **1998**, *217*, 179.
- [3] R. Portier, D. Gratias, *Acta Crystallographica Section A-Foundations of Crystallography* **1980**, *36*, 190.
- [4] B. S. Hemingway, H. T. Evans, G. L. Nord, H. T. Haselton, R. A. Robie, J. J. Mcgee, *Canadian Mineralogist* **1986**, *24*, 425.
- [5] F. Seifert, M. Czank, B. Simons, W. Schmahl, *Physics and Chemistry of Minerals* **1987**, *14*, 26.
- [6] I. U. Heimann, J. D. Axe, J. M. Hastings, G. Shirane, *Physical Review B* **1979**, *20*, 751.
- [7] F. Röthlisberger, F. Seifert, M. Czank, *European Journal of Mineralogy* **1990**, *2*, 585.
- [8] K. Iishi, K. Fujino, Y. Furukawa, *Physics and Chemistry of Minerals* **1990**, *17*, 720.
- [9] J. C. Jiang, M. Schosnig, A. K. Schaper, K. Ganster, H. Rager, L. Toth, *Physics and Chemistry of Minerals* **1998**, *26*, 128.
- [10] H. Böhm, *American Mineralogist* **1983**, *68*, 11.
- [11] M. Schosnig, A. K. Schaper, A. Kutoglu, W. Treutmann, H. Rager, *Zeitschrift für Kristallographie* **2000**, *215*, 495.
- [12] K. Hagiya, M. Ohmasa, *Acta Crystallographica Section B-Structural Science* **1993**, *49*, 172.
- [13] N. E. Brown, C. R. Ross, S. L. Webb, *Physics and Chemistry of Minerals* **1994**, *21*, 469.
- [14] T. Tamura, A. Yoshiasa, K. Iishi, S. Takeno, H. Maeda, S. Emura, K. Koto, *Physics and Chemistry of Minerals* **1996**, *23*, 81.
- [15] B. Bagautdinov, K. Hagiya, K. Kusaka, M. Ohmasa, K. Iishi, *Acta Crystallographica Section B-Structural Science* **2000**, *56*, 811.
- [16] M. Rießer, H. Böhm, V. Petricek, *Zeitschrift für Kristallographie* **2000**, *215*, 102.
- [17] L. Bindi, P. Bonazzi, M. Dusek, V. Petricek, G. Chapuis, *Acta Crystallographica Section B-Structural Science* **2001**, *57*, 739.
- [18] K. Kusaka, M. Ohmasa, K. Hagiya, K. Iishi, N. Haga, *Mineralogical Journal* **1998**, *20*, 47.
- [19] K. Kusaka, K. Hagiya, M. Ohmasa, Y. Okano, M. Mukai, K. Iishi, N. Haga, *Physics and Chemistry of Minerals* **2001**, *28*, 150.
- [20] P. Le Boulanger, J. L. Doualan, S. Girard, J. Margerie, R. Moncorge, B. Viana, *Journal of Luminescence* **2000**, *86*, 15.
- [21] J. P. Foing, E. Scheer, B. Viana, N. Britos, *Applied Optics* **1998**, *37*, 4857.
- [22] N. Kodama, T. Takahashi, M. Yamaga, Y. Tanii, J. Qiu, K. Hirao, *Applied Physics Letters* **1999**, *75*, 1715.
- [23] M. Yamaga, Y. Tanii, N. Kodama, T. Takahashi, M. Honda, *Physical Review B* **2002**, *65*, 235108.
- [24] L. Jiang, C. K. Chang, D. L. Mao, *Journal of Alloys and Compounds* **2003**, *360*, 193.
- [25] T. Janssen, A. Janner, *Advances in Physics* **1987**, *36*, 519.
- [26] B. E. Warren, *Zeitschrift für Kristallographie* **1930**, *74*, 131.

- [27] J. V. Smith, *American Mineralogist* **1953**, 38, 643.
- [28] C. V. Heurck, G. V. Tendeloo, S. Amelinckx, *Physics and Chemistry of Minerals* **1992**, 18, 441.
- [29] M. Riestler, H. Böhm, *Zeitschrift für Kristallographie* **1997**, 212, 506.
- [30] A. K. Schaper, M. Schosnig, A. Kutoglu, W. Treutmann, H. Rager, *Acta Crystallographica Section B-Structural Science* **2001**, 57, 443.
- [31] L. H. Merwin, A. Sebald, F. Seifert, *Physics and Chemistry of Minerals* **1989**, 16, 752.
- [32] F. Seifert, *Carn. Inst. Washington Year Book* **1974**, 73, 500.
- [33] H. Ito, S. S. Hafner, *American Mineralogist* **1974**, 59, 700.
- [34] P. M. Wolff, *Acta Crystallographica Section A-Foundations of Crystallography* **1974**, 30, 777.
- [35] A. Yamamoto, 1 ed., Sakura mura, **1984**.
- [36] K. Kusaka, Doctorate Thesis, Himeji Institute of Technology, Himeji, **1999**.
- [37] K. Kusaka, K. Hagiya, M. Ohmasa, K. Iishi, *Ferroelectrics* **2001**, 250, 79.
- [38] W. Heywang, *Zeitschrift für Naturforsch* **1956**, 11a, 238.
- [39] P. Buseck, J. Cowley, L. Eyring, *High-resolution Transmission Electron Microscopy and Associated Techniques*, Second ed., Oxford University Press, New York, **1992**.
- [40] J. C. H. Spence, *High-resolution Electron Microscopy*, 3rd ed., Clarendon Press, **2003**.
- [41] D. Shindo, K. Hiraga, *High-resolution Electron Microscopy for Materials Science*, Springer, Tokyo, **1998**.
- [42] D. L. Dorset, *Structural Electron Crystallography*, Plenum Press, New York, **1995**.
- [43] J. M. Cowley, A. F. Moodie, *Acta Crystallographica Section A-Foundations of Crystallography* **1959**, 12, 360.
- [44] M. J. Buerger, *The Precession Method in X-ray Crystallography*, John Wiley and Sons. Inc., New York, **1964**.
- [45] A. S. Marfunin, *Spectroscopy, Luminescence and Radiation Centers in Minerals*, Springer-Verlag, Berlin, **1979**.
- [46] G. Liptay, *Atlas of Thermoanalytical Curves*, **1971**.
- [47] W. Krause, G. Nolze, 2.4 ed., Berlin, **2000**.
- [48] J. Liebertz, S. Stähr, *Zeitschrift für Kristallographie* **1982**, 159, 271.
- [49] K. Iishi, K. Fujimoto, Yamaguchi, K. Fujino, Ehime, *Newes Jahrbuch für Mineralogie* **1989**, 5, 219.
- [50] W. Bardsley, F. C. Frank, G. W. Green, D. T. J. Hurle, *Journal of Crystal Growth* **1974**, 23, 341.
- [51] M. Pokoj, Diploma work, Philipps University, Marburg, **2003**.
- [52] R. A. Cowley, in *Monographs on Physics: Structural Phase Transitions* (Ed.: B. R. Coles), Taylor & Francis Ltd., London, **1981**, pp. 1.
- [53] K. Iishi, T. Mizota, K. Fujino, Y. Furukawa, *Physics and Chemistry of Minerals* **1991**, 17, 720.
- [54] S. J. Louisnathan, *Zeitschrift für Kristallographie* **1969**, 130, 427.
- [55] J. Kusz, H. Böhm, *Zeitschrift für Kristallographie* **2001**, 216, 509.
- [56] K. Hagiya, K. Kusaka, M. Ohmasa, K. Iishi, *Acta Crystallographica Section B-Structural Science* **2001**, 57, 271.
- [57] A. K. Schaper, Z. H. Jia, T. Ogawa, M. Tsuji, Nanotechnology Support Project, Institute for Chemical Research, Kyoto, **2004**.
- [58] W. L. McMillan, *Physics Review B* **1976**, 14, 1496.

-
- [59] P. M. Chaikin, T. C. Lubensky, *Principles of Condensed Matter Physics*, Cambridge University Press, **1997**.
- [60] J. C. Jiang, X. D. Zou, in *International Conference of Electron Microscopy*, Paris, **1994**, pp. 745.
- [61] P. Hirsch, A. Howie, R. Nicholson, D. W. Pashley, M. J. Whelan, *Electron microscopy of thin crystals*, second ed., Krieger, **1977**.
- [62] J. P. Hirth, J. Lothe, *Theory of dislocations*, New York Wiley, **1982**.
- [63] J. D. C. McConnell, *Zeitschrift für Kristallographie* **1999**, 214, 457.
- [64] K. Kusaka, K. Hagiya, M. Ohmasa, K. Iishi, *Acta Crystallographica Section B-Structural Science* **2004**, 60, 369.
- [65] V. Petricevic, S. K. Gayen, R. R. Alfano, K. Yamagishi, H. Anzai, Y. Yamaguchi, *Applied Physics Letters* **1988**, 52, 1040.
- [66] M. H. Garret, V. H. Chan, H. P. Jenssen, M. H. Whitemore, A. Sacra, D. J. Singel, in *Proceedings Advance Solid State Lasers, Vol. 10* (Eds.: G. Dube, L. Chase), Washington, **1991**, pp. 76.
- [67] T. H. Allik, B. H. T. Chai, L. D. Merkle, *Proceedings Advance Solid State Lasers* **1991**, 84.
- [68] C. Deka, M. Bass, B. H. T. Chai, X. X. Zang, *Proceedings Advance Solid State Lasers* **1992**, 47.
- [69] T. Ishii, K. Fujimura, K. Ogasawara, H. Adachi, I. Tanaka, *Journal of Physics: Condensed Matter* **2001**, 13, 5757.
- [70] A. Sugimoto, Y. Nobe, T. Yamazaki, Y. Anzai, K. Yamagishi, Y. Segawa, H. Takei, *Physics and Chemistry of Minerals* **1997**, 24, 326.
- [71] Y. H. Lin, Z. T. Zhang, Z. L. Tang, X. X. Wang, J. Y. Zhang, Z. S. Zheng, *Journal of the European Ceramic Society* **2001**, 21, 683.
- [72] K. Yamazaki, H. Nakabayashi, Y. Kotera, A. Ueno, *Journal of Electrochemistry Society* **1986**, 133, 657.
- [73] N. Kodama, N. Sasaki, M. Yamaga, Y. Masui, *Journal of Luminescence* **2001**, 94, 19.

Appendix A. Lock-in phase of $\text{Ca}_2(\text{Co}_{0.9}\text{Zn}_{0.1})\text{Si}_2\text{O}_7$ refined in s. g. $P2_12_12$.

Table 1 Crystal data and measurement conditions.

Empirical formula	$\text{Ca}_2 \text{Co}_{0.90} \text{Zn}_{0.10} \text{Si}_2 \text{O}_7$	
Formula weight	307.91	
Temperature	190(2) K	
Wavelength	0.71073 Å	
Crystal system	Orthorhombic	
Space group	$P2_12_12$	
Unit cell dimensions	$a = 23.518(1)$ Å	$\alpha = 90^\circ$.
	$b = 23.518(1)$ Å	$\beta = 90^\circ$.
	$c = 5.0263(3)$ Å	$\gamma = 90^\circ$.
Volume	$2780.0(2)$ Å ³	
Z	18	
Density (calculated)	3.311 Mg/m ³	
Absorption coefficient	4.935 mm ⁻¹	
F(000)	2723	
Crystal size	$0.15 \times 0.12 \times 0.02$ mm ³	
Theta range for data collection	1.94 to 31.21° .	
Index ranges	$-31 \leq h \leq 32$, $-33 \leq k \leq 33$, $-7 \leq l \leq 7$	
Reflections collected	25016	
Independent reflections	8340 [R(int) = 0.0775]	
Completeness to theta = 31.21°	92.5 %	
Absorption correction	Semi-empirical from equivalents	
Max. and min. transmission	0.814 and 0.567	
Refinement method	Full-matrix least-squares on F ²	
Data / restraints / parameters	8340 / 0 / 332	
Goodness-of-fit on F ²	1.051	
Final R indices [I > 2σ(I)]	R1 = 0.0605, wR2 = 0.1422	
R indices (all data)	R1 = 0.0827, wR2 = 0.1559	
Absolute structure parameter	-0.01(2)	
Extinction coefficient	0.0016(2)	
Largest diff. peak and hole	1.407 and -1.118 e.Å ⁻³	

Table 2 Atomic coordinates ($\times 10^4$) and equivalent isotropic displacement parameters (Å² $\times 10^3$). U(eq) is defined as one third of the trace of the orthogonalized U^{ij} tensor.

	x	y	z	U(eq)
Co(1)	0	0	-57(7)	14(1)
Co(2)	66(1)	3361(1)	68(5)	14(1)
Co(3)	1634(1)	1616(1)	104(5)	14(1)
Co(4)	3335(1)	21(1)	96(5)	14(1)
Co(5)	3347(1)	3304(1)	42(6)	14(1)
Zn(1)	0	0	-57(7)	14(1)
Zn(2)	66(1)	3361(1)	68(5)	14(1)
Zn(3)	1634(1)	1616(1)	104(5)	14(1)
Zn(4)	3335(1)	21(1)	96(5)	14(1)
Zn(5)	3347(1)	3304(1)	42(6)	14(1)
Ca(1)	1082(1)	536(1)	5003(7)	16(1)

Appendix

Ca(2)	1151(1)	3920(1)	4894(5)	17(1)
Ca(3)	550(1)	2251(1)	4988(6)	16(1)
Ca(4)	2754(1)	1112(1)	5102(6)	16(1)
Ca(5)	2691(1)	4506(1)	4758(6)	17(1)
Ca(6)	2156(1)	2659(1)	5210(5)	18(1)
Ca(7)	4415(1)	527(1)	5218(5)	18(1)
Ca(8)	4503(1)	3974(1)	5134(7)	17(1)
Ca(9)	4012(1)	2127(1)	4956(6)	18(1)
Si(1)	424(2)	1209(2)	-738(8)	14(1)
Si(2)	491(2)	4561(2)	-813(7)	14(1)
Si(3)	1256(2)	2857(2)	661(8)	14(1)
Si(4)	2125(2)	415(2)	740(8)	13(1)
Si(5)	2149(2)	3819(2)	464(8)	14(1)
Si(6)	2833(2)	2097(2)	-435(7)	14(1)
Si(7)	3811(2)	1232(2)	-531(7)	13(1)
Si(8)	3828(2)	4516(2)	-505(9)	14(1)
Si(9)	4554(2)	2803(2)	587(9)	15(1)
O(1)	-79(4)	1648(3)	8189(19)	16(2)
O(2)	1737(4)	-139(3)	1804(16)	16(2)
O(3)	1784(3)	3268(3)	1700(13)	16(1)
O(4)	3386(4)	1752(4)	8390(17)	21(2)
O(5)	5000	0	1990(20)	20(2)
O(6)	426(4)	1188(4)	2430(20)	23(2)
O(7)	504(4)	4576(4)	2385(15)	17(2)
O(8)	1232(4)	2821(4)	7543(19)	22(2)
O(9)	2158(4)	431(4)	7525(18)	19(2)
O(10)	2096(4)	3843(4)	7251(18)	18(2)
O(11)	2778(3)	2037(3)	2716(14)	16(2)
O(12)	3849(4)	1223(4)	2630(15)	16(2)
O(13)	3867(4)	4585(3)	2630(18)	19(2)
O(14)	4612(4)	2758(4)	7479(18)	22(2)
O(15)	248(4)	626(4)	7730(19)	20(2)
O(16)	991(4)	1426(3)	7786(17)	17(2)
O(17)	335(4)	3964(3)	7743(17)	19(2)
O(18)	1048(4)	4792(3)	7610(17)	18(2)
O(19)	1382(4)	2263(4)	2201(18)	20(2)
O(20)	708(3)	3118(3)	2211(16)	15(2)
O(21)	1832(4)	951(4)	2298(16)	19(2)
O(22)	2716(3)	291(3)	2350(16)	14(2)
O(23)	1865(3)	4361(3)	2073(16)	14(2)
O(24)	2785(4)	3778(3)	1730(16)	22(2)
O(25)	2878(3)	2725(3)	8294(14)	16(1)
O(26)	2306(3)	1799(4)	7983(16)	18(2)
O(27)	3558(4)	675(4)	7935(18)	17(2)
O(28)	4408(3)	1374(3)	7899(16)	16(2)
O(29)	3796(3)	3889(3)	8241(14)	18(2)
O(30)	4345(4)	4816(4)	7821(18)	18(2)
O(31)	4834(3)	2265(3)	2222(17)	17(2)
O(32)	3924(3)	2847(3)	1782(16)	19(2)

Appendix

Table 3 Bond lengths [\AA].

Ca(1)-O(15)	2.402(10)	Ca(2)-O(17)	2.396(9)	Ca(3)-O(19)	2.407(9)
Ca(1)-O(30)	2.427(9)	Ca(2)-O(23)	2.431(9)	Ca(3)-O(8)	2.452(10)
Ca(1)-O(21)	2.431(9)	Ca(2)-O(18)	2.474(9)	Ca(3)-O(31)	2.469(9)
Ca(1)-O(16)	2.527(9)	Ca(2)-O(7)	2.507(8)	Ca(3)-O(20)	2.499(8)
Ca(1)-O(6)	2.532(11)	Ca(2)-O(10)	2.525(9)	Ca(3)-O(14)	2.530(9)
Ca(1)-O(13)	2.536(9)	Ca(2)-O(20)	2.542(8)	Ca(3)-O(1)	2.605(9)
Ca(1)-O(2)	2.734(9)	Ca(2)-O(3)	2.674(8)	Ca(3)-O(16)	2.610(9)
Ca(1)-O(9)	2.842(9)	Ca(2)-O(8)	2.915(10)	Ca(3)-O(6)	2.827(11)
Mean	2.554(9)	Mean	2.558(9)	Mean	2.550(9)
Ca(4)-O(22)	2.378(8)	Ca(5)-O(24)	2.301(8)	Ca(6)-O(25)	2.304(7)
Ca(4)-O(26)	2.411(9)	Ca(5)-O(2)	2.344(8)	Ca(6)-O(11)	2.419(8)
Ca(4)-O(9)	2.453(9)	Ca(5)-O(23)	2.390(8)	Ca(6)-O(3)	2.435(8)
Ca(4)-O(11)	2.485(8)	Ca(5)-O(10)	2.443(10)	Ca(6)-O(26)	2.482(9)
Ca(4)-O(27)	2.581(9)	Ca(5)-O(9)	2.483(9)	Ca(6)-O(8)	2.498(11)
Ca(4)-O(21)	2.614(9)	Ca(5)-O(22)	2.536(8)	Ca(6)-O(19)	2.543(9)
Ca(4)-O(4)	2.685(10)	Ca(5)-O(13)	2.970(9)	Ca(6)-O(10)	2.969(9)
Ca(4)-O(12)	2.871(9)				
Mean	2.560(9)	Mean	2.495(9)	Mean	2.521(9)
Ca(7)-O(28)	2.404(9)	Ca(8)-O(29)	2.291(8)	Ca(9)-O(32)	2.336(8)
Ca(7)-O(27)	2.459(9)	Ca(8)-O(30)	2.425(9)	Ca(9)-O(31)	2.394(9)
Ca(7)-O(5)	2.464(8)	Ca(8)-O(13)	2.426(9)	Ca(9)-O(14)	2.410(9)
Ca(7)-O(12)	2.478(8)	Ca(8)-O(1)	2.428(9)	Ca(9)-O(4)	2.433(10)
Ca(7)-O(18)	2.490(9)	Ca(8)-O(15)	2.454(10)	Ca(9)-O(12)	2.455(9)
Ca(7)-O(7)	2.548(9)	Ca(8)-O(6)	2.522(11)	Ca(9)-O(28)	2.488(9)
Ca(7)-O(7)	2.840(10)	Ca(8)-O(14)	3.104(9)	Ca(9)-O(11)	3.121(8)
Ca(7)-O(17)	2.887(9)				
Mean	2.571(9)	Mean	2.521(9)	Mean	2.520(9)
Si(1)-O(6)	1.591(12)	Si(2)-O(7)	1.608(8)	Si(3)-O(8)	1.571(11)
Si(1)-O(16)	1.610(9)	Si(2)-O(17)	1.622(9)	Si(3)-O(19)	1.625(10)
Si(1)-O(15)	1.626(10)	Si(2)-O(18)	1.626(9)	Si(3)-O(20)	1.626(9)
Si(1)-O(1)	1.659(8)	Si(2)-O(5)	1.658(5)	Si(3)-O(3)	1.659(8)
Mean	1.622(10)	Mean	1.629(8)	Mean	1.620(10)
Si(4)-O(9)	1.619(10)	Si(5)-O(10)	1.621(10)	Si(6)-O(11)	1.596(8)
Si(4)-O(22)	1.634(9)	Si(5)-O(24)	1.627(9)	Si(6)-O(25)	1.612(8)
Si(4)-O(21)	1.637(9)	Si(5)-O(23)	1.652(9)	Si(6)-O(26)	1.630(9)
Si(4)-O(2)	1.678(9)	Si(5)-O(3)	1.673(8)	Si(6)-O(4)	1.644(9)
Mean	1.642(9)	Mean	1.643(9)	Mean	1.621(9)
Si(7)-O(12)	1.592(9)	Si(8)-O(13)	1.587(10)	Si(9)-O(14)	1.572(10)
Si(7)-O(27)	1.633(9)	Si(8)-O(29)	1.604(8)	Si(9)-O(32)	1.602(9)
Si(7)-O(28)	1.645(9)	Si(8)-O(30)	1.640(10)	Si(9)-O(31)	1.647(9)
Si(7)-O(4)	1.670(9)	Si(8)-O(2)	1.688(9)	Si(9)-O(1)	1.671(9)
Mean	1.635(9)	Mean	1.630(9)	Mean	1.623(9)
Co,Zn(1)-O(15)	1.935(9)	Co,Zn(2)-O(20)	1.942(8)		

Appendix

Co,Zn(1)-O(15)	1.935(9)	Co,Zn(2)-O(17)	1.943(9)
Co,Zn(1)-O(30)	1.954(9)	Co,Zn(2)-O(31)	1.946(9)
Co,Zn(1)-O(30)	1.954(9)	Co,Zn(2)-O(28)	1.955(8)
Mean	1.945(9)	Mean	1.947(9)
Co,Zn(3)-O(19)	1.944(9)	Co,Zn(4)-O(18)	1.930(9)
Co,Zn(3)-O(26)	1.956(8)	Co,Zn(4)-O(22)	1.951(8)
Co,Zn(3)-O(16)	1.961(9)	Co,Zn(4)-O(27)	1.955(9)
Co,Zn(3)-O(21)	1.970(8)	Co,Zn(4)-O(23)	1.955(8)
Mean	1.958(9)	Mean	1.948(9)
Co,Zn(5)-O(24)	1.927(8)	Co,Zn(5)-O(25)	1.962(7)
Co,Zn(5)-O(32)	1.940(8)	Mean	1.947(9)
Co,Zn(5)-O(29)	1.956(7)		

Table 4 Anisotropic displacement parameters ($\text{\AA}^2 \times 10^3$) according to $P2_12_12$. The anisotropic displacement factor exponent takes the form: $-2\pi^2 [h^2 a^{*2} U^{11} + \dots + 2 h k a^* b^* U^{12}]$.

	U11	U22	U33	U23	U13	U12
Co(1)	14(1)	10(1)	18(1)	0	0	-2(1)
Co(2)	14(1)	11(1)	18(1)	1(1)	-1(1)	-1(1)
Co(3)	13(1)	11(1)	18(1)	-1(1)	1(1)	1(1)
Co(4)	13(1)	11(1)	18(1)	0(1)	0(1)	-1(1)
Co(5)	12(1)	10(1)	21(1)	1(1)	-1(1)	0(1)
Zn(1)	14(1)	10(1)	18(1)	0	0	-2(1)
Zn(2)	14(1)	11(1)	18(1)	1(1)	-1(1)	-1(1)
Zn(3)	13(1)	11(1)	18(1)	-1(1)	1(1)	1(1)
Zn(4)	13(1)	11(1)	18(1)	0(1)	0(1)	-1(1)
Zn(5)	12(1)	10(1)	21(1)	1(1)	-1(1)	0(1)
Ca(1)	16(1)	14(1)	17(1)	-2(1)	0(1)	1(1)
Ca(2)	14(1)	16(1)	20(1)	-1(1)	1(1)	1(1)
Ca(3)	16(1)	15(1)	16(1)	2(1)	0(1)	-2(1)
Ca(4)	16(1)	13(1)	20(1)	0(1)	-1(1)	-1(1)
Ca(5)	19(1)	13(1)	19(1)	-1(1)	1(1)	-2(1)
Ca(6)	15(1)	19(1)	19(1)	0(1)	1(1)	2(1)
Ca(7)	18(1)	14(1)	22(1)	0(1)	0(1)	2(1)
Ca(8)	16(1)	19(1)	17(1)	-1(1)	1(1)	3(1)
Ca(9)	19(1)	13(1)	21(1)	2(1)	-1(1)	-2(1)
Si(1)	12(2)	14(2)	15(2)	0(1)	0(1)	0(1)
Si(2)	11(1)	13(2)	16(1)	0(1)	-1(1)	0(1)
Si(3)	10(2)	16(2)	16(2)	-2(1)	1(1)	-1(1)
Si(4)	10(1)	15(2)	15(2)	1(1)	2(1)	0(1)
Si(5)	10(1)	13(1)	19(2)	0(1)	-2(1)	0(1)
Si(6)	9(1)	16(2)	16(1)	2(1)	-1(1)	0(1)
Si(7)	10(1)	11(1)	18(1)	1(1)	1(1)	2(1)
Si(8)	11(1)	16(1)	15(2)	0(1)	0(1)	0(1)
Si(9)	12(2)	14(1)	19(2)	1(1)	-1(1)	-2(1)

Appendix B. Lock-in phase of $\text{Ca}_2(\text{Co}_{0.9}\text{Zn}_{0.1})\text{Si}_2\text{O}_7$ refined in s. g. $P\bar{4}$.

Table 1 Crystal data and structure refinement.

Identification code	p-4	
Empirical formula	$\text{Ca}_2 \text{Co}_{0.90} \text{O}_7 \text{Si}_2 \text{Zn}_{0.10}$	
Formula weight	307.91	
Temperature	190(2) K	
Wavelength	0.71073 Å	
Crystal system	tetragonal	
Space group	$P\bar{4}$	
Unit cell dimensions	$a = 23.5180(10)$ Å	$\alpha = 90^\circ$.
	$b = 23.5180(10)$ Å	$\beta = 90^\circ$.
	$c = 5.0263(3)$ Å	$\gamma = 90^\circ$.
Volume	$2780.0(2)$ Å ³	
Z	18	
Density (calculated)	3.311 Mg/m ³	
Absorption coefficient	4.935 mm ⁻¹	
F(000)	2723	
Crystal size	0.15 x 0.12 x 0.02 mm ³	
Theta range for data collection	1.94 to 31.21°.	
Index ranges	$-31 \leq h \leq 32$, $-33 \leq k \leq 33$, $-7 \leq l \leq 7$	
Reflections collected	25012	
Independent reflections	8488 [R(int) = 0.0776]	
Completeness to theta = 31.21°	94.5 %	
Absorption correction	Semi-empirical from equivalents	
Max. and min. transmission	0.814 and 0.567	
Refinement method	Full-matrix least-squares on F ²	
Data / restraints / parameters	8488 / 0 / 331	
Goodness-of-fit on F ²	1.113	
Final R indices [$I > 2\sigma(I)$]	R1 = 0.0758, wR2 = 0.1751	
R indices (all data)	R1 = 0.1011, wR2 = 0.1948	
Absolute structure parameter	0.00(3)	
Extinction coefficient	0.0048(4)	
Largest diff. peak and hole	1.497 and -1.198 e.Å ⁻³	

Table 2 Atomic coordinates ($\times 10^4$) and equivalent isotropic displacement parameters (Å² $\times 10^3$) for $P\bar{4}$. U(eq) is defined as one third of the trace of the orthogonalized U_{ij} tensor.

	x	y	z	U(eq)
Ca(1)	1146(2)	3973(2)	5275(7)	30(1)
Ca(2)	1105(1)	573(1)	4985(7)	21(1)
Ca(3)	4523(1)	656(1)	4916(7)	28(1)
Ca(4)	7803(2)	608(2)	5128(8)	36(1)
Ca(5)	4334(1)	3808(1)	5181(6)	10(1)*
Ca(6)	-2219(1)	3899(1)	5064(8)	19(1)
Ca(7)	1187(1)	7307(2)	5179(7)	26(1)
Ca(8)	-5602(1)	7194(1)	4942(7)	13(1)

Appendix

Ca(9)	-2222(1)	7215(1)	5002(7)	20(1)
Co(1)	0	0	0	29(1)
Co(2)	3366(1)	26(1)	-9(5)	19(1)
Co(3)	3287(1)	3302(1)	39(4)	15(1)
Co(4)	1639(1)	1685(1)	-122(4)	15(1)
Co(5)	4994(1)	1716(1)	-29(6)	18(1)
Co(6)	5000	5000	0	17(1)
Zn(1)	0	0	0	29(1)
Zn(2)	3366(1)	26(1)	-9(5)	19(1)
Zn(3)	3287(1)	3302(1)	39(4)	15(1)
Zn(4)	1639(1)	1685(1)	-122(4)	15(1)
Zn(5)	4994(1)	1716(1)	-29(6)	18(1)
Zn(6)	5000	5000	0	17(1)
Si(1)	492(2)	4569(2)	9520(7)	13(1)
Si(2)	435(2)	1222(2)	9346(10)	20(1)
Si(3)	-509(2)	2136(2)	9588(10)	20(1)
Si(4)	3824(2)	1221(2)	9321(9)	25(1)
Si(5)	-2862(2)	7882(2)	9263(7)	13(1)
Si(6)	7124(2)	1152(2)	9380(9)	17(1)
Si(7)	6226(2)	2108(2)	9235(9)	18(1)
Si(8)	3792(2)	4487(2)	9548(10)	15(1)
Si(9)	2936(2)	5483(2)	9333(9)	15(1)
O(1)	0	5000	8400(40)	39(4)
O(2)	538(4)	4600(4)	12810(20)	26(2)
O(3)	404(6)	3934(6)	8310(30)	48(3)
O(4)	1060(4)	4775(4)	7987(19)	18(2)
O(5)	28(8)	1751(7)	8300(50)	61(5)
O(7)	6639(4)	1586(4)	8177(19)	21(2)
O(8)	3466(3)	5063(3)	8342(15)	6(1)
O(6)	3289(4)	1600(4)	8080(20)	17(2)
O(24)	5605(4)	1977(4)	7641(19)	18(2)
O(18)	-2858(4)	7871(4)	12450(20)	19(2)
O(26)	6217(6)	2116(6)	12300(30)	35(3)
O(21)	7124(6)	1220(6)	12630(30)	43(3)
O(31)	2919(3)	5528(4)	12479(18)	12(2)
O(27)	3718(3)	4441(3)	12632(16)	11(1)
O(32)	3049(4)	6065(4)	7837(19)	14(2)
O(20)	-3072(4)	7323(4)	7830(20)	18(2)
O(15)	4394(4)	1495(4)	7704(19)	18(2)
O(30)	2381(3)	5199(3)	7829(16)	9(1)
O(25)	6484(4)	2639(4)	7760(20)	20(2)
O(13)	-516(5)	2120(5)	12660(30)	29(2)
O(19)	-2263(4)	8076(4)	7643(18)	17(2)
O(11)	457(4)	1216(4)	12530(20)	18(2)
O(17)	3885(4)	1275(4)	12468(19)	23(2)
O(12)	-1035(4)	1849(4)	7830(20)	19(2)
O(29)	3476(4)	3964(4)	7892(18)	14(2)
O(10)	1017(4)	1401(4)	7640(20)	21(2)
O(28)	4425(3)	4521(3)	8280(15)	9(1)
O(16)	3782(4)	609(4)	8098(19)	24(2)
O(22)	7675(5)	1446(5)	7870(30)	36(3)
O(9)	197(5)	692(6)	7840(30)	39(3)
O(23)	7099(5)	546(5)	8310(20)	34(2)
O(14)	-434(5)	2765(5)	8130(20)	33(2)

* non positive definite

Appendix

Table 3 Bond lengths [Å].

Ca(1)-O(3)	2.320(14)	Ca(8)-O(27)#17	2.471(8)
Ca(1)-O(4)	2.337(10)	Ca(8)-O(26)#10	2.547(15)
Ca(1)-O(2)#1	2.399(11)	Ca(8)-O(25)#8	2.543(10)
Ca(1)-O(7)#2	2.480(10)	Ca(8)-O(30)#16	2.547(8)
Ca(1)-O(26)#3	2.624(14)	Ca(8)-O(8)#16	2.753(8)
Ca(1)-O(24)#2	2.638(10)	Ca(8)-O(31)#17	2.968(9)
Ca(1)-O(21)#3	2.792(15)	Ca(9)-O(25)#9	2.419(10)
Ca(2)-O(10)	2.371(10)	Ca(9)-O(19)	2.423(9)
Ca(2)-O(11)#1	2.477(11)	Ca(9)-O(20)	2.467(10)
Ca(2)-O(9)#4	2.497(13)	Ca(9)-O(18)#1	2.502(10)
Ca(2)-O(12)#4	2.501(10)	Ca(9)-O(22)#9	2.566(13)
Ca(2)-O(9)	2.586(13)	Ca(9)-O(7)#9	2.574(10)
Ca(2)-O(5)#4	2.65(2)	Ca(9)-O(21)#11	2.649(15)
Ca(2)-O(13)#5	2.669(12)	Ca(9)-O(26)#11	2.722(14)
Ca(2)-O(11)#5	2.736(10)	Co(1)-O(9)#18	2.011(13)
Ca(3)-O(16)	2.367(10)	Co(1)-O(9)#4	2.011(13)
Ca(3)-O(2)#6	2.375(11)	Co(1)-O(9)#1	2.011(13)
Ca(3)-O(4)#7	2.399(10)	Co(1)-O(9)#9	2.011(13)
Ca(3)-O(17)#1	2.425(10)	Co(2)-O(3)#4	1.880(14)
Ca(3)-O(15)	2.439(10)	Co(2)-O(23)#19	1.929(11)
Ca(3)-O(1)#4	2.533(13)	Co(2)-O(16)#1	1.934(10)
Ca(3)-O(2)#5	3.039(11)	Co(2)-O(14)#4	1.952(11)
Ca(4)-O(23)	2.306(12)	Co(3)-O(20)#10	1.909(10)
Ca(4)-O(22)	2.423(13)	Co(3)-O(29)#1	1.945(9)
Ca(4)-O(5)#7	2.43(2)	Co(3)-O(25)#2	1.948(10)
Ca(4)-O(21)#1	2.489(16)	Co(3)-O(32)#7	1.955(10)
Ca(4)-O(10)#7	2.525(11)	Co(4)-O(19)#10	1.932(9)
Ca(4)-O(11)#6	2.615(10)	Co(4)-O(22)#2	1.938(13)
Ca(4)-O(13)#6	2.874(12)	Co(4)-O(10)#1	1.962(10)
Ca(5)-O(28)	2.298(8)	Co(4)-O(12)#4	1.977(10)
Ca(5)-O(8)#7	2.407(8)	Co(5)-O(15)#1	1.886(10)
Ca(5)-O(31)#6	2.421(9)	Co(5)-O(4)#7	1.930(10)
Ca(5)-O(27)#1	2.439(8)	Co(5)-O(24)#1	1.954(10)
Ca(5)-O(29)	2.463(9)	Co(5)-O(30)#7	1.967(8)
Ca(5)-O(32)#7	2.524(10)	Co(6)-O(28)#1	1.961(8)
Ca(5)-O(27)#6	3.091(8)	Co(6)-O(28)#20	1.961(8)
Ca(6)-O(32)#8	2.400(10)	Co(6)-O(28)#2	1.961(8)
Ca(6)-O(15)#9	2.488(10)	Co(6)-O(28)#7	1.961(8)
Ca(6)-O(31)#10	2.495(9)	Si(1)-O(4)	1.616(10)
Ca(6)-O(17)#11	2.542(10)	Si(1)-O(3)	1.626(14)
Ca(6)-O(30)#8	2.566(9)	Si(1)-O(1)	1.639(8)
Ca(6)-O(6)#9	2.583(11)	Si(1)-O(2)	1.658(11)
Ca(6)-O(20)#12	2.657(10)	Si(2)-O(9)	1.563(14)
Ca(6)-O(18)#13	2.754(11)	Si(2)-O(11)	1.602(12)
Ca(7)-O(14)#8	2.316(12)	Si(2)-O(5)	1.656(18)
Ca(7)-O(6)#2	2.363(11)	Si(2)-O(10)	1.667(11)
Ca(7)-O(12)#8	2.419(10)	Si(3)-O(13)	1.543(14)
Ca(7)-O(13)#10	2.431(13)	Si(3)-O(14)	1.660(12)
Ca(7)-O(19)#14	2.458(10)	Si(3)-O(12)	1.661(11)
Ca(7)-O(18)#15	2.545(11)	Si(3)-O(5)	1.685(18)
Ca(7)-O(17)#3	3.050(10)	Si(4)-O(16)	1.568(10)
Ca(8)-O(29)#16	2.356(9)	Si(4)-O(17)	1.594(11)
Ca(8)-O(24)#8	2.374(10)	Si(4)-O(6)	1.664(9)

Appendix

Si(4)-O(15)	1.695(11)	O(31)-Ca(6)#23	2.495(9)
Si(5)-O(20)	1.578(10)	O(31)-Ca(8)#15	2.968(9)
Si(5)-O(18)	1.604(11)	O(27)-Ca(5)#21	2.439(8)
Si(5)-O(6)#8	1.689(9)	O(27)-Ca(8)#15	2.471(8)
Si(5)-O(19)	1.690(10)	O(27)-Ca(5)#3	3.091(8)
Si(6)-O(23)	1.525(12)	O(32)-Zn(3)#2	1.955(9)
Si(6)-O(21)	1.640(17)	O(32)-Co(3)#2	1.955(9)
Si(6)-O(7)	1.644(10)	O(32)-Ca(6)#8	2.400(10)
Si(6)-O(22)	1.655(13)	O(32)-Ca(5)#2	2.524(10)
Si(7)-O(26)	1.541(16)	O(20)-Zn(3)#23	1.909(10)
Si(7)-O(25)	1.573(11)	O(20)-Co(3)#23	1.909(10)
Si(7)-O(7)	1.654(11)	O(20)-Ca(6)#24	2.657(10)
Si(7)-O(24)	1.694(10)	O(15)-Zn(5)#21	1.886(10)
Si(8)-O(27)	1.563(10)	O(15)-Co(5)#21	1.886(10)
Si(8)-O(28)	1.622(9)	O(15)-Ca(6)#4	2.488(10)
Si(8)-O(29)	1.662(10)	O(30)-Zn(5)#2	1.967(8)
Si(8)-O(8)	1.669(8)	O(30)-Co(5)#2	1.967(8)
Si(9)-O(32)	1.583(10)	O(30)-Ca(8)#14	2.547(8)
Si(9)-O(31)	1.585(10)	O(30)-Ca(6)#8	2.566(9)
Si(9)-O(30)	1.650(9)	O(25)-Zn(3)#7	1.948(10)
Si(9)-O(8)	1.669(8)	O(25)-Co(3)#7	1.948(10)
O(1)-Si(1)#8	1.639(7)	O(25)-Ca(9)#4	2.419(10)
O(1)-Ca(3)#9	2.533(13)	O(25)-Ca(8)#8	2.543(10)
O(1)-Ca(3)#2	2.533(13)	O(13)-Ca(7)#23	2.431(13)
O(2)-Ca(3)#3	2.375(11)	O(13)-Ca(2)#11	2.669(12)
O(2)-Ca(1)#21	2.399(11)	O(13)-Ca(4)#3	2.874(12)
O(2)-Ca(3)#11	3.039(11)	O(19)-Zn(4)#23	1.932(9)
O(3)-Zn(2)#9	1.880(14)	O(19)-Co(4)#23	1.932(9)
O(3)-Co(2)#9	1.880(14)	O(19)-Ca(7)#16	2.458(10)
O(4)-Zn(5)#2	1.930(10)	O(11)-Ca(2)#21	2.477(11)
O(4)-Co(5)#2	1.930(10)	O(11)-Ca(4)#3	2.615(10)
O(4)-Ca(3)#2	2.399(10)	O(11)-Ca(2)#11	2.736(10)
O(5)-Ca(4)#2	2.43(2)	O(17)-Ca(3)#21	2.425(10)
O(5)-Ca(2)#9	2.65(2)	O(17)-Ca(6)#5	2.542(10)
O(7)-Ca(1)#7	2.480(10)	O(17)-Ca(7)#6	3.050(10)
O(7)-Ca(9)#4	2.574(10)	O(12)-Zn(4)#9	1.977(10)
O(8)-Ca(5)#2	2.407(8)	O(12)-Co(4)#9	1.977(10)
O(8)-Ca(8)#14	2.753(8)	O(12)-Ca(7)#8	2.419(10)
O(6)-Si(5)#8	1.689(9)	O(12)-Ca(2)#9	2.501(10)
O(6)-Ca(7)#7	2.363(11)	O(29)-Zn(3)#21	1.945(9)
O(6)-Ca(6)#4	2.583(11)	O(29)-Co(3)#21	1.945(9)
O(24)-Zn(5)#21	1.954(10)	O(29)-Ca(8)#14	2.356(9)
O(24)-Co(5)#21	1.954(10)	O(10)-Zn(4)#21	1.962(10)
O(24)-Ca(8)#8	2.374(10)	O(10)-Co(4)#21	1.962(10)
O(24)-Ca(1)#7	2.638(10)	O(10)-Ca(4)#2	2.525(10)
O(18)-Ca(9)#21	2.502(10)	O(28)-Zn(6)#21	1.961(8)
O(18)-Ca(7)#17	2.545(11)	O(28)-Co(6)#21	1.961(8)
O(18)-Ca(6)#22	2.754(11)	O(16)-Zn(2)#21	1.934(10)
O(26)-Ca(8)#23	2.547(15)	O(16)-Co(2)#21	1.934(10)
O(26)-Ca(1)#6	2.624(14)	O(22)-Zn(4)#7	1.938(13)
O(26)-Ca(9)#5	2.722(14)	O(22)-Co(4)#7	1.938(13)
O(21)-Ca(4)#21	2.489(16)	O(22)-Ca(9)#4	2.566(13)
O(21)-Ca(9)#5	2.649(15)	O(9)-Zn(1)#21	2.011(13)
O(21)-Ca(1)#6	2.792(15)	O(9)-Co(1)#21	2.011(13)
O(31)-Ca(5)#3	2.421(9)	O(9)-Ca(2)#9	2.497(13)

Appendix

O(23)-Zn(2)#25	1.929(11)	O(14)-Co(2)#9	1.952(11)
O(23)-Co(2)#25	1.929(11)	O(14)-Ca(7)#8	2.316(12)
O(14)-Zn(2)#9	1.952(11)		

Symmetry transformations used to generate equivalent atoms:

#1 x,y,z-1 #2 y,-x+1,-z+1 #3 y,-x+1,-z+2 #4 y,-x,-z+1 #5 y,-x,-z+2 #6 -y+1,x,-z+2 #7 -y+1,x,-z+1 #8 -x,-y+1,z #9 -y,x,-z+1 #10 -x,-y+1,z-1 #11 -y,x,-z+2 #12 y-1,-x,-z+1 #13 y-1,-x,-z+2 #14 -y+1,x+1,-z+1 #15 -y+1,x+1,-z+2 #16 y-1,-x+1,-z+1 #17 y-1,-x+1,-z+2 #18 -x,-y,z-1 #19 -x+1,-y,z-1 #20 -x+1,-y+1,z-1 #21 x,y,z+1 #22 -y,x+1,-z+2 #23 -x,-y+1,z+1 #24 -y,x+1,-z+1 #25 -x+1,-y,z+1

Table 4 Anisotropic displacement parameters ($\text{\AA}^2 \times 10^3$) for $P\bar{4}$. The anisotropic displacement factor exponent takes the form: $-2\pi^2 [h^2 a^{*2} U^{11} + \dots + 2 h k a^* b^* U^{12}]$.

	U11	U22	U33	U23	U13	U12
Ca(1)	34(2)	40(2)	16(1)	1(1)	5(1)	19(1)
Ca(2)	24(1)	22(1)	18(1)	-4(1)	-1(1)	7(1)
Ca(3)	23(1)	31(1)	30(1)	16(1)	8(1)	10(1)
Ca(4)	36(2)	46(2)	27(2)	17(2)	8(1)	19(1)
Ca(5)	9(1)	3(1)	20(1)	-1(1)	5(1)	-5(1)
Ca(6)	9(1)	19(1)	28(2)	5(1)	6(1)	-1(1)
Ca(7)	22(1)	38(2)	17(1)	-9(1)	-7(1)	8(1)
Ca(8)	9(1)	10(1)	19(1)	-1(1)	-2(1)	-7(1)
Ca(9)	23(1)	15(1)	23(1)	-3(1)	5(1)	7(1)
Co(1)	42(2)	42(2)	5(2)	0	0	0
Co(2)	26(1)	9(1)	24(1)	-2(1)	-1(1)	2(1)
Co(3)	13(1)	12(1)	19(1)	1(1)	-3(1)	-1(1)
Co(4)	16(1)	14(1)	16(1)	2(1)	-2(1)	-1(1)
Co(5)	18(1)	5(1)	31(1)	2(1)	8(1)	3(1)
Co(6)	15(1)	15(1)	20(2)	0	0	0
Zn(1)	42(2)	42(2)	5(2)	0	0	0
Zn(2)	26(1)	9(1)	24(1)	-2(1)	-1(1)	2(1)
Zn(3)	13(1)	12(1)	19(1)	1(1)	-3(1)	-1(1)
Zn(4)	16(1)	14(1)	16(1)	2(1)	-2(1)	-1(1)
Zn(5)	18(1)	5(1)	31(1)	2(1)	8(1)	3(1)
Zn(6)	15(1)	15(1)	20(2)	0	0	0
Si(1)	12(1)	12(1)	13(1)	-5(1)	-2(1)	-1(1)
Si(2)	14(2)	24(2)	21(2)	-5(2)	-6(1)	4(2)
Si(3)	20(2)	20(2)	19(2)	4(2)	6(2)	3(1)
Si(4)	22(2)	22(2)	30(2)	-2(2)	5(2)	7(2)
Si(5)	11(1)	5(1)	21(2)	2(1)	1(1)	-4(1)
Si(6)	17(2)	16(2)	17(2)	5(1)	2(1)	1(1)
Si(7)	17(2)	23(2)	15(2)	-2(1)	0(1)	1(1)
Si(8)	11(1)	12(1)	22(2)	0(1)	-1(1)	2(1)
Si(9)	9(1)	15(2)	22(2)	3(1)	0(1)	-2(1)

Appendix C. Abbreviations

ARM	Atomic Resolution Microscope
BF	Bright-Field
BSE	Backscattered Electron
C phase	Commensurate Phase
CTF	Contrast Transfer Function
CZ	Czochralski
DC(s)	Discommensuration(s)
DF	Dark-Field
DSC	Differential Scanning Calorimetry
EDP(s)	Electron Diffraction Pattern(s)
EDS	Energy Dispersive X-ray Spectrometry
EPMA	Electron Probe Microscopic Analyzer
ESR	Electron Spin Resonance
FC	Field Cooled
FZ	Floating Zone
HRTEM	High-Resolution Transmission Electron Microscope
HVTEM	Hihg-Voltage Transmission Electron Microscope
I phase	Incommensurate Phase
ICCD	International Center for Diffraction Data
ICSD	Inorganic Crystal Structure Database
IFFT	Inverse Fast Fourier Transformation
MPMS	Magnetic Properties Measurements System
N phase	Normal Phase
SE	Secondary Electron
SEM	Scanning Electron Microscope
T _{I-C}	Transition Temperature from the Incommensurate to the Commensurate Lock-in Phase
T _{I-N}	Transition Temperature from the Incommensurate to the Normal Phase
WDS	Wavelength Dispersive X-ray Spectrometry
WF	Weak Ferromagnetism
WPOA	Weak Phase Object Approximation
XRD	X-Ray Diffraction
ZFC	Zero Field Cooled

Acknowledgements

I gratefully acknowledge all the people who gave me supports and helps to my Ph.D program and my life during the past years of my stay in Germany, although the words here are too limited to express my sincere thanks. I also acknowledge the funding by the Deutsche Forschungsgemeinschaft (DFG).

I would deeply thank Dr. Andreas K. Schaper who led me to the research field of the structure modulation. With his constant guidance and encouragement, I was more confident in the work of this dissertation. Many opportunities he gave me to practice have stimulated many of my interests and enabled me to gain more experiences in my research field. I have learned quite a lot from his extensive knowledge, especially in material sciences as well as electron microscopy and many brilliant and creative ideas. His kind and all-aspect help has made the past years an ever-good memory in my life.

I am especially grateful to Dr. Helmut Rager for offering my Ph.D project. His supervision and continuous supports laid a smooth way for my studies and research work. I am also thankful to his kind understanding and support in all aspects, especially in ESR measurements.

I am greatly thankful to Dr. Werner Treutmann for his powerful help about single crystal growth and magnetic measurements and for his kind supports in all aspects.

I am deeply grateful to Prof. Dr. Haoqing Hou who introduces me a chance to Germany and gave me many helps in my research work and life since I came to Germany.

I am especially grateful to Prof. Dr. Werner Massa who gives me many supports about XRD measurements. He is so kind and patient. I have also learned much knowledge about XRD by discussing with him.

It has been a very nice and a good memory for me to share the office with Mr. Michael Hellwig. He is so kind that he is always willing to help me whenever being asked and he is always capable of solving problems.

I am thankful to Mr. Norbert Lessmann for technical supports during crystal growth and kind help in other aspects.

I want to express my thanks to Dr. Hans Ahsbals for offering the sample orientation machine and to Mr. Heinz Jepsen for help on powder X-ray diffraction.

I would like to show my sincere gratitude to Michael Pokoj, Sauerwald Frank and Torsten Torunski.

I wish to say many thanks to Dr. Fritz Phillipp of the Max-Planck-Institut für Metallforschung in Stuttgart for the ultra-high resolution TEM measurements and Dr. Dieter Rhede of the Geoforschungszentrum in Potsdam for the compositional analysis by EPMA.

Acknowledgements

I would also say thanks to all my friends in Marburg, especially, Dr. Aiguo Wu, Mrs. Jinju Lv, Dr. Yi Yu and Mrs. Siming Lu for their help in the past years.

At last, I thank my wife, Lihua Yu, for giving me the most patient and loving supports and encouragement to my work; my parents, for their ever-loving supports and understanding during the years of my studies and work.

Curriculum Vitae

17. 06. 1974 born in Mutouhu Village, Baotou City,
Innermongolia province, P. R. China.
09. 1981 – 07. 1986 elementary school, Mutouhu, Innermongolia, P.R.
China.
09. 1986 – 07. 1991 middle school, Sandaohe, Innermongolia, P.R. China.
09. 1991 – 07. 1994 high school, the First High School of Salaqi County,
Innermongolia, P.R. China.
09. 1994 – 07. 1998 study in the Department of Chemistry, Innermongolia
Normal University, Hohhot, P. R. China.
07. 1991 BACHELOR`s degree of Chemistry Education.
09. 1998 -12. 2001 postgraduate study in the Key Laboratory of Rare
Earth Chemistry and Physics, Changchun Institute of
Applied Chemistry, Chinese Academy of Sciences,
130022 Changchun, P. R. China.
12. 2001 MASTER`s degree of Science.
- from 01.2002 Ph.D student in the research group of Prof. Dr.
Helmut Rager, the Department of Geosciences and
Material Sciences Center, Philipps-University of
Marburg, 35032 Marburg, Germany.

Erklärung

ich versichere, daß ich meine Dissertation

Structure Modulation and Phase Transitions in Melilites

selbständig, ohne unerlaubte Hilfe angefertigt und mich dabei keiner anderen als der von mir ausdrücklich bezeichneten Quellen und Hilfen bedient habe.

Die Dissertation wurde in der jetzigen oder einer ähnlichen Form noch bei keiner anderen Hochschule eingereicht und hat noch keinen sonstigen Prüfungszwecken gedient.

(Ort/Datum)

(Unterschrift mit Vor- und Zuname)